Thermally Responsive Polymers for Wearable Calorimeters

Thesis by
Vincenzo Costanza

In Partial Fulfillment of the Requirements for the
Degree of
Doctor of Philosophy in Medical Engineering

CALIFORNIA INSTITUTE OF TECHNOLOGY
Pasadena, California

2022
Defended May 12, 2022

Vincenzo Costanza
ORCID: [0000-0002-2409-0632]

ACKNOWLEDGEMENTS

First and foremost, I would like to thank my advisor, Prof. Chiara Daraio. I will always be grateful for the opportunity she has given me, the continuous encouragement and trust she has always put in my work, and the guidance during these years. I would also like to thank my thesis committee, Wei Gao, Yu-Chong Tai, and Azita Emami, for serving in this capacity and for providing valuable feedback on this thesis.

Secondly, I want to thank all the people I worked with: Luca Bonanomi who taught me so much and I still consider a mentor even though we parted ways; Linghui Wang, an incredible scientist and office mate who I am very grateful to for all the things she taught me; Kevin Kim for the fun time we had in the lab. I do not think this thesis could have seen the daylight if it wasn't for the fruitful conversations and the exchange of ideas I have had with each and every one of them. A special thanks to past and current members of the Daraio group, especially to the Italians Antonio, Paolo, and Giovanni with whom I have probably consumed more coffee than in my entire life.

All of the work I have done here could not have been possible without the love and friendship of some very special people: Connor, Alex, Jess, Varun, and Stefano. They are for me like a family away from home and I will forever be thankful for supporting me during difficult times, making me laugh, and giving me that warmth that only true friends can give. Giulia, Alice, and Anna also deserve a special mention: even if only we've interacted for a limited amount of time are now in my heart and forever will be my adopted sisters.

I wanted also to thank another extremely special people I have met during this journey, my girlfriend Brittany. Her unconditional support and love, especially during the past two year, have been the light that allowed me to complete this task and to be here today.

Immense gratitude goes to my family, in particular to my dad who, I know, misses me every day and who he made incredible sacrifices to give me the possibility of a great education and a better life. My sisters and their families, who have supported and loved me even though not particularly happy I am this far away from home. Finally, a special thought to my mom who, even if not here, has continuously made me feel the presence of an angel by my side. I know she would be very proud of me.

ABSTRACT

The measurement of the body core temperature (BCT) can provide insightful health information spanning from hypothermia and heat stroke to inflammations and infections. In addition, the continuous monitoring of the BCT can unlock new possibilities for people's well-being such counting of burnt calories, prediction of the ovulation period in the female population, and for the assessment of mental health issues. However, the integration of a BCT sensor in wearable devices is extremely challenging, since standard methods cannot combine minimal invasiveness with high measurement accuracy. Dual heat flux (DHF) thermometry is a novel technique that allows the precise estimation of BCT from the measurement of skin temperature. Nevertheless, the limited precision of currently available temperature sensors has not favored the wide spread of devices based on this architecture. In this thesis, we present the fabrication of a fully wearable DHF thermometer realized by integrating new polymers with a remarkable temperature sensitivity. In these particular polymers, an increase in temperature results in a change of the ionic conductivity. In the first part of this work, we focus on the understanding of the ion transport mechanism in these polymers and, in particular, on the nature of the interaction between the functional groups present on the polymer backbone and the conducting species (i.e. metal cations and water molecules). We show that the ion's coordinating environment is the key to make these materials highly sensitive to temperature. The second part of the thesis tackles the fabrication of a BCT sensor, integrating these temperature responsive polymers in an ultrathin DHF thermometer. Building on the understanding of the nature of the temperature response, we optimize the polymer's composition to obtain a thermal sensitivity that allows a good precision when measuring the BCT. Finally, we characterize the performance of the fabricated DHF thermometer in different conditions, assessing the sensor's accuracy and response time.

PUBLISHED CONTENT AND CONTRIBUTIONS

[1] G. Cantarella*, V. Costanza*, A. Ferrero, R. Hopf, C. Vogt, M. Varga, . Petti, N. Münzenrieder, L. Büthe, G. Salvatore, A. Claville, L. Bonanomi, A. Daus, S. Knobelspies, C. Daraio, and G. Tröster. Design of engineered elastomeric substrate for stretchable active devices and sensors. *Advanced Functional Materials*, 28(30):1705132, 2018. doi: 10.1002/adfm.201705132.
G.C. and V.C. contributed equally to this work. V.C. realized and measured the temperature sensor. V.C. performed the DIC measurements. V.C. participated in writing and revising the manuscript.

[2] V. Costanza and C. Daraio. Body core temperature sensors based on novel organic temperature sensitive polymers. *in submission*, 2022. V.C. participated in the conception of the project and the design of the research. V.C. performed the numerical simulation and the electrical measurement. V.C. designed and tested the readout circuit, and performed the bench top testing. V.C. participated in writing and revising the manuscript.

[3] V. Costanza, L. Bonanomi, G. Moscato, L. Wang, Y. S. Choi, and C. Daraio. Effect of glycerol on the mechanical and temperature-sensing properties of pectin films. *Applied Physics Letters*, 115(19):193702, 2019. doi: 10.1063/1.5121710.
V.C. participated in the conception of the project, in designing the experiments, in material characterization experiments and in writing and revising the manuscript.

[4] V. Costanza*, L. Wang*, N. Higdon, and C. Daraio. Ion transport phenomena in thermally responsive polyelectrolytes. *in submission*, 2022.
V.C. and L.W. contributed equally to this work. V.C. participated in the conception of the project and the design of the research. V.C. performed the gravimetric analysis and the dielectric spectroscopy measurement. V.C. partecipated in analyzing the data. V.C. participated in writing and revising the manuscript.

[5] T. H. Kim, Z. Zhou, Y.S. Choi, V. Costanza, L. Wang, Y. Yun, H. Kang, S. Kim, and C. Daraio. Flexible biomimetic block copolymer composite for temperature and long-wave infrared sensing. *Nature Communications, under review*, 2022.
V.C. participated in the conception of the project and the design of the research. V.C. built the custom measurement stage for thermal characterization, and participated in conducting electrical measurements, mechanical tests and in analyzing the data.

TABLE OF CONTENTS

LIST OF TABLES

Chapter 1

INTRODUCTION

1.1 Research Objectives

The focus of this work is the fabrication of a wearable body core temperature sensor that employs new organic materials with an unprecedented temperature response. The main objectives of the research presented in this thesis are:

- the understanding of the ion transport phenomena and the mechanisms responsible for the temperature response in these polymers to optimize their sensing properties.
- the optimization and integration of these novel materials in a dual heat flux thermometer to fabricate sensors that can correctly measure the core temperature of the body.

These sensors will offer new opportunities that can enhance healthcare quality in hospitals and improve telemedicine effectiveness.

1.2 Motivation for a Preventive Healthcare System

Over the last two centuries, human life expectancy has exponentially grown, although at different rates depending on the geographical area and sociocultural background. If the average expectancy for an American man was 69.7 in 1960, it raised almost 10 years to 79.4 in 2015. This trend does not appear to change: for instance, the average life expectancy for the total population in the United States is predicted to grow to 85.6 in 2060 from 79.7 in 2017 (US Census, February 2020). The reasons why people live longer are variegated, but among the most important we can find the progress in medical technology and in the quality of the administered cures, an increased awareness towards self-care as well as the boost in preventive measurements, and the growth in quality of living. Although exciting and wonderful upsides exist, the extension of human lifespan does not come cost free. In fact, the use of the healthcare system is not distributed equally with the age group, but it shows a strong age dependence with a steep exponential increase after age 50. With the increase of the older population, the associated healthcare expenditure is steadily raising: studies have shown that on average the per capita expenditure is ten times

higher for a man age 85 compared to a man age 40 [1]. This problem presents an unprecedented challenge for the future of the healthcare system, and especially for the social welfare, being a substantial burden on countries' economies. Higher hospitalization rates, rise in age-related chronic illnesses, and an increasing need for long-term care have been identified as the major factors that drive the healthcare expenditure for the elderly. Nonetheless, the increase in the healthcare cost associated with an older population is not the only problem caused by a longer lifespan. In the last two decades, a rather fundamental question has been posed: should the focus of medical research shift from increasing the quantity of life to increasing its quality? In fact, even though life expectancy has increased, the same cannot be said about the quality of life for the older population: the risk of disease, disability, and dementia has increased at a similar rate as the life expectancy [2]. Healthcare providers are therefore looking for the next generation of services that can lower the per capita expenditure and, at the same time, improve the quality of life for those in need. Remote patient monitoring (RPM) is considered an increasingly cost effective method to deliver patient care. In combination with telemedicine, it expands access to physicians and specialists, and ensures that patients can have the right care, at the right place, at the right time. This will encourage preventive measures that will help reduce the hospitalization rate and the need for more expensive treatments. Through RPM, healthcare workers will have access to vital functions and signals, which will tailor the administered cure to the specific symptoms. Moreover, in the event of hospitalization, patients can be sent home much more quickly and be monitored from remote. Lastly, in the case of chronic diseases, patients will not require constant supervision allowing them a higher degree of independence. Combined with the immediate advantages that RPM presents in terms of immediate applicability, the long term potential of this approach has to also be considered. In fact, the merging of current remote monitoring technologies can be combined with Artificial Intelligence algorithms in order to create extremely powerful diagnostic tools. RPM has therefore the potential to combine a cheaper access to care, while keeping high treatment standards, with the improvement of quality of life through prevention and the possibility of treatment in more caring environments than hospitals or nursing houses.

1.3 Significance of Wearable Devices in the Healthcare System

RPM is mainly based on non-invasive remote monitoring devices that measure common physiological parameters, and wirelessly transmit them to healthcare providers

or other monitoring entities. The real time data collection is crucial for the efficacy of RPM. Advances in sensing technologies and microelectronics have enabled the creation of sensors with medical accuracy and are small enough to be worn during everyday activities with no discomfort. Wearable devices made their appearances shortly after the transistor era with the first examples in the 70s and 80s as wrist watch calculators and Walkman portable radios. At the beginning of the 2000s, wearables started showing their potential with the introduction of devices like the iPod and the FitBit. It was only with the improvement of energy efficient hardware and high power density batteries in the 2010s that true wearable devices for medical applications started flooding the market and showing their true potential, especially in conjunction with the development of the internet of things (IoT). The outbreak of the COVID-19 pandemic has solidified and sped up the spread of wearable devices as also shown by the market trends. The global wearable devices market is predicted to grow at a compound annual growth rate (CAGR) of 11.8% during the period 2019-2026[1], and expected to reach 150 billion EUR by 2028[2]. Nowadays, there is a number of available wearable devices that are specifically used to monitor health conditions from continuous glucose monitors to non-invasive wearable electrochemical sensors. Of great importance are those devices with a particular focus on the monitoring of vital signs: pulse and breathing rates, blood pressure, and oxygenation level. These physiological outputs are usually complemented by the measurement of the body core temperature (BCT), defined as the temperature of the inner organs and the brain, which is another widely used diagnostic tool in everyday life as well as in medical care environments. Fever and inflammations cause an increase in the BCT, which can also be correlated to multiple dangerous health conditions such as heat exhaustion [3], heat stroke [4], and hyperthermia [5]. These events can lead to death in the most severe cases. Hypothermia, on the other hand, can affect the circulatory system and it is known to affect patients during the perioperative period [6]. Other physiological processes are associated with a change of the BCT. For example, cellular metabolism that involves a complex sequence of biochemical reactions has heat as one of its main products [7]. BCT therefore can be used for the analysis of how the body responds to a particular diet, or it could be used to measure the calorie expenditure [8, 9]. Another important application includes the analysis of the circadian rhythm which is correlated with several diseases

[1]Llamas R.T. Enterprise Wearable Market: Information By Technology, Product, Application, and Regional Outlook – Forecast Till 2026: Tech. Rep. SR1195 (2019).

[2]Hayward J., Wearable Sensors 2018-2028: Technologies, Markets & Players 2018, I-SCOOP Wearables Market Outlook 2020: Drivers and New Markets (2016).

including narcolepsy [10], insomnia [11], burnout [12], and can give information even on degenerative diseases such as Parkinson [13] and Alzheimer [14]. However, the measurement of the BCT is not a trivial task, mainly because the most accessible areas for temperature reading are situated in the periphery of our body, which show little correlation to BCT. BCT wearable monitors could therefore greatly improve the current set of wearable devices in the context of RPM.

1.4 State of the Art of Body Core Temperature Sensors

Even though several examples of wearable sensors measuring physiological signs have been reported, there are almost no successful attempts on the realization of wearable BCT sensors. The main challenge lies in combining a high degree of accuracy with no or relatively small invasiveness. The gold standard for BCT measurement is the pulmonary artery catheter, in which a thermal probe is inserted by the mean of a catheter into the pulmonary artery. This method is the most accurate because it measures the temperature of the blood directly from the core and its surroundings. However it is greatly invasive and can be used only in hospital settings during surgeries. Another rather invasive method consists in the placement of a temperature sensor in the rectum. Besides the evident discomfort and the impossibility of keeping a sensor in the area at all time, rectal BCT sensors also show a slow temperature response and low accuracy in the event of rapid temperature changes. Esophageal sensors are located deep in the esophagus, close to the left ventricle and the aorta. They show similar characteristics of rectal sensors with an improved time response at the cost of irritation of nasal passages and a general subject discomfort. In order to reduce the discomfort during the measurement of the BCT, non-invasive techniques have been developed. Ingestible radio pills are common to measure BCT, particularly in ambulatory settings. These pills measure the temperature of the surrounding of the gastrointestinal region and then transmit the data through a radio wave to an external receiver. However, these ingestible pills provide temperature data only over a limited time (i.e. when the pills are in the digestive system), without offering the possibility of continuous monitoring. Probably the most used in clinical experiments is the measurement of the oral temperature. However, environmental factors, the consumption of hot/cold drinks, or smoking can impact the outcome of the measurement. In addition, unless oral implants are developed, the continuous monitoring inside the oral cavity is not possible. Another popular method is the measurement of the temperature of the tympanic membrane, usually recorded with an infrared detector, that receives blood

from the branches of the internal carotid artery. Even if the site is easily accessible, this method is problematic and not accurate especially for continuous monitoring because it can be affected by multiple external factors. The least invasive method is the measurement of the skin temperature: it offers easy access to the area and, at the same time, it gives the possibility to "wear" devices with no discomfort for the patient. Nonetheless, not only skin temperature greatly differs from the core temperature (typically 2 to 4 °C lower), but it also shows remarkable variance from area to area of the body [15]. These factors make measuring skin temperature an approach with great potential to record BCT but with an accuracy too low to favor the spread of such devices as BCT sensors. As previously mentioned, skin temperature does not reflect BCT, since thermoregulatory processes keep peripheral areas at lower temperature than the core. Nevertheless, under certain conditions, the skin temperature can reflect with high precision the core temperature. Multiple approaches have been employed to improve the accuracy and precision of skin temperature sensors in measuring BCT. Zero heat flux (ZHF) is a non-invasive method that allows to continuously monitor the BCT from the skin surface [16]. This technique sets a zero heat flow on a certain area of the skin: in absence of heat flowing through the skin, the temperature at the surface of the skin equals the temperature of the inner tissues (Fig. 1.1(a)). A ZHF thermometer consist of two precision thermistors separated by a layer of thermal insulating layer. Another insulating layer is placed on top of the probe to minimize thermal losses. This architecture is then covered by a servocontrolled heating element that will force the temperature of the heater to equal the skin temperature, providing a heat flux of the same magnitude but different direction than the one produced by the body. Multiple scientific as well as clinical reports confirm that ZHF thermometry has the degree of accuracy required to indirectly measure BCT and it has started to be employed in clinical settings, especially during the perioperative stage to prevent hypothermia [17–19]. Nonetheless, ZHF thermometry presents three major flaws that prevent it to be widely used in everyday life. Firstly, the presence of a heater to counterbalance the heat produced by the body requires a power density that cannot be given by a portable battery, and it therefore requires to be connected to the power grid; this makes ZHF thermometry not suitable to be employed in wearable sensors. Secondly, the heat flow sensor relies on the heat flowing from the body to the environment. In the case of environmental temperatures higher than the body temperature, the ZHF thermometer cannot properly function. Lastly, slight discomfort has been reported in the region where the sensor is heating the skin. As a result, ZHF thermometers

have found application only in hospital environments, where they have shown to be a good alternative to more invasive methods, but not as a wearable sensor for daily use. An alternative use of the heat flow principle can be found in the double temperature sensor (DTS) [20]. Here, a temperature sensor and a heat flow sensor are combined in the same architecture of the ZHF thermometer but without the presence of a heater (Fig. 1.1(b)). The temperature of the core can be extracted as:

$$T_c = T_{h_1} + \frac{k_s}{k_g}(T_{h_1} - T_{h_2}). \tag{1.1}$$

where T_{h_1} and T_{h_2} are the temperature of the top and bottom sensors, respectively, k_s is the heat transfer coefficient of the insulating layer between the two sensors, and k_g is the heat transfer coefficient of the human tissue. As showed in Eq.(1.1), to compute the BCT T_c, the value of the heat transfer coefficient of the underlying human tissue k_g needs to be known. Therefore, the DTS needs to be placed in an area where there is no large variance of the thermal properties of the tissue regardless of the patient's gender, BMI, or age. Usually, the forehead is an insensitive region with respect to different human characteristics and therefore is chosen for the operation of the DTS. Clearly, the minimal difference in the thermal properties of the chosen region will greatly affect the outcome of the measurement. Contrasting results on the accuracy of this type of sensor have been reported within a range of <0.5 °C to >1 °C, making the sensor's performance unreliable [21, 22]. In an effort to make the heat flux method insensitive to the underlying tissue, dual heat flux (DHF) thermometry has been developed [23]. In this technique, the BCT is indirectly measured from the skin temperature using the measurement of the heat flow in two thermal insulators with different thermal resistances. The schematic of a DHF thermometer is shown in Figure 1.1(c). Two pairs of temperature sensors sandwich two thermal insulators, with thermal resistance R_1 and R_2, respectively. The heat flows Q_1 and Q_2 flowing through each pair of sensors are:

$$Q_1 = \frac{T_{u_1} - T_s}{R_1} \qquad Q_2 = \frac{T_{u_2} - T_s}{R_2}. \tag{1.2}$$

where T_s is the temperature of the skin and T_u is the temperature at the top surface of the insulator. Similarly, the temperature at the core can be obtained as:

$$Q_b = \frac{T_{b_1} - T_s}{R_s}. \tag{1.3}$$

where T_b is the temperature at the core and R_s is the thermal resistance of the skin. Since the heat flows are the same ($Q_1 = Q_2 = Q_b$), the BCT can be calculated

combining Eqs. (1.2) and (1.3):

$$T_b = T_s + \frac{R_s}{R}(T_s - T_u). \tag{1.4}$$

which corresponds to the temperature measured by the DTS. The thermal resistance R_s of the tissue under the insulator cannot be easily measured and still remains an unknown. When combining two pairs of this sandwiched architecture, the BCT calculated from each insulator is given by:

$$T_b = T_1 + \frac{R_s}{R_1}(T_1 - T_3). \tag{1.5}$$

$$T_b = T_2 + \frac{R_s}{R_2}(T_2 - T_4). \tag{1.6}$$

with T_1 and T_2 being the skin temperature beneath the two insulators, and T_3 and T_4 the temperature at the upper surface of the two insulators. Since the two insulators are placed close to each other, the R_s is the same and can be eliminated from the equation. Thus the BCT can be computed as:

$$T_b = T_1 + \frac{(T_1 - T_2)(T_1 - T_3)}{K(T_2 - T_4) - (T_1 - T_2)}. \tag{1.7}$$

with K the ratio between the two thermal resistances R_1/R_2, that can be determined both experimentally and theoretically. Although promising, there have been only

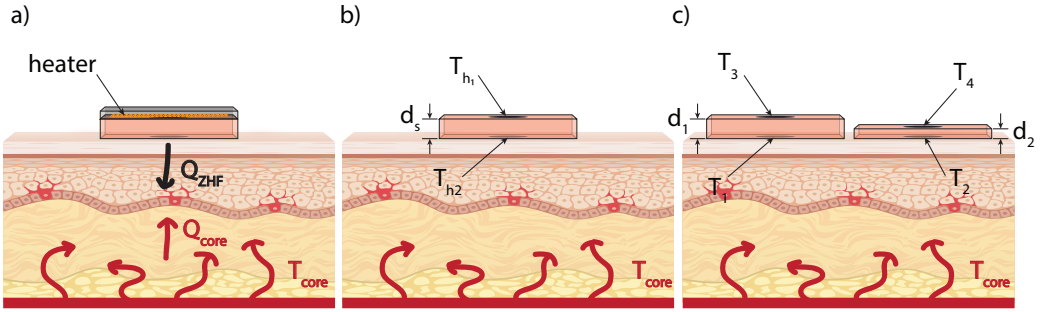

Figure 1.1: Schematic of different BCT sensor architectures. (a) Zero heat flux thermometry. (b) Dual temperature sensor. (c) Dual heat flux thermometry.

few experimental implementations of DHF thermometers [23–26]. The lateral heat flux, neglected in the calculation of the BCT, contributes to the measurement error. Moreover, the size of these devices do not allow a full wearability: the final device has a thickness between 15 mm and 10 mm, which is mainly determined by the accuracy and resolution of the individual temperature sensors employed to measure the different surface temperatures. In the simplified 2D case with unidirectional

heat flow, the temperature gradient that develops across the insulator's surfaces due to the heat flow generated by the body is:

$$\Delta T = \frac{\Delta x}{Ak} q. \tag{1.8}$$

with ΔT temperature difference between the top and bottom surfaces, Δx the thickness of the sample measured on the direction of the heat flow, A the cross sectional area measured perpendicularly to the direction of the heat flow, k the thermal conductivity of the sample, and q the heat flow rate. From Eq.(1.8), it is clear that a certain insulator thickness must be ensured in order to develop a detectable temperature gradient. Therefore, to fabricate ultrathin DHF sensors that can be worn without great discomfort, accurate and precise temperature sensors must be employed.

Temperature sensors are among the most used sensors for industrial, automotive, aereospace, and medical applications. Multiple physical stimuli are used to detect change in temperature from change in the electrical resistance, to variation in vapor pressure, volume, or optical properties. Commercially available temperature sensors can be divided into thermocouples, resistive temperature detectors, and thermistors. Thermocouples are a combination of two different thermoelements, such as conductors and semiconductors, that form an electrojunction. One junction (cold) is kept at a constant temperature and serves as the reference, while the other junction (hot) is the measuring point. According to the thermoelectric effect, also known as Seeback effect, when two dissimilar materials are fused together and kept at different temperatures, they generate an electromotive force that pushes the electrons to move from the hot end to the cold end. A voltage difference, proportional to the temperature difference and the Seeback coefficient, develops as a result across the junction. The Seeback coefficient represents the thermal coefficient that can go up to several tens of μV/K. Although thermocouples can cover a range between -200 to 2000 °C, they have some disadvantages such as alloy manufacturing uncertainties, aging effect on the junction, small output voltage with temperature change, noise over long wires, and the need of compensating an additional thermoelectric effect at the junction between the cold point and the amplification stage.

Unlike thermocouples, resistive temperature sensors (RTDs) operate on the principle that the electrical resistance of pure metals is proportional to temperature. The excess of electrons in the conduction band is impaired by their collision with atoms and other electrons that increase with increasing thermal vibration, preventing the free flow of electrons. This effect, in turn, lowers the electrical conductivity. For

example, a RTD platinum sensor has a nominal resistance of 100 Ω at 0 °C and around 140 Ω at 100 °C. Since they show an almost linear response over the range of operation, usually a single coefficient, called temperature coefficient of resistance, is given as figure of merit of the sensor and indicates the sensitivity of the material. In most applications, a four-order polynomial, the Callendar-Van Dusen equation, is used to compute the exact temperature from the electrical resistance. Copper, gold, nickel platinum, and silver are the most used materials, although platinum is probably the most employed because of its stability, range of operation (-200 to 850 °C), and good non-oxidation properties. Nickel, on the other hand, is a popular choice when a higher sensitivity is required. RTDs possess therefore features that make them suitable for their use in industrial environment. However, due to their cost, low sensitivity, slow response, and design challenges, RTDs are not widely employed for medical instrumentation.

Thermistors are similar to RTDs, in the sense that they are resistors that change resistance with temperature. Depending on the materials used, thermistors can be divided into negative temperature coefficient (NCT) thermistors and positive temperature coefficient (PTC) thermistors. NTCs show a decrease in resistance with temperature and are generally based on semiconducting materials, such as sintered metal oxides. The increase in temperature leads to an increase in the number of carriers in the conduction band, reducing the resistance of the medium. PTCs, on the other hand, decrease resistance when temperature increases. They are manufactured using doped polycrystalline ceramics that are characterized by a transition temperature. Below the transition temperature the high dielectric constant prevents the formation of potential barriers between the grain of the crystal, leading to a low resistance. Above the transition temperature, the dielectric constant drops to value sufficiently low enough that that potential barriers from at the grain boundaries, leading to a sharp increase in resistance. PCTs are used mainly in current limiting devices and fuses, while NTCs find wide application as temperature sensors. Thermistors, unlike thermocouples and RTDs, show a linear behavior only in a very limited range and therefore a single temperature coefficient of resistance cannot be defined. In order to describe the relationship between the resistance and the temperature, the Steinhart–Hart equation is often used. The increase in sensitivity and response is counterbalanced by the lack of linearity of the calibration curve and range of operation.

In summary, thermocouples are inexpensive, durable, and can measure over a wide

temperature at the cost of an extremely low voltage generated at the junction. RTDs offer a wide temperature range and stability, providing repeatable measurements with great linearity, showing however low sensitivity. Thermistors are durable and have a much higher responsivity compared to thermocouples and RTDs, but cannot operate on a large temperature range; they need heavy calibration compensation in order to have accurate temperature readings. Commercially available sensors are not suitable to be used for ultrathin DHF thermometers, which require the development of new temperature sensing materials with higher temperature sensitivity.

As current temperature sensing technology cannot satisfy the requirements for the successful fabrication of a DHF thermometer, the exploitation of new temperature sensitive materials is necessary. Organic chemistry could provide new tools to engineer polymers' properties and synthetize materials with new exotic features. As a matter of fact, organic electronic materials are nowadays emerging as an alternative to standard electronic devices. The possibility to modify the properties of a device by changing the composition of the molecular structure of the polymer it is made of has been the main attraction for this field. The first example of a device based on an organic compound was reported in the mid-80s with the demonstration of a low voltage thin film LED [27]. Since then, organic LEDs have found their way in widely available high performance displays. The spread of organic devices has surged in another field of optoelectronics: organic solar cells, based on the same principle of their inorganic counterparts, showing great potential due to their great efficiency in solar energy conversion [28].

Organic transistors made their appearance almost simultaneously with organic LEDs [29]. The formation of a conducting channel in a semiconducting material through the application of an electric field on a gate electrode can also be achieved using organic semiconductors. Nowadays, organic transistors have considerable success and are tremendously appealing for the consumer electronics market, in particular because they can be used to fabricate flexible devices. In terms of organic chemistry applied to the development of new sensing technology, extensive research has shown the great potential of this approach. For example, through organic optical sensors, it is possible to record human health information such as heart rate or oxygenation level and glucose concentration in the blood [30, 31]. Organic pressure sensors have been fabricated to measure cardiovascular pressure, which can inform on arterial stiffness, or intraocular pressure, that can be applied for the diagnosis of neurodegenerative diseases or glaucoma [32]. For example, a pressure

sensor built with an organic FET was able to analyze the pressure waveform of the radial artery and assess arterial stiffness [33, 34]. In another case, a bylayer dynamic pressure sensor was fabricated on a contact lens and then successfully implanted in a pig eye [35].

As far as temperature sensors are concerned, several examples of temperature responsive devices that employ organic material can be found in the literature. A popular approach consists in embedding conductive fillers within a polymeric matrix [36, 37]. Due to the increase in the specific volume when passing the melting point of the crystalline region, the resistance of these composites dramatically increases with temperature. Although showing a promising temperature responsivity, it is hard to employ nanofilled polymers in actual devices, in particular due to the large hysteresis that the resistance curve show, resulting in a large uncertainty over the temperature reading. Similar effects have been achieved also by inducing percolation in insulating polymer matrices with conductive materials, such as metal particles [38, 39]. These materials still suffer from a large hysteresis, probably due to the time lag required by the polymer matrix to recover after the transition, although efforts have been put to reduce this effect [36]. P-n organic junction using reduced graphene oxide in combination with polyurethane were successfully fabricated on PEDOT:PSS electrodes on a stretchable substrate [40]. These devices showed a temperature response of 1.34 %/°C, which does not justify the complex architecture and the cumbersome fabrication method. Thermoelectric effect was reproduced on a polyurethane microstructure coated with PEDOT:PSS [41], and an electrolyte-gated transistor, fabricated with P3HT/PVPA-AA and an ionic thermoelectric supercapacitor made of PEO-NaOh polyelectrolyte [42]. In both cases, the achieved Seeback coefficient and the resulting temperature response were limited.

Of particular interest recent investigations of plant cell wall components, which have shown that pectin, a structurally and functionally complex polysaccharide, has an incredibly high temperature response [43, 44]. This behavior has been attributed to the strong interaction that divalent metal cations have with the repeating units of galacturonic acid, the main constituent of pectin. In particular, the carboxyl and hydroxyl functional groups can strongly coordinate the central cation, forming an "egg-box" structure, which bridges different pectin backbones. The increase in temperature provides enough energy to the cations to escape the potential wells where they are confined and contribute to the ionic conduction. As a result, an exponential increase in conductivity is measured following an increase in temperature. Pectin

based temperature sensors have shown great potential, offering a thermal response several order of magnitudes higher compared to current technologies and an accuracy as low as 10 mK. These properties, combined with the cost effectiveness of the material fabrication and the ease of the deposition process on existing devices, make pectin based temperature sensors great candidates to be embedded in the DHF thermometers. However, even though pectin based sensors are extremely promising, their commercialization presents remarkable challenges. In fact, pectin is mainly used in the food industry as jellifying agent. As such, pectin chemical composition is not optimized nor repeatable for engineering applications, especially in the medical field. Recently, work has been carried out to synthetize a polymer (HEA–AA) that can provide comparable temperature sensing features and, at the same time, a simpler scaffold, which can be reliably synthetize and chemically tuned to adjust its physical and chemical properties [45]. The chemical structure of this polymer mimics pectin through the presence of carboxyl (acrylic acid) and hydroxyl (2-hydroxyethyl acrylate) groups. These groups create a coordination environment where divalent cations can bind with an activation energy similar to that of pectin. The result is a synthetic polymer that shows a temperature response even greater than the one reported for pectin sensors. This newly developed polymer will be employed in this work for the fabrication of an ultrathin wearable DHF sensor capable of accurately monitoring BCT.

1.5 Chapters Outline

This thesis presents the fabrication and characterization of a DHF thermometer, fabricated using novel temperature sensitive ion conducting polymers. The understanding of the interaction between the conducting species and the polymer backbone is crucial to comprehend the ion transport mechanisms and the origin of the temperature response. Therefore we will give an introduction to ion conduction in these systems in Chapter 2. In Chapter 3, we will provide a first experimental proof of how the modification of the interaction between pectin and metal ions can affect the material's properties and temperature response. In particular, we will show how water molecules play a crucial role in the temperature sensing properties of pectin. Increasing water content affects the polymer segmental motion improving the mechanical properties and conductivity. At the same time, the increased water concentration shunts the thermally activated ion conduction, degrading the temperature response of the material. In order to better understand the interactions between water molecules, ion-polymer coordination complexes and temperature re-

sponse, we will perform dielectric spectroscopy in Chapter 4. We will study these phenomena in the simplified scaffold provided by a synthetic counterpart of pectin. By coupling the time humidity superposition principle with DSC and FTIR data, we will show that the temperature response is correlated to the strength of the interaction between the coordinating ion and the polymer backbone. In addition, we will demonstrate that the role played by water within the matrix is to accelerate the ion transport and to increase the polymer's segmental motion, reducing the thermal response. The work presented in Chapters 3 and 4 is preparatory for the fabrication of the DHF thermometer, which will be presented in Chapter 5. In this chapter, we will first illustrate the operation of the polymer at different frequency, comparing the polymer's temperature sensitivity for different ion-polymer combination. We will study the temperature response in the complex impedance domain, analyzing both its absolute value and phase change with temperature. This analysis will allow to choose the combination of polymer chemical composition and frequency of operation to achieve a material with an accuracy suitable for the integration in a ultrathin DHF thermometer. Furthermore, to understand the sources of the theoretical error and further reduce the measurement error, we will conduct a FE analysis on the chosen geometry in different conditions. The architecture will then be implemented on flexible substrate and tested on a custom-made experimental set up. We will characterize the basic properties of the sensor and test its functionality in different environments. A discussion and the outlook on future work will conclude the thesis in Chapter 6.

References

[1] B. Alemayehu and K. E. Warner. The lifetime distribution of health care costs. *Health Services Research*, 39(3):627–642, 2004.

[2] G. C. Brown. Living too long. *EMBO Reports*, 16(2):137–141, 2015.

[3] R. W. Kenefick and M. N. Sawka. Heat exhaustion and dehydration as causes of marathon collapse. *Sports Medicine*, 37:378–381, 2007.

[4] Y. Epstein and W. O. Roberts. The pathopysiology of heat stroke: An integrative view of the final common pathway. *Scandinavian Journal of Medicine & Science in Sports*, 21(6):742–748, 2011.

[5] W. Sinclair, S. Rudzki, A. Leicht, A. Fogarty, S. Winter, and Patterson. M. Efficacy of field treatments to reduce body core temperature in hyperthermic subjects. *Medicine & Science in Sports & Exercise*, 41(11):1984–1990, 2009.

[6] M. Bommadevara and L. Zhu. Efficacy of field treatments to reduce body core temperature in hyperthermic subjects. *Biomechanics and Modeling in Mechanobiology*, 1(2):137–149, 2002.

[7] R. Sörbris, M. Monti, P. Nilsson-Ehle, and I. Wadsö. Heat production by adipocytes from obese subjects before and after weight reduction. *Metabolism*, 31(10):973–978, 1982.

[8] R. Walford, D. Mock, T. MacCallum, and J. Laseter. Physiologic changes in humans subjected to severe, selective calorie restriction for two years in biosphere 2: Health, aging, and toxicological perspectives. *Toxicological Sciences*, 52(2 Supplement):61–65, 1999.

[9] L. Landsberg, J. Young, W. Leonard, R. Linsenmeier, and F. Turek. Is obesity associated with lower body temperatures? Core temperature: A forgotten variable in energy balance. *Metabolism*, 58(6):871–876, 2009.

[10] H. Middelkoop, G. Lammers, B. Van Hilten, C. Ruwhof, H. Pijl, and H. Kamphuisen. Circadian distribution of motor activity and immobility in narcolepsy: Assessment with continuous motor activity monitoring. *Psychophysiology*, 32 (3):286–291, 1995.

[11] M. Van Veen, J. Sandra Kooij, A. Marije Boonstra, M. Gordijn, and E. Van Someren. Delayed circadian rhythm in adults with attention-deficit/hyperactivity disorder and chronic sleep-onset insomnia. *Biological Psychiatry*, 67(11):1091–1096, 2010.

[12] M. Bagheri Hosseinabadi, M. Ebrahimi, N. Khanjani, J. Biganeh, S. Mohammadi, and M. Abdolahfard. The effects of amplitude and stability of circadian rhythm and occupational stress on burnout syndrome and job dissatisfaction among irregular shift working nurses. *Journal of Clinical Nursing*, 28(9-10): 1868–1878, 2019.

[13] S. Li, Y. Wang, F. Wang, L. Hu, and C. Liu. A new perspective for parkinson's disease: Circadian rhythm. *Neuroscience Bulletin*, 33:62–72, 2017.

[14] D. Weldemichael and G. Grossberg. Circadian rhythm disturbances in patients with alzheimer's disease: A review. *International Journal of Alzheimer's Disease*, 2010, 2010.

[15] J. Weller. and Z. Karim. Perioperative beta-blockade: Guidelines and practice in New Zealand. *Anaesthesia and Intensive Care*, 33(5):645–650, 2005.

[16] M. Bakhsheshi, M. Ho, L. Keenliside, and T. Lee. Non-invasive monitoring of brain temperature during rapid selective brain cooling by zero-heat-flux thermometry. *Emerging Science Journal*, 3(1), 2019.

[17] M. Yamakage and A. Namiki. Deep temperature monitoring using a zero-heat-flow method. *Journal of Anesthesia*, 17(2):108–115, 2003.

[18] L.P.J. Teunissen, J. Klewer, J.J. De Haan, A .and De Koning, and H.A.M. Daanen. Non-invasive continuous core temperature measurement by zero heat flux. *Physiological Measurement*, 32(5):559, 2011.

[19] Marja-Tellervo Mäkinen, Anne Pesonen, Irma Jousela, Janne Päivärinta, Satu Poikajärvi, Anders Albäck, Ulla-Stina Salminen, and Eero Pesonen. Novel zero-heat-flux deep body temperature measurement in lower extremity vascular and cardiac surgery. *Journal of Cardiothoracic and Vascular Anesthesia*, 30 (4):973–978, 2016.

[20] Frank Sattler. Double temperature sensor with a receiving element, November 15 2011. US Patent 8,057,093.

[21] S. Mazgaoker, I. Ketko, R. Yanovich, Y. Heled, and Y. Epstein. Measuring core body temperature with a non-invasive sensor. *Journal of Thermal Biology*, 66: 17–20, 2017.

[22] J. Sastre, M. Pascual, and T. López. Evaluation of the novel non-invasive zero-heat-flux tcore thermometer in cardiac surgical patients. *Journal of Clinical Monitoring and Computing*, 33:165–172, 2019.

[23] K. Kitamura, X. Zhu, W. Chen, and T. Nemoto. Development of a new method for the noninvasive measurement of deep body temperature without a heater. *Medical Engineering Physics*, 32(1):1–6, 2010.

[24] M. Huang, T. Tamura, Z. Tang, W. Chen, and S. Kanaya. A wearable thermometry for core body temperature measurement and its experimental verification. *IEEE Journal of Biomedical and Health Informatics*, 21(3):708–714, 2017.

[25] J. Feng, C. Zhou, C. He, Y. Li, and X. Ye. Development of an improved wearable device for core body temperature monitoring based on the dual heat flux principle. *Physiological Measurement*, 38(4):652–668, 2017.

[26] J. Fang, C. Zhou, and X. Ye. Optimization of a wearable device for core body temperature monitoring based on the dual-heat-flux model. *IOP Conference Series: Materials Science and Engineering*, 677(3):032006, 2019.

[27] C. W. Tang and S. A. VanSlyke. Organic electroluminescent diodes. *Applied Physics Letters*, 51(12):913–915, 1987.

[28] Z. Zhou, W. Liu, G. Zhou, M. Zhang, D. Qian, J. Zhang, S. Chen, S. Xu, C. Yang, F. Gao, H. Zhu, F. Liu, and X. Zhu. Subtle molecular tailoring induces significant morphology optimization enabling over 16% efficiency organic solar cells with efficient charge generation. *Advanced Materials*, 32 (4):1906324, 2020.

[29] A. Tsumura, H. Koezuka, and T. Ando. Macromolecular electronic device: Field-effect transistor with a polythiophene thin film. *Applied Physics Letters*, 49(18):1210–1212, 1986.

[30] C. Lochner, Y. Khan, A. Pierre, and A. Arias. All-organic optoelectronic sensor for pulse oximetry. *Nature Communications*, 5(5745), 2014.

[31] T. Yokota, P. Zalar, M. Kaltenbrunner, H. Jinno, N. Matsuhisa, H. Kitanosako, Y. Tachibana, W. Yukita, M. Koizumi, and T. Someya. Ultraflexible organic photonic skin. *Science Advances*, 2(4):e1501856, 2016.

[32] Nicholas M. Farandos, A. Yetisen, M. Monteiro, C. Lowe, and S. Yun. Contact lens sensors in ocular diagnostics. *Advanced Healthcare Materials*, 4(6):792–810, 2015.

[33] G. Schwartz, B. Tee, J. Mei, A. Appleton, D. Kim, H. Wang, and Z. Bao. Flexible polymer transistors with high pressure sensitivity for application in electronic skin and health monitoring. *Nature Communications*, 4(1859), 2013.

[34] G. Y. Bae, S. W. Pak, D. Kim, Giwon L., D. H. Kim, Y. Chung, and K. Cho. Linearly and highly pressure-sensitive electronic skin based on a bioinspired hierarchical structural array. *Advanced Materials*, 28(26):5300–5306, 2016.

[35] V. Laukhin, I. Sánchez, A. Moya, E. Laukhina, R. Martin, F. Ussa, C. Rovira, A. Guimerá, R. Villa, J. Aguiló, J. C. Pastor, and J. Veciana. Non-invasive intraocular pressure monitoring with a contact lens engineered with a nanostructured polymeric sensing film. *Sensors and Actuators, A: Physical*, 170: 36–43, 2011.

[36] J. Jeon, H.-B.-R. Lee, and Z. Bao. Flexible wireless temperature sensors based on ni microparticle-filled binary polymer composites. *Advanced Materials*, 25 (6):850–855, 2013.

[37] T. Yokota, Y. Inoue, Y. Terakawa, J. Reeder, M. Kaltenbrunner, T. Ware, K. Yang, K. Mabuchi, T. Murakawa, M. Sekino, W. Voit, T. Sekitani, and T. Someya. Ultraflexible, large-area, physiological temperature sensors for multipoint measurements. *Proceedings of the National Academy of Sciences*, 112(47):14533–14538, 2015.

[38] X. Ren, P. K. L. Chan, J. Lu, B. Huang, and D. C. W. Leung. High dynamic range organic temperature sensor. *Advanced Materials*, 25(9):1290–1290, 2013.

[39] X. Ren, K. Pei, B. Peng, Z. Zhang, Z. Wang, X. Wang, and P. K. L. Chan. A low-operating-power and flexible active-matrix organic-transistor temperature-sensor array. *Advanced Materials*, 28(24):4832–4838, 2016.

[40] T. Q. Trung, S. Ramasundaram, B.-U. Hwang, and N.-E. Lee. An all-elastomeric transparent and stretchable temperature sensor for body-attachable wearable electronics. *Advanced Materials*, 28(3):502–509, 2016.

[41] F. Zhang, Y. Zang, D. Huang, C. Di, and D. Zhu. Flexible and self-powered temperature–pressure dual-parameter sensors using microstructure-frame-supported organic thermoelectric materials. *Nature Communications*, 6(8356), 2015.

[42] D. Zhao, S. Fabiano, M. Berggren, and X. Crispin. Ionic thermoelectric gating organic transistors. *Nature Communications*, 8(14214), 2017.

[43] R. Di Giacomo, C. Daraio, and B. Maresca. Plant nanobionic materials with a giant temperature response mediated by pectin-ca^{2+}. *Proceedings of the National Academy of Sciences U.S.A.*, 112(15):4541–4545, 2015.

[44] R. Di Giacomo, L. Bonanomi, V. Costanza, B. Maresca, and C. Daraio. Biomimetic temperature-sensing layer for artificial skins. *Science Robotics*, 2 (3):eaai9251, 2017.

[45] T. H. Kim, Z. Zhou, Y. S. Choi, V. Costanza, L. Wang, Y. Yun, H. Kang, S. Kim, and C. Daraio. Flexible biomimetic block copolymer composite for temperature and long-wave infrared sensing. *Nature Communications, under review*, 2022.

Chapter 2

INTRODUCTION TO CONDUCTION PHENOMENA IN POLYELECTROLYTES

2.1 Chapter Preamble

As discussed in Chapter 1, the fabrication of a BCT thermometer with the accuracy needed by a medical device, requires the development of sensors with a remarkable temperature sensitivity. Pectin-based temperature sensors have shown temperature sensing performances that surpass both commercial sensors as well as organic and inorganic materials currently under research. Even though, the physical nature of the temperature sensing mechanism in pectin films is not clear yet, there is strong evidence that it results from the particular interaction that metal ions have with the polymer matrix. Pectin is a polyelectrolyte that can be found and extracted from plant cells and that presents numerous acid an polar groups on its backbone. In particular conditions, the electrostatic interaction between these functional groups and metal ions (in particular Ca^{2+}) allows the formation of a physical crosslinking in the matrix. Energetically, these ions are confined in potential wells generated by these coordination complexes. At a given temperature, a certain number of these ions have enough thermal energy to escape the wells where they are confined. When temperature increases, more thermal energy is provided to the system and the number density of ions that can hop from one potential well to another increases, resulting in an increase in conductivity. As a result, pectin is a material that can be exploited for temperature sensing since its conductivity strongly depends on temperature. We will show that this relationship between conductivity and temperature mainly depends on the strength of the interaction between the ion and the coordination complex. Since the temperature response does not depend specifically on the chemical structure of the polymer but only on the nature of the ion-backbone interaction, we synthesized a polymer with a simpler structure that can recreate the same coordination environment present in pectin. This polymer, composed of 2-hydroxyethyl acrylate–acrylic acid (HEA–AA), has a temperature sensitivity even higher than the one recorded for pectin films [1]. In addition, HEA–AA simpler scaffold allows a more effective analysis of the nature of the ion-polymer interactions as well as the effect of different charge carriers on the temperature response. More specifically, due to the hydrophilic nature both of pectin and the synthetic polymer,

water molecules play an important role in the conduction mechanisms and the temperature response. Since both pectin and HEA–AA are polyelectrolytes, in this chapter, we will introduce the basic of the transport phenomena in these systems and the experimental techniques used to study them.

2.2 Introduction to Polyelectrolytes

A polyelectrolyte is a polymer that has on its backbone charged groups. Depending on the sign of this charged group polyelectrolytes can be divided into polycations, with positively charged groups, and polyanions, with negatively charged groups. Nowadays, polyelectrolytes have attracted a great deal of attention for their broad application, in particular in the energy sector, where they are employed in high energy density storage/conversion devices such as lithium batteries, supercapacitors and fuel cells. Even though, many compelling points have been addressed and significant advances have been made, this field has still major open questions that remain unresolved. In particular, it is not clear the exact microscopic phenomena that regulate the ion motion in such complex systems. Nonetheless, through electrochemical techniques, impedance spectroscopy, nuclear magnetic resonance in combination with data coming from molecular dynamics simulations, insightful information can be extracted on the ion transport phenomena in these systems. Depending on the solvent concentration in the polymer matrix, polyelectrolytes can divide into liquid or solid polyelectrolytes. In liquid polyelectrolytes, the polymer is completely dissolved in an organic solvent, such as ethylene carbonate, propylene carbonate or dimethyl carbonate, or in an aqueous solvent. In this case, the polymer network solvates the ions but the solvent helps with the ion conduction, offering paths for the ions to diffuse. On the contrary, solid polyelectrolytes are solvent free and the ions get dissociated because of the interactions with the acids and polar groups on the polymer backbone. Polymer with an extremely low glass transition temperature need to be employed to facilitate ion transport, through the backbone's segmental motion. As it will be shown later in this chapter as well as in Chapters 3 and 4, both pectin and HEA–AA need to be dehydrated to show a good temperature response, therefore they can be considered solid polyelectrolytes. As previously described, polyelectrolytes solvate ionic charges within the polymer matrix providing mechanical strength, flexibility, processability and electrochemical stability, compared to classical electrolytes. Both pectin and HEA–AA possess carboxylic functional groups which when dissolved in a solvent will partially deprotonate:

$$RCOOH \rightleftharpoons RCOO^- + H^+ \tag{2.1}$$

creating moieties that will coordinate metallic cations. Preliminary studies show that the carboxylic acid alone does not confer HEA–AA a good thermal response. The addition of highly polar hydroxyl groups, also present in pectin, results in a stronger coordination environment, possibly by stabilizing the electronic orbitals of the cations. The combined effect of carboxylic acid and hydroxyl groups confers pectin and HEA–AA a high temperature responsivity.

2.3 Ion Conduction Phenomena in Polyelectrolytes

Before diving into the interpretation of dielectric spectroscopy data, it is useful to rigorously define the concept of dielectric relaxation in a dielectric material, with bound charges. Let us consider a small perturbation $x(t)$ acting on an isotropic, linear and casual system. The response $y(t)$ can be related to the perturbation by:

$$y(t) = y_\infty + \int_{-\infty}^{t} J(t-t')\frac{dx(t')}{dt'}dt' \tag{2.2}$$

where $J(\tau)$ is the material function and y_∞ accounts for the instantaneous response of the system, that is the fast response not related to the processes we are interested in. Neglecting the instantaneous response y_∞, one can note that Eq. (2.2) represents the convolution between the material function and the derivative of the applied perturbation. Posing $\tau = t - t'$, and integrating by parts we can rewrite Eq. (2.2) as:

$$y(t) = \int_0^\infty R(\tau)x(t-\tau)d\tau \tag{2.3}$$

with $R(\tau) = dJ(\tau)/d\tau$ the impulse response of the system. Considering a periodic perturbation of the form $x(t) = x_0 e^{-j\omega t}$, and the respective Fourier transform of the perturbation $x^*(\omega)$ and the system response $y^*(\omega)$, we obtain:

$$y^*(\omega) = \chi^*(\omega)x^*(\omega) \tag{2.4}$$

where the susceptibility complex function $\chi^*(\omega)$ is the Laplace transform of the impulse function $R(\tau)$:

$$\chi^*(\omega) = \chi^{'}(\omega) - \chi^{''}(\omega) = \int_0^\infty R(\tau)e^{-j}d\tau. \tag{2.5}$$

For analogy, in the case of a dielectric linear system, the external perturbation is given by the electric field $E(t)$, while the system response is the polarization $P(t)$ and the electric displacement $D(t)$. Using the linear response theory, we can write the system response as:

$$P^*(\omega) = \epsilon_0 \chi^*(\omega) E^*(\omega) P^*(\omega) \tag{2.6}$$

$$D^*(\omega) = \epsilon_0 E^*(\omega) + P^*(\omega) = \epsilon_0 \epsilon^*(\omega) E^*. \tag{2.7}$$

Here, we have correlated the complex permittivity with the complex susceptibility as $\epsilon^*(\omega) = 1 + \chi^*(\omega)$. Both the permittivity and the susceptibility have frequency dependence, which lead to the dispersion properties of the material. In particular, the real part of the complex permittivity $\epsilon^{'}$ is called dielectric permittivity and measures the recoverable polarization (e.g. dipoles alignment to the electric field), while the real part $\epsilon^{''}$ is the permittivity loss, and defines the unrecoverable polarization (e.g. dipole relaxation processes and diffusive motion charge). Relaxation in the dielectric spectra can arise from different phenomena, namely the reorientation of dipoles with the electric fields, the long range diffusion of charged particles, or the accumulation of charges at a blocking interface. In the following sections, we will analyze these processes individually.

Debye and Non-Debye Dipole Relaxation

The simplest dielectric relaxation process corresponds to an ideal, noninteracting population of dipoles responding to an alternating electric field. Usually referred to as Debye relaxation, it can be described as the model of rotational Brownian motion of spherical dipoles in a viscous media where inertia effects are neglected [2, 3]. The main idea for this theory can be found in the fluctuation dissipation theorem (FDT), which correlates the microscopic fluctuations in a system at a thermal equilibrium to the response of the macroscopic system when an external perturbation is applied. Thermodynamics quantities usually fluctuate around their average value due to stochastic (brownian) motions of the particles in the system. For example the quantity $y(t)$, with an average value of $\langle y \rangle$, fluctuates of the quantity $\Delta y(t) = y(t) - \langle y \rangle$. The correlation function $\varphi(\tau)$, defined as $\varphi(\tau) = \langle \Delta y(t) \Delta y(t+\tau) \rangle$, relates the fluctuations at a time $\Delta y(t+\tau)$ with a previous time $\Delta y(t)$. For a stationary process, the time t does not influence the process, therefore $\varphi(\tau) = \langle \Delta y(0) \Delta y(\tau) \rangle$. We can approach the study of the polarization caused by an electric field perturbation

in the past using a similar statistical approach. We can infer that polarization decrease rate following the perturbation is independent from the past history of the material, and depends only on the polarization at that given time. In the Debye case, we can write the polarization decrease rate as proportional to the relaxation time τ_D. We obtain the following first order differential equation and relative solution:

$$-\frac{dP(t)}{dt} = \frac{P(t)}{\tau_D} \rightarrow P(t) = P(0)e^{-t/\tau_D}. \tag{2.8}$$

The normalized correlation function[1] that relates the polarization to the stochastic fluctuations will therefore be:

$$\Phi(\tau) = \frac{\langle \Delta P(0)\Delta P(\tau)\rangle}{\langle \Delta P(0)^2\rangle}. \tag{2.9}$$

The complex dielectric is associated with the correlation function as:

$$\frac{\epsilon^*(\omega) - \epsilon_\infty}{\epsilon_s - \epsilon_\infty} = \int_0^\infty -\frac{d\Phi(t)}{dt} e^{-j\omega t} \tag{2.10}$$

where ϵ_s and ϵ_∞ are the low (static) and high frequency limits of the dielectric permittivity. Combining Eq. (2.8), (2.9), and (2.10), we obtain the complex permittivity for a Debye relaxation (Fig. 2.1(a)):

$$\epsilon^*(\omega) = \epsilon_\infty + \frac{\Delta\epsilon}{1 + j\omega\tau_D}, \qquad with \;\; \Delta\epsilon = \epsilon_s - \epsilon_\infty. \tag{2.11}$$

This model provides a simple ideal understanding of the relaxation phenomena in dielectric materials. However, when compared with experimental data, it usually fails to properly describe the characteristic dielectric spectra of many materials. Specifically, experimental permittivity loss data shows broader and non-symmetrical peaks compared to the ideal Debye case. The understanding of the origin of this behavior is still under debate. Nonetheless, there are two main approaches to explain the non-idealities encountered in almost all ionic conductors. The first takes into account the fact that the individual dipole rotations are not independent, as postulated in the Debye theory, but correlated. The resulting relaxation is therefore the sum of cooperative processes [4–6]. The other approach considers the individual dipole rotations as random and independent events, each described by a Debye relaxation, but with different relaxation time. The result is an inhomogeneous and disordered environment, with a variegated energy landscape. Regardless of their physical origin, these non-idealities need to be accounted for when fitting experimental data,

[1] The normalized correlation function is usually defined as $\Phi(\tau) = \frac{\varphi(\tau)}{\varphi(0)} = \frac{\langle \Delta y(0)\Delta y(\tau)\rangle}{\langle \Delta y(0)\Delta y(0)\rangle}$.

and lead to development of modified descriptions of the Debye relaxation such as the Cole-Cole model (Fig. 2.1(b)) or the Cole-Davidson model (Fig. 2.1(c)). The Havriliak-Negami (HN) function [7] is one of the most used empirical functions to fit dielectric spectra (Fig. 2.1(d)):

$$\epsilon^* = \epsilon_\infty + \frac{\Delta\epsilon}{(1 + (j\omega\tau_D)^\alpha)^\beta}. \tag{2.12}$$

The fractal parameters α and β describe the broadening and the symmetry of the relaxation peak, respectively. Figure 2.1 shows a comparison of the dielectric and loss permittivity for Debye and non-Debye processes. They both appear as a peak in the dielectric loss and a step decrease in the dielectric permittivity.

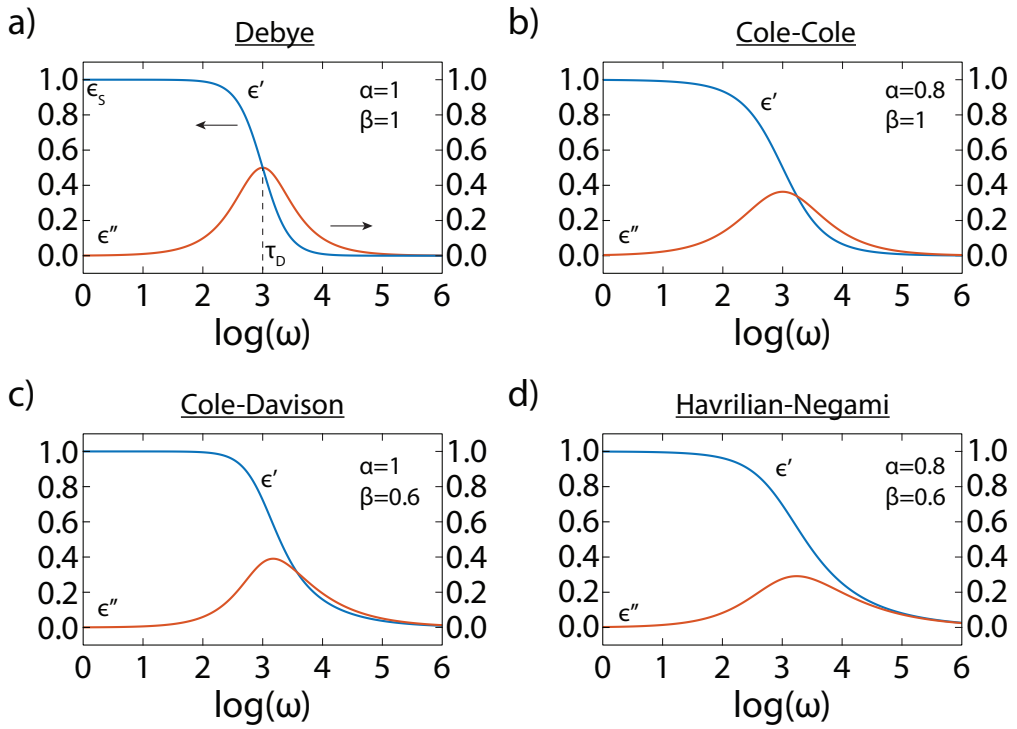

Figure 2.1: Debye and Non-Debye relaxations. (a) Dielectric permittivity (blue line) and dielectric loss (orange line) with relaxation time $\tau_D = 10^{-3}$ for different dipole relaxations: (a) Debye, (b) Cole-Cole ($\alpha = 0.8, \beta = 1$), (c) Cole-Davidson ($\alpha = 1, \beta = 0.6$), (d) Havriliak-Negami ($\alpha = 0.8, \beta = 0.6$).

Conduction Relaxation

Dipole relaxation of bound charges is not the only type of relaxation that can be present in a disordered ionically conducting material. Charge migration, for example, also leads to relaxation processes. For a non-electronic conductor, charges are surrounded by a polarization cloud made of opposite sign counter charges. As

the ionic species move, the polarization cloud needs to move along in order to lead to an effective jump (otherwise the probability of the ion jumping back will be high). If the time period of the applied external field is longer than the time for the polarization cloud to successfully move, then the field supports the charge transport, contributing to the electrical relaxation. This results into an increase in the dielectric loss for decreasing frequency. We can again use the FDT and correlate the complex conductivity σ^*_{hop} due to ion hopping with the velocity correlation function [8]:

$$\sigma^*_{hop}(\omega) = \frac{Nq^2}{k_B T} \int_0^\infty \langle \sum_{i,j} v_i(0), v_j(0) \rangle e^{-j\omega t} \tag{2.13}$$

where N is the carrier number density, k_B the Boltzmann constant, T the temperature, q the elementary charge, and v_i the velocity of the i ion. Similarly, the self-diffusion coefficient D can be written as function of the velocity autocorrelation function:

$$D^*_{hop}(\omega) = \int_0^\infty \langle v(0), v(t) \rangle e^{-j\omega t}. \tag{2.14}$$

If the particles are not correlated, the hopping walk is random and there are no memory effects. In this case, the velocity correlation function is proportional to the diffusion coefficient D, and can be substituted in Eq. (2.13), obtaining:

$$\sigma^*_{hop}(\omega) = \frac{Nq^2}{k_B T} D^*_{hop}(\omega). \tag{2.15}$$

That for $\omega \to 0$, reduces to the Nerst-Einsten relation. This result implies that the DC and AC conductivity can be treated all the same, for periods below the relaxation time of the ionic conduction, and it is usually identified with the term DC or bulk conductivity. For frequencies above the relaxation time, a near constant loss dispersion arises. Interestingly enough, this behavior is common to all ionic conductors and it is usually referred as first universality. The exact explanation for the loss behavior at higher frequencies is still under great scientific debate and it is out of the scope of this thesis.

It is now clear how relaxations can arise both from rotational dipoles oscillations as well as translational charge movements. Although very different in nature, these different processes are entangled in the macroscopic measurable quantities of the complex conductivity and permittivity. Maxwell's equations, in fact, show how the current density J and the electric displacement time derivative $\partial D/\partial t$ are additive quantities, which in turn leads to the relation between the complex permittivity and conductivity $\sigma^* = i\omega\epsilon_0\epsilon^*$. In addition, as explained in this section, hopping

DC conductivity also generates relaxation phenomena that affect the permittivity spectra. Unlike dipole relaxation phenomena, charge diffusion does not cause a peak in the dielectric loss, but a decrease as a function of frequency with a fixed slope of one. Phenomenologically, in order to account for the different relaxation phenomena, the complex permittivity can be written as a combination of all the n dipole relaxation processes, described by the HN relation, and the contribution given by the relaxation that arises from the motion of charged species in the material, identified by the DC conductivity:

$$\epsilon^* = _\infty + \sum_{i=1}^{n} \frac{\Delta\epsilon_i}{(1 + (j\omega\tau_i)^\alpha)^\beta} - j\frac{\sigma_{DC}}{_0\omega}. \tag{2.16}$$

In many cases, the magnitude of the bulk conductivity is predominant compared to dipole relaxations and can hide the corresponding peaks in the dielectric loss data. It is useful therefore to introduce the conduction-free approach [9, 10], which takes advantage of the Kramers-Kronig transformations that relate the imaginary part of quantity with its real counterpart and vice versa. After the transformation, the dielectric loss reads:

$$\epsilon''_{der} \approx -\frac{\pi}{2}\frac{\partial\epsilon'(\omega)}{\partial ln(\omega)}. \tag{2.17}$$

Even though the dielectric loss is not exactly represented by Eq. (2.17), some features of the original dielectric loss are conserved in this derived expression. In particular, a relaxation peak in the dielectric loss ϵ'' corresponds to a minimum in $\partial\epsilon'/\partial ln(\omega)$. Because of the derivative function, peaks are narrower, and therefore more easily detectable. Lastly, the contribution of the DC conductivity is ruled out, since it does not show any frequency dependence in the real part of the permittivity.

Electrode Polarization

Relaxation peaks can also arise in the case of separation of charges at an interface. During the study of inhomogeneous materials like colloids or polymer blends, charges can accumulate at the interfaces between different boundaries of the material. This charge separation contributes to the dielectric loss, and since they can be separated over large distance, usually this contribution is substantial. Another example of charge separation can be given by the polarization of the non-blocking electrodes at low frequency. When an external electric field is applied to an ion conductor, the charged species diffuse through the medium. If they are given enough time, the ions will migrate toward one electrode, depleting the other one. The accumulation will be limited by the concentration gradient which counteracts the

electrostatic force of the electric field. At the steady state, the resulting non-constant charge density distribution generates a polarization that has opposite direction of the applied field. In this work, however, we will not consider both the effect on the permittivity given by charge separation that arises from inhomogeneous boundaries within the material and the ones created by the electrode polarization.

Dielectric Spectroscopy Measurements

Now that we have analyzed how relaxation peaks arise and what is their representation in the permittivity spectra, we will discuss how the dielectric spectra are experimentally measured. Among all the experimental techniques, dielectric spectroscopy (DS) is one of the most useful to study transport mechanisms since it measures the movement of electric dipoles in the presence of an electric field. DS usually ranges from 10^{-6} Hz to 10^{12} Hz, where longer wavelengths can probe, ion diffusion as well as dipole reorientation and rotation. In dielectric measurements, a perturbation created by a sinusoidal external voltage forces the dipoles within the sample to align with the created electric field and then relax to the new state. These processes result macroscopically in a change in the measured complex permittivity ϵ^*. Observed relaxation phenomena are usually attributed to the rotation of rotating dipoles, motion of charges and accumulation of charges at the interface.The most common experimental set-up consists of a sinusoidal voltage generator with known amplitude and frequency, and a meter that measures the resulting current. Assuming a linear response, if a sinusoidal voltage is applied, the resulting current will have the same frequency but will be shifted in phase:

$$v(t) = V_0 sin(\omega t) \rightarrow i(t) = I_0 sin(\omega t - \phi). \tag{2.18}$$

Since the analysis of the response in the time domain is usually very complex, the solution is often given in the frequency domain after the use of Fourier Transforms. If $V^*(\omega)$ and $I^*(\omega)$ are the Fourier Transforms of $v(t)$ and $i(t)$, respectively, then the complex impedance Z can be defined as:

$$Z^* = \frac{V^*(\omega)}{I^*(\omega)} = R + jX. \tag{2.19}$$

where the resistance R represents the real part of the complex impedance, while the reactance X its imaginary part. Through arithmetic transformations, all the other immittance functions can be evaluated (Tab. 2.1). Among these immittance functions, of particular interests are: the complex conductivity σ^* (i.e. the dimensionless counter part of the admittance), the complex permittivity ϵ^*, and the

Immittance Transformations				
	Modulus (M^*)	Impedance (Z^*)	Admittance (Y^*)	Permittivity (ϵ^*)
M^*	M^*	$(j\omega C_0)Z^*$	$(j\omega C_0)/Y^*$	$1/\epsilon^*$
Z^*	$M^*/(j\omega C_0)$	Z^*	$1/Z^*$	$1/[(j\omega C_0)\epsilon^*]$
Y^*	$(j\omega C_0)/M^*$	$1/Z^*$	Y^*	$(j\omega C_0)\epsilon^*$
ϵ^*	$1/M^*$	$1/[(j\omega C_0)Z^*]$	$Y^*/(j\omega C_0)$	ϵ^*

Table 2.1: Immittance functions transformations.

electric modulus M^*. Depending on the different formalism employed to analyze the data, different visualizations can be used for the understanding of the electrical response in ion conductors. For example, the dielectric response of materials is usually analyzed with the dielectric formalism (permittivity, conductivity, and electric modulus), while electrolytes–electrode interfacial response uses the impedance representation (argand plot, impedance Bode plots). It is important to stress that, regardless of the used formalism, the represented data is the same, and different visualization techniques can be employed to analyze different aspect of the conduction phenomena. The impedance data are usually represented on a Nyquist plot, representation on the complex plane of the real and imaginary part of the impedance at different frequencies, or on a Bode plot, where the real and imaginary part are plotted as a function of frequency. The impedance is then fitted to lumped electrical parameters such as resistors and capacitors, in order to find the characteristic time constants of the system, its bulk resistivity, or the interfacial resistance in case of reaction at the electrode–material interface. Each electrical element is assigned to an individual physical processes. Through the use of a fit the time constants for these processes are then calculated. Nevertheless, there are two main drawbacks with this approach. The first one is that fitting the impedance through electrical elements does not provide a univocal output (the same set of data can fit different electrical representations), forcing to make a priori assumptions on the different transport mechanisms. The second major problem is represented by the high frequency behavior of ionically conducting materials, referred as universal response, which cannot be fitted by any ideal electrical component. The power law dependence at high frequency of the conductivity, typical of the universal response, is usually described by a so-called universal capacitor Q or constant phase element (CPE), characterized by the complex admittance $Y_Q = Qj\omega^n$. Even though with the introduction of the universal capacitor data can be fitted also at higher frequencies and its extended use in the literature, its physical meaning and validity have been criticized [11–13]. Unlike impedance spectroscopy, dielectric spectroscopy data

are usually visualized in terms of conductivity, permittivity, or electric modulus. Figure 2.2 shows typical conductivity, permittivity, and modulus plots for an ionic conducting material. From the analysis of these plots, the dynamics of ion transport in different materials can be understood. For instance, Figure 2.2(a) shows the real and imaginary parts of the complex conductivity for an ion conducting polymer clay composites (PEO_{20}-$LiCF_3SO_3$) [14]. In the real part of the conductivity, three different regimes can be identified. A low frequency region (below 10 Hz) where the conductance increases with frequency. This region corresponds to the electrode polarization where the accumulation of charges at the non-blocking electrode interface leads to an apparent decrease in conductivity. A medium frequency region (between 10 and 10 kHz) where the conductance is independent from the frequency. Here, ions diffuse within the medium through subsequent hopping from one site to another and it is usually used as reference for the bulk conductivity of the material. This type of long range conductivity is believed to need a sort of percolation activation in order to be observed. Another loss region can be observed at high frequency (above 10 kHz), commonly identified as near constant loss (NCL) or first universality, where the conductance shows a power law dependence with frequency. While these three regimes are evident in the real part of the conductivity, they are not fully present in the imaginary counterpart spectrum: the electrode polarization onset as well as the bulk conductivity are identified by a maximum and a minimum, respectively, which is greatly convenient for fitting purposes. However, there is no trace of the onset of the dispersive regime at higher frequency. While, the complex conductivity underlines mainly charge motion mechanisms, the permittivity spectra are extremely useful to probe dielectric relaxation phenomena. Figure 2.2(b) shows the complex permittivity for PEO_{20}-$LiCF_3SO_3$. For a non-ohmic process, the dielectric permittivity shows a strong dependence at low frequencies, due to the electrode polarization effects, and a plateau at higher frequency, corresponding to the ion diffusive limit. Every successive relaxation process is identified by a step-like decrease, from which the dielectric strength $\Delta\epsilon$ can be calculated. In contrast, in the permittivity loss a relaxation event is indicated by a peak. Depending by the number of contribution of relaxation processes, peaks can be overlapping, and therefore, fitting with previously described functions is necessary to exactly identify the time constants for these phenomena. As previously mentioned, the ionic diffusive regime is indicated by a decrease in the permittivity loss with a unitary slope. Electric modulus can be alternatevely used to measure relaxation peaks and dielectric strength, with the advantage of a non-logarithmic scale that in certain

cases shows more features compared to the complex permittivity (Fig. 2.2(c)). Now that we have analyzed why relaxation phenomena arise and their representation in spectroscopy data, we can discuss what are the actual microscopic mechanisms of ion transport in polyelectrolytes.

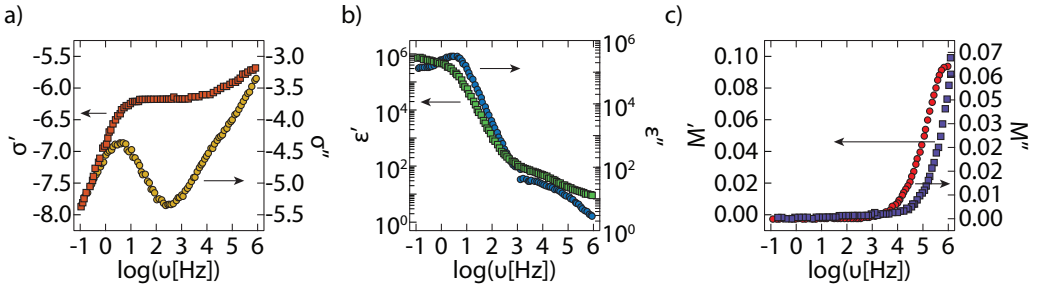

Figure 2.2: Conductivity, Permittivity, and Electric Modulus comparison in PEO_{20}-$LiCF_3SO_3$. (a) Real (orange squares) and imaginary (yellow circles) parts of the conductivity σ, (b) real (green squares) and imaginary (blue circles) parts of the permittivity ϵ, (c) real (purple squares) and imaginary (red circles) parts of the electric modulus M for PEO_{20}-$LiCF_3SO_3$ measured at 263 K. The data is adapted from [14] and reproduced with publisher consent.

2.4 Ion Conduction Phenomena in Polymers

Ion conduction in polymers is a rather complex subject to analyse experimentally. Measurable quantities, like electrical conductivity, are the result of the sum of the contributions given by a variety of charge carriers (e.g. cations, anions and protons), charge diffusion, dipole reorientation and relaxation, segmental motions and so on. It is therefore hard to probe individual contribution. The simplest relation that expresses the total DC conductivity of an ion conductor can be given as:

$$\sigma = \sum_i n_i \mu_i q_i \tag{2.20}$$

where n_i is the charge carrier density, q_i the charge and μ_i the electrical mobility of the $i-th$ species. In the particular case of pectin and HEA–AA, where only divalent ions are conducting, the overall conductivity needs to include only that ionic species and water. The bulk conductivity thus reads:

$$\sigma = n_{M^{2+}} \mu_{M^{2+}} q_{M^{2+}} + n_{H_2O} \mu_{H_2O} q_{H_2O}. \tag{2.21}$$

In this section, we will focus on the mechanisms behind of ionic conduction, neglecting the contribution given by water molecules and leaving that analysis for the following section.

Ion Conduction

Generally speaking, ionic conduction in crystalline structures occurs when ions can hop from one site to another. The ion diffusion is driven by structural defects in the structure: Schottky defects result in the vacancy mechanism, where ions jump into a nearby unoccupied lattice site; Frenkel defects, which lead to the interstitial mechanism, where an ion that occupies an interstitial site moves to one of the neighboring sites. For amorphous and glassy polymers, one can imagine a similar situation, where the only difference is that instead of having a periodic structure and a single activation energy for the ion hopping, ions encounter a disordered media with a distribution of energy barriers. In the simple assumption of a 1D model for an ionic conductor, ions are vibrating within their potential well and have a finite probability of overcoming the energy barrier ΔH_m, proportional to $e^{-\Delta H_m/k_BT}$. The transition rate between two equilibrium states is given by [15]:

$$\Gamma = \nu_0 e^{-\Delta S_m/k_BT} e^{-\Delta H_m/k_BT} \tag{2.22}$$

where ΔS_m andΔH_m corresponds, respectively, to the entropy and enthalpy change, and ν_0 is the attempt frequency of the jump. When no electric field is applied, the probability of a forward and backward jump will be the same, resulting in no net transport of ions through the material. Upon the application of the external field, the forward jump frequency Γ_f will be decreased by the quantity $qdE/2$, while the backward jump frequency quantity Γ_b will be increased of the same amount:

$$\begin{aligned} \Gamma_f &= \nu_0 exp(-\Delta S_m/k_BT) exp(-\frac{-\Delta H_m - qdE/2}{k_BT}) \\ \Gamma_b &= \nu_0 exp(-\Delta S_m/k_BT) exp(-\frac{-\Delta H_m + qdE/2}{k_BT}). \end{aligned} \tag{2.23}$$

The current density is given by the difference between the forward and backward frequency:

$$j = \frac{1}{2} nqd(\Gamma_f - \Gamma_b) \tag{2.24}$$

where n is the concentration of the hopping ions. Substituting Eq. (2.23) in Eq. (2.24), and under the assumption that the thermal energy is much bigger than the potential energy, that is $qdE \gg k_BT$, we can use the equality $e^x - e^{-x} = 2x$. Eq. (2.24) becomes:

$$j = \frac{1}{2} nqd\nu_0 exp(-\frac{\Delta S_m}{kb_T}) exp(-\frac{\Delta H_m}{kb_T}) \frac{qdE}{k_BT} = \frac{nq^2 d^2 \Gamma}{2k_BT} E \tag{2.25}$$

Defining the diffusivity $D = d^2\Gamma/2$, we obtain the Nerst-Einstein equation in 1D:

$$\sigma = \frac{nq^2}{k_BT} D. \tag{2.26}$$

This 1D simple model is important to understand the dynamics involved in ion conduction, but is far from providing a full picture of the actual conduction phenomena. In fact, even in the case of a successful jump, long range conduction is still impaired. The concept of percolation arises in order to connect microscopic successful jumps to mesoscopic conduction. According to the percolation theory, in order to record long distance conductivity, the percolation threshold needs to be overcome. Several models have been developed over the years in order to account for the microscopic behavior of the ions in a polymer matrix according to the percolation theory. Here, we will give an outline of two of the most significant, namely the Random Walk Barrier and the Bond Percolation Theory.

Random Walk Barrier (RWB)

The random walk barrier (RWB) describes the random walk of charge carriers in disordered solids through the use of a hopping-time distribution function, calculated via the continuous random walk approximation [16–18]. For non-interacting particles that occupy sites at constant distance, let P_s the probability of the particle to be at a site, and $\Gamma(s \rightarrow s^{'})$ the probability per unit time for a jump from site s to $s^{'}$. The equation of motion is:

$$\frac{d}{dt}P_s = \sum_{s^{'}}(\Gamma(s^{'} \rightarrow s)P_{s^{'}} - \Gamma(s \rightarrow s^{'})P_s). \tag{2.27}$$

The microscopic fluctuations can be correlated to the macroscopic diffusivity via the fluctuation dissipation theorem:

$$D(\omega) = \int_0^{-\infty} \langle v(0)v(t)\rangle e^{-j\omega t}dt \tag{2.28}$$

where $\langle v(0)v(t)\rangle$ is the autocorrelation velocity function. Diffusivity and conductivity are again related through the Nerst-Einstein equation (Eq. (2.26)). If we consider an energy landscape where the minima are the same, the maxima have a distribution described by $p(E)$, and the jump rates are symmetric, Equation (2.27) reads:

$$\frac{d}{dt}P_s = \sum_{s^{'}} \Gamma(s, s^{'})(P_{s^{'}} - P_s) \tag{2.29}$$

with $\Gamma(s^{'} \rightarrow s) = \Gamma(s \rightarrow s^{'}) = \Gamma(s, s^{'})$.The jumping rates probability have an Arrhenius form $\Gamma = \nu_0 e^{-E/k_B T}$. Long range conduction occurs when the thermally activated hopping overcomes the largest of the energy barrier E_c. When the fraction of individual conduction links reaches a critical number, the percolation threshold

p_c, an infinite cluster forms and long range conductivity occurs. The activation energy for the process can be evaluated as:

$$\int_0^{E_c} p(E)dE = p_c. \tag{2.30}$$

Modeling ion conduction as probability functions of hopping rates has two implications: (i) at low temperature the charge carriers almost always choose the path with lowest energy barrier, which implies that if the charge jumps forward most likely it will jump back in the next hopping event; (ii) at infinite time, charges will have the same probability to overcome the barrier, leading to macroscopic conductivity. The second statement introduces a characteristic time τ_c which is the time needed for a charged particle to overcome the energy barrier and has the same Arrhenius form of the jumping rates probability and determines for the characteristic time that marks the onset of the dispersive regime [19]. Solving for the probability distribution and excluding the electrode polarization effect, the complex conductivity can be computed from:

$$\sigma^* = \sigma_{DC} \frac{j\omega\tau_c}{ln(1 + j\omega\tau_c)}. \tag{2.31}$$

Dynamic Bond Percolation (DBP) Theory

Dynamic bond percolation (DBP) theory has a similar approach compared to the random walk barrier in the sense that the particles have a probability of jumping from one site to another neighboring site. In the DBP, however, these probabilities are allowed to change with time, to take into account the segmental motion of the polymer chains [20–23]. In fact, a jump that originally is not permitted, after the rearrangement of the polymer chain has a higher likelihood to occur. Differently than the RBW where only one time constant was defined, here we need to define two time constants: τ_{hop} which corresponds to the average time that the particles take to hop, and τ_{ren} which corresponds to the average time that the polymer chain takes to reorient itself (renewal time). In the easiest 1D case, for ions moving in a dynamic lattice, the master equation that describes the probability of finding a particle at the site i at time t reads:

$$\frac{d}{dt}P_s = \sum_{j \neq i} (P_j(t)w_{j \to i} - P_i(t)w_{i \to j}) \tag{2.32}$$

where $w_{i\to j}$ represent the probability per unit time of the particle jumping from site j to i so that $n_c w\tau_{hop} = 1$, with n_c the coordination number of the charge. This probability depends on both the site position as well as their probabilities:

$$w_{i\to j} = \begin{cases} w \text{ or } 0 & \text{when } (i,j) \text{ are neighbours} \\ 0 & \text{when } (i,j) \text{ are not neighbours} \\ 1 - (w_{i\to j} + w_{j\to i}) & \text{for } i = j \end{cases} \tag{2.33}$$

$$w_{i\to j} = \begin{cases} 0 & \text{bond } (i,j) \text{ not available} \\ w & \text{bond } (i,j) \text{ available} \end{cases}. \tag{2.34}$$

The final probability for the occupation of the site r starting from the site i, and after N+1 renewal processes, depends only on the previous renewal state N, given the sequential nature of hopping:

$$P^{N+1}(r) = \sum_i P^N(i) P^1(r-1). \tag{2.35}$$

Using this equation of motion, one can calculate the mean displacement $\langle x^2 \rangle$ and the diffusivity D(through the fluctuation dissipation theorem):

$$D = \frac{\langle x^2 \rangle}{\tau_{ren}}. \tag{2.36}$$

Three different regimes that relate the observation time τ_{obs} (frequency of the applied external field), the hopping time τ_{hop}, and the renewal time τ_{ren}, can be observed according to the DBP: (i) $\tau_{obs} \gg \tau_{ren} \gg \tau_{hop}$, (ii) $\tau_{ren} \gg \tau_{obs} \gg \tau_{hop}$ and (iii) $\tau_{obs} \gg \tau_{hop} \gg \tau_{ren}$. Case (ii) describes a percolation model where there is no rearrangement of the network with time. Case (iii) describes a diffusive behavior where the jumping rate depends on the availability of a specific site. Finally, case (i) represents the case in which a particle after multiple jumps has explored all the connected region. However, after a renewal event, new jumping probabilities are established, i.e., new sites become available for hopping, and the particle can further diffuse in the material.

Macroscopic Models

Percolation theories can relate microscopic fluctuations and motions to macroscopic measurable quantities such as diffusion. However, they fail in providing detailed explanation of motion of the particles involved in the conduction process. There are several ways ion can move within a polymer matrix [24]. Vehicular diffusion

occurs when the polymer–salt complex also embeds certain amount of solvents (as organic solvents or water). In this case, the salt diffuses through the network via the solvent, dragging along its solvation shell. Inter- or intrachain transport mainly occurs in low concentration solvent or solvent free, and are related to the motion of the polymer backbone usually when above its glass transition temperature. On the contrary, structural diffusion is less dependent from the segmental motion and involves direct ion hopping from one coordination site to another. In the case of high molecular weight polymers with low solvent concentration, vehicular diffusion is unlikely, and only segmental related mobility and structural diffusion are allowed. The Arrhenius model and the Vogel- Fulcher -Tammann (VFT) model can be used in order to discriminate between these two phenomena. The Arrhenius model is described by the equation:

$$\sigma_{DC} = \sigma_0 exp(-\frac{E_a}{k_B T}) \tag{2.37}$$

where σ_0 and E_a are the pre-exponential factor and the activation energy, respectively. When the Arrhenius relationship is fulfilled, one can conclude that the charge motion is not influenced by the motion of the polymer network and ionic conduction occurs via structural diffusion. The activation energy can be interpreted as the bottleneck for percolation to occur, that is the highest energy barrier to overcome for the formation of a percolative path. On the contrary, the VFT model is a phenomenological expression of polymers when the glass transition temperature is crossed:

$$\sigma = AT^{-1/2} exp(-\frac{B}{k_B(T - T_0)}). \tag{2.38}$$

In this case, one can conclude that the ion transport does not occur through structural diffusion, but also polymer's segmental motion is involved to favor ion hopping.

2.5 Water Contribution to Ion Conduction

In the previous section, the phenomena that describe ion transport have been discussed. In the analysis, for clarity, the contribution of water in the transport mechanisms was neglected. However, water molecules can play a major role in the electrical properties of a polyelectrolyte. First of all, it is important to underline, that the characteristics of water molecules present inside a low concentration solvent, or solvent free polymer, greatly differ from those of bulk water. Generally speaking, water can affect conductivity in multiple ways both contributing directly to the conduction and by lowering the energy barriers that ions need to overcome in order to diffuse in the material.

Let us consider again the general conductivity equation given in Eq. (2.21), explicitly calling for water contributions[2]:

$$\sigma(RH) = n_{M^{2+}}(RH)\mu_{M^{2+}}(RH)q_{M^{2+}} + n_{H_2O}\mu_{H_2O}q_{H_2O}. \tag{2.39}$$

Recalling the acid dissociation described in Eq. (2.1), we can notice how the equilibrium will move to the right for a higher water concentration. This implies that for a higher water content, more carboxylic acid groups deprotonate resulting in a higher protons concentration n_{H_2O}. Water molecules, however, can also affect the ionic term in Eq. (2.39). Water can increase the mobility of the cations, by providing additional paths for transport process [25, 26]. This phenomenon occurs either via the creation of water channels that allow long range ion drifting, or by increasing the segmental motion of the polymer favored by the plasticizing effect of water molecules. Furthermore, water concentration can modify the number density of ions contributing to the polymer's conductivity caused by screening effect of water molecules for charged particles: water molecules compete with carboxyl and hydroxyl groups on the polymer backbone for the formation of coordination bonds that cations want to establish, effectively lowering the energy barrier and the strength of that bond. It is important to understand the role that water plays in the conduction mechanism in pectin and HEA–AA, especially in view of the thermal response of these polymers. In Chapters 3 and 4, we will show how a specific water content is crucial to register a high temperature responsivity [27]. This can be shown in a first approximation considering the total conductivity as the sum of the contribution of the ionic conductivity and the proton conductivity as a function of temperature:

$$\sigma(T) = \sigma_{ion}f(T) + \sigma_{H_2O}g(T) \tag{2.40}$$

where $f(T)$ and $g(T)$, represent how the ionic and proton conductivity change as a function of temperature. Bulk water slightly increases conductivity as temperature raises, mainly due to changes in the viscosity. On the other hand, the ion conductivity strongly depends on temperature, being a thermally activated process, and it is orders of magnitude higher compared to water. Therefore, the overall temperature response is mainly provided by the ionic species in the polymer. However, when the water concentration is too high, the absolute conductivity provided by proton transport is much higher and dominates the overall conductivity ($\sigma_{H_2O} >> \sigma_{ion}$), masking the temperature responsivity of the ionic species in the polymer matrix. An optimal water content is therefore required to record the temperature responsivity of the ions.

[2]The water dependence is described as a function of the relative humidity RH.

Time Humidity Superposition Principle (THSP)

Deconvoluting the single contributions of water from the overall conductivity can be hard, since multiple effects are combined with the ion transport in one single property, the electrical conductivity. For the particular case of the temperature responsive polymers we are analyzing, the contribution of proton conduction to the overall conductivity can be differentiated from the indirect effect water has on the ion transport, by looking at the temperature-conductivity function. In fact, proton conduction shows a weak relation with temperature, while the ion hopping has a stronger dependence from temperature. Direct proton conduction can also be analyzed by the change of bulk conductivity as a function of external relative humidity, and therefore water content present in the matrix. This approach allows to separate the effect of the direct contribution that protons have on conductivity, from the indirect one on the ions and polymer energetic landscape, which effectively favors ion transport. Discriminating between the effect that water has on the ion number density and the ion mobility can be complex because they both appear in the same term in the conductivity. Nonetheless, recently, the time humidity superposition principle (THSP) has been employed to further analyze the impact of water on the ion conduction [28–30]. The THSP is a scaling law that follows the similar time temperature superposition principle (TTSP). The TTSP is based on the empirical observation that the real part of the conductivity of many materials has a temperature independent shape. For example, Figure 2.3(a) shows different conductivity spectra for different temperature as measured in the polycrystal niobium-doped barium stannate ($BaSn_{1-x}Nb_xO_3$) [31]. These spectra can be scaled with an appropriate function F so that:

$$\frac{\sigma^{'}(\omega)}{\sigma_{DC}} = F(\frac{\omega}{\omega_0}). \tag{2.41}$$

Here, ω_0 is a scaling parameter used to super impose the real conductivity at different temperatures onto a so-called master curve (Fig. 2.3(b)) [31]. The most common approach to do so is to use as scaling parameters ω_0, the onset frequency of the dispersive region ω^*. In the case that $log(\sigma_{DC})$ is proportional to $log(\omega_0)$, the Summerfield scaling is fulfilled, the scaling parameter is $\omega^* = \sigma_{DC}T$, and the corresponding scaling function is given by:

$$\frac{\sigma^{'}(\omega)}{\sigma_{DC}} = F(\frac{\omega}{\sigma_{DC}T}). \tag{2.42}$$

A similar approach can be used when looking at the THSP. Neglecting the proton conductivity, we can state that the number of ions participating to the conduction

does not depend on the frequency, but only to the RH level. On the other hand, the ion mobility is affected both by the angular frequency and the water content. In this context, the onset frequency ω^* describes the passage from long range diffusive transport to the dispersive regime, where the observation time is shorter than the hopping time. For increasing mobility, the time needed to enter the dispersive regime will be shorter, implying that the inverse of the offset frequency is proportional to the mobility. Interestingly, in case the Summerfield scaling is fulfilled, the bulk conductivity is proportional to the onset frequency, leading to [28–30]:

$$\mu \propto \omega^* \propto \sigma. \tag{2.43}$$

Eq. 2.43 has important implications on the effect of water on the ion conductivity: (i) if the slope of the line connecting the logarithm of the onset frequency with the logarithm of the corresponding conductivity at different RH is one, then water molecules only affect the ion mobility, without changing the number density of ionic charges. In this case, the total conductivity (where proton conduction has been neglected) can be written as a function of humidity and frequency as:

$$\sigma(\omega, RH) = n\mu(\omega, RH)q. \tag{2.44}$$

On the contrary, if (ii) the slope of the line connecting the logarithm of the onset frequency with the logarithm of the corresponding conductivity at different RH is greater than one, the presence of water molecules has also an impact on the energy barriers which leads to lowering the activation energy and the generation of more ions for higher water concentration. The THSP can therefore be applied to try to deconvolute the effect that water has on the mobility of the conducting ionic species from the one on the number density of ionic charges.

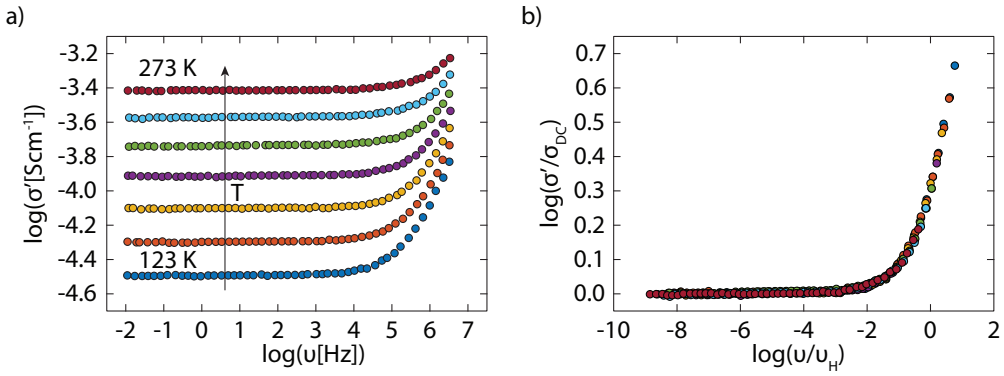

Figure 2.3: Time Temperature Superposition Principle. (a) Real part of the conductivity at different temperatures measured for a $BaSn_{1-x}Nb_xO_3$ sample: blue circles 123 K, orange circles 148 K, yellow circles 173 K, purple circle 198 K, green circles 223 K, light blue circles 248 K, red circles 273 K. (b) Superimposed conductivity spectra according to the scaling function. The data is adapted from [31] and reproduced with publisher consent.

Methods to Calculated the Onset Frequency

The application of the THSP requires the computation of the frequency at which the transport becomes dispersive. The most common and applied strategy is based on the Almond-West formalism and the Jonscher power law, according to which the real conductivity can be expressed as:

$$\sigma^{'}(\omega) = \sigma_{DC}[1 + (\frac{\omega}{\omega^*})^n]. \tag{2.45}$$

To find the onset frequency ω^*, it is enough to find the frequency at which $\sigma^{'}(\omega^*) = 2\sigma_{DC}$. Even if this approach is widely used, it has been critiqued because the Jonscher power law is not based on any physical model and it leads to results at low frequency that do not correspond to experimental data [32]. A sounder approach consists on fitting the conductivity data with the RWB in order to find the characteristic time τ_C, which corresponds to the beginning of the dispersive regime. The only drawback with this method is that the RWB does not take into account polymer segmental motion and in some case can provide inaccurate fit. A valid alternative is the application of the Electrode Polarization model developed by MacDonald and Cohelo [33–36], where the polarization effect at the blocking electrode is modeled as an effective dipole with Debye relaxation:

$$\epsilon^*(\omega) = \epsilon_S + \frac{\Delta\epsilon}{1 + j\omega\tau_{EP}} \tag{2.46}$$

where τ_{EP} is the time constant for the polarization build up and $\Delta\epsilon = \epsilon_{EP} - \epsilon_S$ is the apparent increase in the polarization due to the charge accumulation. The onset

frequency can be found by fitting the tangent loss function:

$$tan\delta = \frac{\omega\tau_{EP}}{1 + j(\omega^2/\omega^*)\tau_{EP}}. \tag{2.47}$$

Also this model, however, gives inaccurate result for higher ion concentration and interacting particles. Geometrical procedures that involve the fit of the electric modulus M with Debye or non-Debye functions, as well as the calculation of the flex point (e.g. $max(\partial^2\sigma'/\partial\omega^2)$) are also valid alternatives that can be used to compute the onset frequency. In our work, we will apply the AW formalism and the RWB to find the onset frequency and compare them to check the quality of the data.

References

[1] T. H. Kim, Z. Zhou, Y.S. Choi, V. Costanza, L. Wang, Y. Yun, H. Kang, S. Kim, and C. Daraio. Flexible biomimetic block copolymer composite for temperature and long-wave infrared sensing. *Nature Communications, under review*, 2022.

[2] P. Debye. Einige resultate einer kinetischen theorie der isolatoren. *Physikalische Zeitschrift*, 97, 1912.

[3] P. Debye. Zur theorie der anomalen dispersion im gebiete der langwelligen elektrischen strahlung. *Deutsche Physikalische Gesellschaft*, 97, 1913.

[4] G. Adam and J. H. Gibbs. On the temperature dependence of cooperative relaxation properties in glass-forming liquids. *The Journal of Chemical Physics*, 43(1):139–146, 1965.

[5] K. Schmidt-Rohr and H. W. Spiess. Nature of nonexponential loss of correlation above the glass transition investigated by multidimensional nmr. *Physical Review Letters*, 66:3020–3023, 1991.

[6] E. Weeks, J. C. Crocker, A. C. Levitt, A. Schofield, and D. A. Weitz. Three-dimensional direct imaging of structural relaxation near the colloidal glass transition. *Science*, 287(5453):627–631, 2000.

[7] S. Havriliak and S. Negami. A complex plane analysis of -dispersions in some polymer systems. *Journal of Polymer Science Part C: Polymer Symposia*, 14 (1):99–117, 1966.

[8] R. Kubo. Statistical-mechanical theory of irreversible processes. I. General theory and simple applications to magnetic and conduction problems. *Journal of the Physical Society of Japan*, 12(6):570–586, 1957.

[9] P. A. M. Steeman and J. van Turnhout. Fine structure in the parameters of dielectric and viscoelastic relaxations. *Macromolecules*, 27(19):5421–5427, 1994.

[10] M. Wübbenhorst and J. van Turnhout. Analysis of complex dielectric spectra. i. one-dimensional derivative techniques and three-dimensional modelling. *Journal of Non-crystalline Solids*, 305:40–49, 2002.

[11] C. T. Moynihan. Analysis of electrical relaxation in glasses and melts with large concentrations of mobile ions. *Journal of Non-Crystalline Solids*, 172-174: 1395–1407, 1994.

[12] C. T. Moynihan. Description and analysis of electrical relaxation data for ionically conducting glasses and melts. *Solid State Ionics*, 105(1):175–183, 1998.

[13] I.M. Hodge, K.L. Ngai, and C.T. Moynihan. Comments on the electric modulus function. *Journal of Non-Crystalline Solids*, 351(2):104–115, 2005.

[14] T. Dam, S. S. Jena, and D. K. Pradhan. The ionic transport mechanism and coupling between the ion conduction and segmental relaxation processes of peo 20-licf 3 so 3 based ion conducting polymer clay composites. *Physical Chemistry Chemical Physics*, 18(29):19955–19965, 2016.

[15] C. Zener and R. H. Fowler. Non-adiabatic crossing of energy levels. *Proceedings of the Royal Society of London. Series A, Containing Papers of a Mathematical and Physical Character*, 137(833):696–702, 1932.

[16] Jeppe C. Dyre. A simple model of ac hopping conductivity in disordered solids. *Physics Letters A*, 108(9):457–461, 1985.

[17] Jeppe C Dyre and Thomas B Schrøder. Universality of ac conduction in disordered solids. *Reviews of Modern Physics*, 72(3):873, 2000.

[18] Thomas B Schrøder and Jeppe C Dyre. Computer simulations of the random barrier model. *Physical Chemistry Chemical Physics*, 4(14):3173–3178, 2002.

[19] J. C. Dyre, P. Maass, B. Roling, and D. L. Sidebottom. Fundamental questions relating to ion conduction in disordered solids. *Reports on Progress in Physics*, 72(4):046501, 2009.

[20] S. D. Druger, A. Nitzan, and M. A. Ratner. Dynamic bond percolation theory: A microscopic model for diffusion in dynamically disordered systems. I. Definition and one-dimensional case. *The Journal of Chemical Physics*, 79(6): 3133–3142, 1983.

[21] S. D. Druger, M. A. Ratner, and A. Nitzan. Polymeric solid electrolytes: Dynamic bond percolation and free volume models for diffusion. *Solid State Ionics*, 9:1115–1120, 1983.

[22] S. D. Druger, M. A. Ratner, and A. Nitzan. Generalized hopping model for frequency-dependent transport in a dynamically disordered medium, with applications to polymer solid electrolytes. *Physical Review B*, 31(6):3939, 1985.

[23] M. A. Webb, B. M. Savoie, Z.-G. Wang, and T. F. Miller III. Chemically specific dynamic bond percolation model for ion transport in polymer electrolytes. *Macromolecules*, 48(19):7346–7358, 2015.

[24] C. Y. Son and Z.-G. Wang. Ion transport in small-molecule and polymer electrolytes. *The Journal of Chemical Physics*, 153(10):100903, 2020.

[25] F. Lecomte, J. Siepmann, M. Walther, R.J. MacRae, and R. Bodmeier. Polymer blends used for the aqueous coating of solid dosage forms: Importance of the type of plasticizer. *Journal of Controlled Release*, 99(1):1–13, 2004.

[26] G. I. Olivas and G. V. Barbosa-Cánovas. Alginate–calcium films: Water vapor permeability and mechanical properties as affected by plasticizer and relative humidity. *LWT-Food Science and Technology*, 41(2):359–366, 2008.

[27] V. Costanza, L. Bonanomi, G. Moscato, L. Wang, Y. S. Choi, and C. Daraio. Effect of glycerol on the mechanical and temperature-sensing properties of pectin films. *Applied Physics Letters*, 115(19):193702, 2019.

[28] C. Cramer, S. De, and M. Schönhoff. Time-humidity-superposition principle in electrical conductivity spectra of ion-conducting polymers. *Physical Review Letters*, 107(2):028301, 2011.

[29] S. De, C. Cramer, and M. Schönhoff. Humidity dependence of the ionic conductivity of polyelectrolyte complexes. *Macromolecules*, 44(22):8936–8943, 2011.

[30] S. De, A. Ostendorf, M. Schönhoff, and C. Cramer. Ion conduction and its activation in hydrated solid polyelectrolyte complexes. *Polymers*, 9(11):550, 2017.

[31] P. Singh, O. Parkash, D. Kumar, et al. Scaling of low-temperature conductivity spectra of basn1- x nb x o 3 (x 0.100): Temperature and compositional-independent conductivity. *Physical Review B*, 84(17):174306, 2011.

[32] J. R. Macdonald. Addendum to "Fundamental questions relating to ion conduction in disordered solids.". *Journal of Applied Physics*, 107(10):101101, 2010.

[33] J. R. Macdonald. Theory of ac space-charge polarization effects in photoconductors, semiconductors, and electrolytes. *Physical Review*, 92:4–17, 1953.

[34] R. Coelho. Sur la relaxation d'une charge d'espace. *Revue de Physique Appliquée*, 18(3):137–146, 1983.

[35] R. Coelho. On the static permittivity of dipolar and conductive media—an educational approach. *Journal of Non-Crystalline Solids*, 131:1136–1139, 1991.

[36] R. J. Klein, S. Zhang, S. Dou, B. H. Jones, R. H. Colby, and J. Runt. Modeling electrode polarization in dielectric spectroscopy: Ion mobility and mobile ion concentration of single-ion polymer electrolytes. *The Journal of Chemical Physics*, 124(14):144903, 2006.

Chapter 3

EFFECT OF GLYCEROL ON THE MECHANICAL AND TEMPERATURE-SENSING PROPERTIES OF PECTIN FILMS

V. Costanza, L. Bonanomi, G. Moscato, L. Wang, Y. S. Choi, and C. Daraio. Effect of glycerol on the mechanical and temperature-sensing properties of pectin films. *Applied Physics Letters*, 115(19):193702, 2019.

3.1 Chapter Preamble

Pectin's remarkable temperature response can be exploited for the fabrication of ultrathin DHF sensors. However, the origin of the temperature response needs to be understood in order to take advantage of the full potential of the material's properties. In particular, the interaction between the crosslinking ions, the polymer backbone, and water molecules play a crucial role in the temperature responsivity recorded in pectin films. In this chapter, we will modify water concentration by adding a plasticinzing molecule, glycerol, and study the effect on the overall properties of pectin films, with a particular focus on the temperature sensitivity.

3.2 Abstract

Temperature-sensitive films embedded in electronic skins (e-skins) can provide temperature feedback to robots, high-tech prostheses, and wearable devices for health care monitoring. Pectin-based films have shown a temperature response at least two orders of magnitude higher than previously reported temperature-sensing materials. However, they are not easily stretchable and tearable, which limit their applications as e-skins that require repetitive bending and mechanical stresses. Here, we show how the addition of glycerol as a plasticizer in the fabrication of pectin-based films improves their mechanical properties. We report how the enhancement of the mechanical performance is accompanied by a decrease in the temperature responsivity. Through thermogravimetric analysis, we show that this reduction in responsivity can be associated with water retention due to the addition of the plasticizer. The link between the water content and the temperature response demonstrates that a dehydrated status of pectin is crucial to record its high temperature responsivity.

Combining electrical and thermal characterization with the tensile strength test, we estimate the optimal concentration of glycerol for improving the mechanical properties without compromising the temperature response of the pectin films.

3.3 Introduction

Electronic skins (e-skins) are flexible electronic devices engineered to mimic human skin and its ability to map continuous external physical stimuli, such as temperature, pressure, and strain. Applications of e-skins are mainly pursued in robotics and prosthetics to provide temperature feedback for controls and responsiveness to environmental changes [1–4] and to enhance human-robot interactions [5]. Recently, e-skins have also been incorporated into wearable devices, for example, to map temperature for early diagnosis of diseases and chronic conditions [4, 6].

Creating e-skins with flexible, stretchable, and robust sensory networks is a scientific and an engineering challenge. Its pursuit has pushed a quest for new materials that can measure complex stimuli over large areas while withstanding external mechanical solicitations. While pressure sensitive e-skins have reached a significant maturity, temperature sensing still presents considerable limitations. In particular, solutions able to provide measurements over a wide range of temperatures have limitations in response [7–12], whereas devices with acceptable responsivity work over only very narrow temperature ranges [13, 14]. Recently, pectin-based films have been demonstrated to be highly responsive over an extended temperature range of 50 °C [15]. Large area pectin films have also been successful in mapping temperature effectively over surfaces without the need for complex pixel-addressed electronic arrays, typical e-skin architectures [15].

Pectin is a structurally complex polysaccharide contained in the primary cell wall of plant cells. Its structure is heterogeneous, depending on the plant origins and extraction methods. Different galacturonic acid-rich polysaccharides have been identified as components of pectin compounds, such as homogalacturonan, rhamonogalacturonan (I and II), xylogalacturonan, and arabinogalactan. Despite their complexity, the structural behavior of pectin networks is determined by homogalacturonan that constitutes at least 65% of the pectin molecule. Homogalacturonan is made up of α-(1-4)-linked galacturonic acid residues (polygalacturonic acid), in which part of the carboxyl groups are esterified by methyl groups [16] (Fig. 3.1(a)). The degree of esterification determines the crosslinking mechanism. In highly esterified pectin, at acidic conditions, individual chains are crosslinked together through hydrogen

bridging and hydrophobic interactions. On the contrary, the low-ester crosslinking of pectin is mediated by divalent metallic ions. The carboxylated groups on the backbone are strongly hydrated when dissolved in water. The charged moieties on the side chains of pectin form stable electrostatic interactions with the cations (coordinate and cooperative bonds), promoting the formation of junction zones among neighboring chains [17, 18] (Fig. 3.1(b)). The crosslinking extent depends on different factors, such as pH or electronic affinity of the divalent cations. Among all these parameters, temperature greatly affects the crosslinking density of the pectin network. The temperature increase causes a rearrangement of the polymer backbone and of the ions, leading to a higher number of mobile cations or to an increase in their mobility. As a result, the conductivity exponentially increases with temperature [15, 19, 20]. The weak strength of the ion-polymer interaction is most likely responsible for the recorded temperature response. These weak forces, combined with the intrinsic hydrophilicity of the polygalacturonic acid chains, also render the network capable of holding a large amount of water. Upon dehydration, the interchain distance decreases, favoring polymer-polymer electrostatic interactions, rather than water-polymer interactions promoting the formation of junction zones among neighboring chains (Fig. 3.1(c)). As a result, dehydrated pectin films present a very brittle mechanical behavior, prone to tearing and cracking under tension. E-skins and wearable electronic devices must be flexible and stretchable to accommodate articulated motion and external solicitations. Stretchability can be achieved either by fabricating a specific substrate, which can accommodate the external stress [21], or by producing sensing layers that are intrinsically stretchable [22, 23]. Intrinsic stretchability is preferred because it avoids cumbersome microfabrication approaches. The as-prepared pectin films [13] are nonstretchable, but they can be modified chemically to create films with improved mechanical properties. Plasticizers are often used to produce pectin films for better handling and workability in the food industry [18, 24]. Understanding the impact of plasticizers on the mechanical and sensing properties of pectin films is essential for translating this new class of organic materials into e-skin applications. Plasticizers are nonvolatile and high-boiling point liquids, with low molecular weights [25]. Glycerol, for example, is a simple alcohol compound with three hydroxyl groups (polyol) and is one of the most commonly used plasticizers in food and pharmaceutical industries. Due to its low molecular size, glycerol can occupy intermolecular space between pectin chains, impairing hydrogen bonding, reducing polymer-polymer interactions, and thus increasing chain mobility. Glycerol can interact with the network in multiple

ways: for instance, the hydroxyl groups on glycerol can form covalent ester linkages either via hydroxyl-hydroxyl or hydroxyl-carbonyl condensation reactions [26] (Fig. 3.1(d)). The polar sites on the pectin chain could also be solvated by glycerol molecules. This polar interaction screens hydrophilic sites along the pectin chains, reducing intermolecular attraction. The resulting films (Fig. 3.1(e)) are expected to be less brittle and show a decrease in electrical resistance, due to the action of the plasticizer in increasing the ion mobility and the polymer segmental motion.

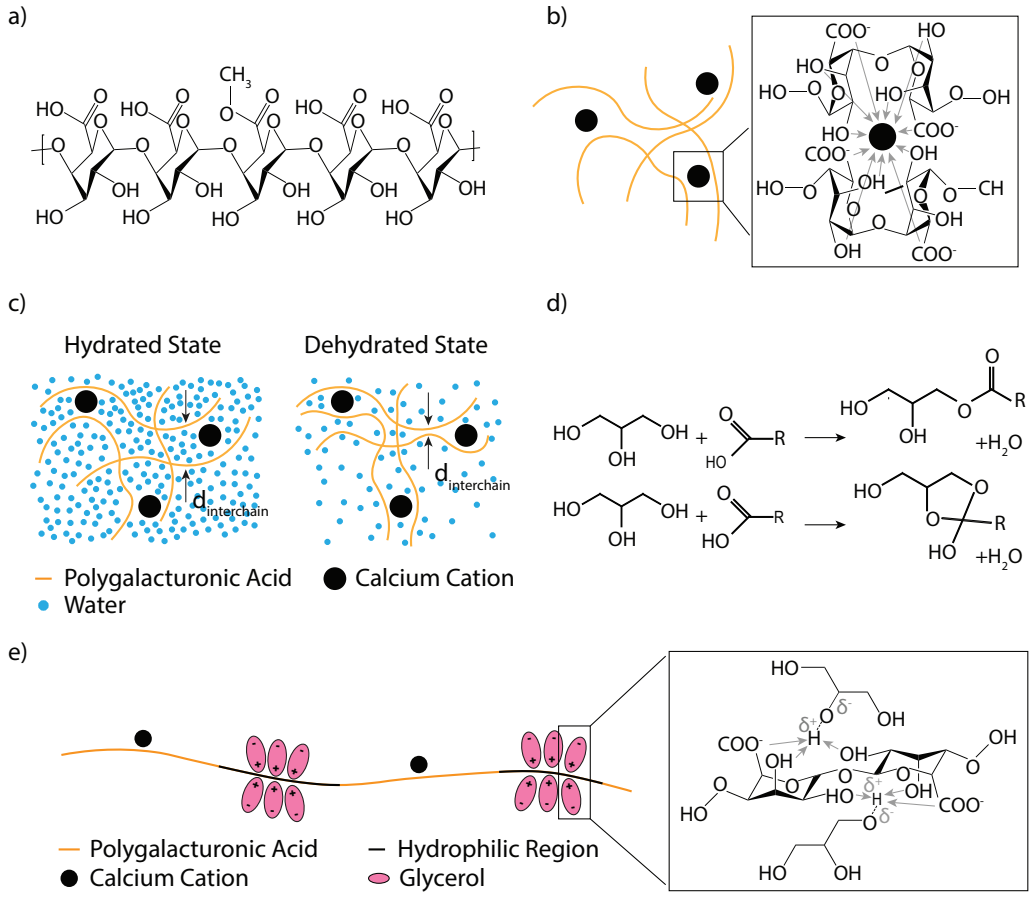

Figure 3.1: Pectin-Glycerol interaction. (a) Polygalacturonic acid chemical composition. (b) Low methoxylated pectin (orange lines) crosslinking mechanism with divalent calcium ions (black dots). The zoomed-in image shows divalent calcium ions coordinated by two polygalacturonic chains. The arrows indicate the electrostatic interaction between the groups on the side of the chains and the metal ion. (c) Pectin interchain distance in the case of high and low hydration. (d) Hydroxyl-hydroxyl and hydroxyl-carbonyl condensation reactions. (e) Electrostatic interaction of hydrophobic glycerol molecules (pink) with the hydrophilic regions (black lines) of the pectin network (orange line). The zoomed-in image shows one of the possible configurations of the electrostatic interaction between the hydrophilic region of the pectin backbone and the polar sites of the hydroxyl groups in the glycerol molecule.

In this work, we characterize the changes in the mechanical and electrical properties

of pectin films with different amounts of glycerol, using quasi/static tensile tests and electrical impedance spectroscopy. We also show that glycerol's beneficial effects on the mechanical properties of the films are contrasted by a reduced responsivity to temperature. Using thermogravimetric analysis (TGA) and water uptake measurements, we observe increased water retention associated with the presence of glycerol. We attribute the reduction in temperature responsivity to water excess in the polymer network. These results highlight how pectin-based films require a low water content to present high responsivity to temperature.

3.4 Materials and Methods

Films Preparation

Pectin films were produced using commercially available citrus low-methoxylated pectin with an 84% content of galacturonic acid and a 34% degree of methylation (Herbstreith Fox). Pectin molecular weight was 59000 Dalton, as measured by viscosimetry. Pectin powder (2%, w/v) was dissolved at 80°C in deionized water and stirred at 1400 rpm until a uniform solution was obtained. Glycerol was mixed with a 32 mM $CaCl_2$ crosslinking solution, obtaining solutions at 2.5%, 5%, 7.5% and 10% v/v glycerol content, respectively, in addition to a solution with only $CaCl_2$ used as control. The pectin solution previously prepared was casted into a mold, then to induce gelation the $CaCl_2$/glycerol solution was added. We let pectin in the crosslinking solution overnight (~12 hours) to allow the whole film to gel. After gelation, we let the films dehydrate overnight at room temperature. Higher glycerol concentrations resulted in phase separation between glycerol and the pectin films.

Mechanical Testing

To characterize the mechanical properties of pectin films and estimate the influence of glycerol on the films' response, we performed tensile tests. We produced rectangular samples (6 cm × 1 cm) with different glycerol contents. Samples were tested with an Instron E3000 tensile testing machine using a 250 N load cell. The tests were performed at 0.1 %/s up to samples' fracture. From the obtained stress-strain curves, we extracted the tensile strength, the elongation at break and the Young's modulus of the materials.

Water Uptake

We produced five different square samples (area: 1 cm^2) for each glycerol concentration. The pectin films were further dehydrated for 6 hours in an oven and then

their thicknesses were measured with a digital caliber. The dehydrated films were weighted using a digital scale (Mettler Toledo XPE Analytical Balance), and then immersed in DI water overnight. After the hydration process, water excess was removed with filtered paper. The water uptake w_{uptake} was calculated according to the relation:

$$w_{uptake} = \frac{w_t - w_0}{w_0}. \tag{3.1}$$

Electrical Conductivity

Electrical conductivity of the pectin films was measured via impedance spectroscopy. The films were clamped between two carbon blocking electrodes (area 1 cm^2) (Fig. 3.2(a)) and the film impedance was measured with a Zurich Instruments MFIA Impedance Analyzer. 1000 points were acquired in a frequency range of 1 Hz to 5 MHz. The bulk resistance R_b was calculated considering the intercept of the Nyquist plot with the real axis (Fig. 3.2(b)). The bulk conductivity σ_b was calculated according to the relation:

$$\sigma_b = \frac{d}{R_b A}. \tag{3.2}$$

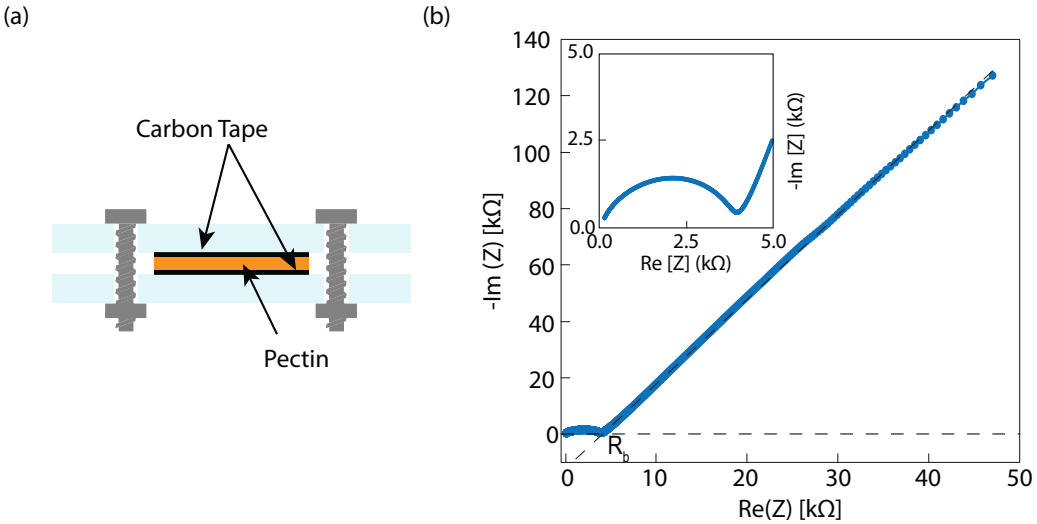

Figure 3.2: Measurement of pectin samples conductivity. (a) Set up for the measurement of the electrical conductivity of the pectin samples. A pectin film (orange) was sandwiched between two carbon electrodes (black) and then placed in a holder to apply spring compression. (b) Nyquist plot of a pectin sample with 5% glycerol content. The bulk resistance was calculated by calculating the intersection between the real axis and the interpolation of the linear region of the impedance plot. The top inset shows a zoomed-in portion of the plot, where the semicircle can be more clearly seen.

Thermal Responsivity

Temperature cycles on the films were actuated by a Peltier-Element (model Qc-31-1.4-8.5m). The temperature was independently measured with a Pt100 platinum resistance thermometer, which was previously calibrated with a FLIR thermal camera (model A655sc). A PI controller was implemented to control temperature between 20 and 60 °C. The samples were electrically connected via carbon tape and the current measured with a 2-channels source meter (Keithley 2636B), with a sampling rate of 10 S/s. The response after each thermal cycle was calculated as the ratio between the current measured at 60 °C and at 20 °C (Fig. 3.3(a)). The final response was calculated as the average of the stable responses over at least 100 thermal cycles (Fig. 3.3(b)).

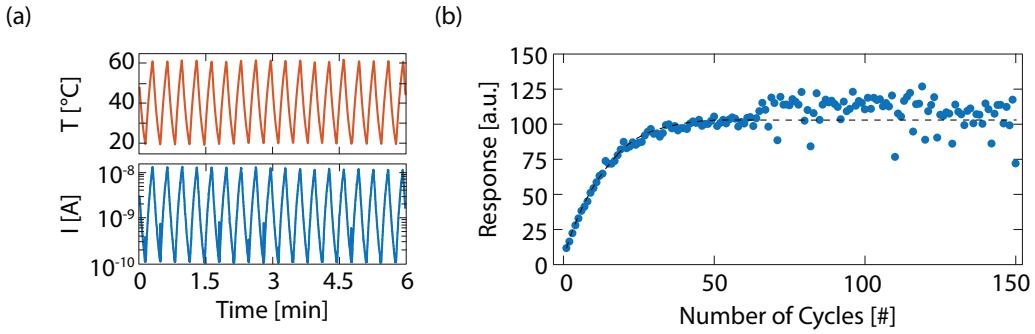

Figure 3.3: Electrical characterization of pectin membranes. (a) Typical thermal cycle: thermal cycle (top left), measured current (bottom left) and (b) typical response extrapolation.

Thermogravimetric Analysis

Pectin precursor solution was casted into aluminum pans and then the immersed in the crosslinking solution for 12 hours. The so prepared samples were then analyzed with a TG Analyzer (TA 550). The temperature was raised up to 100 °C at a rate of 0.1 °C/min with a controlled atmosphere of nitrogen (flow rate 20 mL/min) and the mass fraction loss was measured. The first and second derivatives with respect to time were calculated from the raw data of the percentage weight loss. A moving average with 10,000 points was applied to both the first and second derivative datasets to reduce noise. The total water mass after dehydration were calculated by looking at the intersection of the peaks in the second derivative with the temperature profile and mass fraction loss, respectively.

3.5 Results

Spectroscopy

To probe the formation of the network via the reaction between glycerol and pectin, pectin membranes were prepared in water and then crosslinked into a $CaCl_2$ solution with glycerol or without glycerol. Solid State Nuclear Magnetic Resonance (SS-NMR) spectroscopy in deuterium oxide did not show significant differences between samples with and without glycerol (Fig. 3.4(a)). Most likely, pectin chain immobility leads to a broadening and overlapping of the peaks so that useful information could not be extracted. FT-IR was performed on pure glycerol, pectin crosslinked without glycerol, and pectin crosslinked with 5% and 10% glycerol (Fig. 3.4(b)). The inset shows the formation of ester linkage indicated by a new stretching peak due to C-O-C appearing at 1047 cm^{-1}. Furthermore, vibration peaks of C-C bonding at 925 cm^{-1} and 850 cm^{-1} are diminished after the formation of the pectin-glycerol network. Although the esterification of glycerol with the carboxylic groups is slow without the presence of a catalyst, the FT-IR spectra variation indicates that hydroxyl groups of glycerol and pectin react to form ester linkage via ester formation reactions. The traces of this esterification can be explained as esterification catalyzed by acids (Fischer esterification) [26].

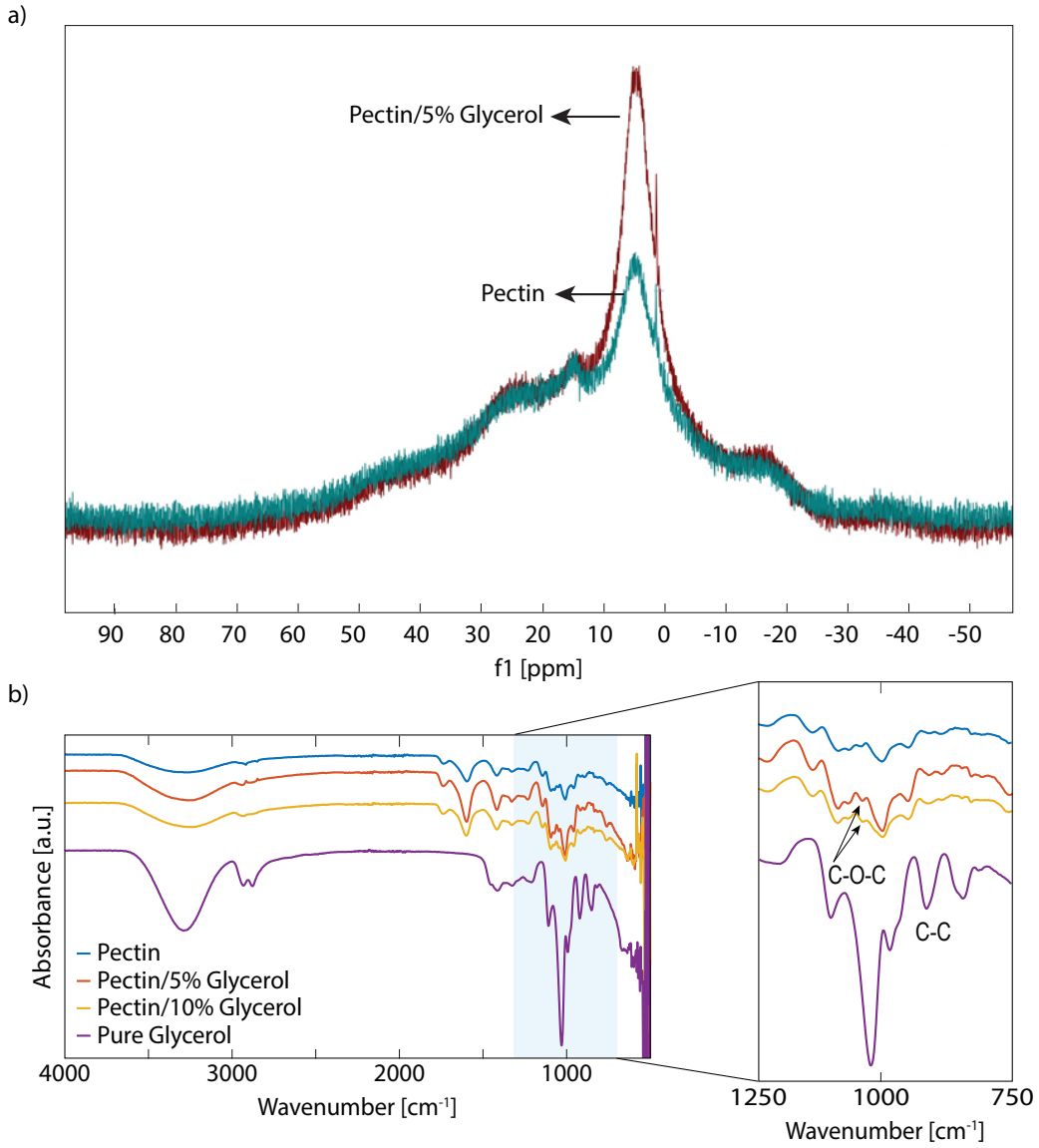

Figure 3.4: Spectroscopy on pectin. (a) Superimposed spectra of pectin membranes with 5% Glycerol (purple) and pectin membranes without glycerol (green). Pectin membranes with 5% Glycerol show higher intensity at 5.2 ppm, despite being mostly at similar levels of intensities at other regions. The immobility of the pectin membrane structure results in the broadening of NMR signals. (b) Comparison between membranes fabricated with pectin only (blue) and membranes with the addition of 5% (red) and 10% (yellow) of glycerol, respectively. Inset: zoom in of the FTIR between 1250 and 750 cm^{-1}: the vibration of a new peak (C-O-C linkage, 1047 cm^{-1}) due to the interaction between glycerol and pectin can be observed as well as the suppression of the C-C vibration at 925 cm^{-1} and 850 cm^{-1}.

Mechanical Properties

To further investigate the impact of the plasticizer on the crosslinked pectin network, we performed tensile tests on samples with and without glycerol. The mechanical

properties of the pectin films vary with the water content and polymer segmental motion, both of which are affected by the addition of the plasticizer. We observe that the addition of glycerol to pectin films increases the elongation at break and flexibility, while reduces the tensile strength and Young's modulus (Fig. 3.5(a - c)). The elongation at break is improved up to 5% v/v of glycerol content (Fig. 3.5(a)). Tensile Strength and Young's Modulus, however, decrease with the increasing plasticizer concentration (Fig. 3.5(b,c)). This behavior is closely related to the interactions between neighboring pectin chains and glycerol. Glycerol is a low molecular weight molecule, which can occupy the free volume space between the polymer chains, weakening the electrostatic attraction and increasing the segmental motion. Glycerol reduces the magnitude of these forces, weakening the electrostatic attractions and increasing the interchain distance between the hydrophilic regions of the pectin backbone. In this context, the few glycerol molecules esterified on the polymer backbone do not play a significant role in the mobility of the polymer chains. The improved segmental motion of the network is further confirmed by the amount of water retained in the hydrogel. The water uptake of the films increases with respect to the glycerol content in the film (Fig. 3.5(d)). However, the augmented hydrophilic character of the pectin network cannot be explained solely by the intrinsic hydrophilicity of the glycerol molecules and by the increased flexibility of the polymer chains. In fact, increasing the glycerol content over 5% v/v does not significantly change the amount of water absorbed by the network. To fully understand the hydrophilic character of pectin with glycerol, one has to take into account the availability of hydrophilic regions along the backbone. In the dehydrated state and without glycerol, hydrophilic regions aggregate, forming hydrogen bonds and reducing the amount of bound water. With the addition of glycerol, these hydrophilic sites become available and a higher concentration of water molecules bonds to these regions, increasing the water content within the network (Fig. 3.5(e)).

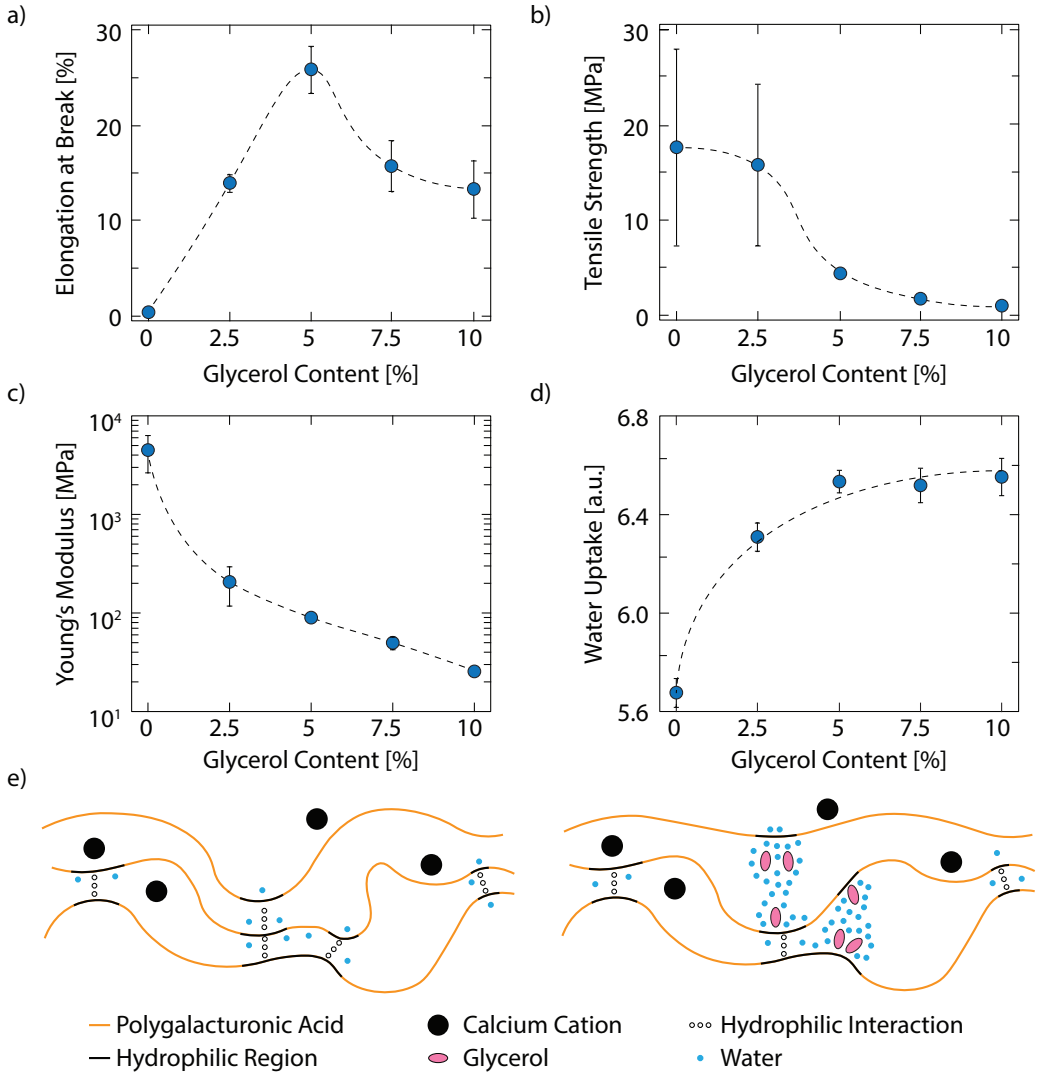

Figure 3.5: Pectin-Glycerol mechanical properties. (a) Elongation at break (for the point at a glycerol content of 0%, the error bar is smaller than the data marker), (b) tensile strength (for the points at glycerol contents of 5%, 7.5%, and 10%, the error bars are smaller than the data marker), and (c) Young's Modulus of the pectin based films as a function of glycerol content strength (for the points at glycerol contents of 5% and 10%, the error bars are smaller than the data marker). (d) Water uptake as a function of glycerol content. (e) Schematic diagram of the pectin interchain interactions, with (bottom) and without (top) glycerol. Orange lines represent the pectin chains crosslinked by calcium ions (black dots). Without glycerol, the hydrophilic regions tend to form hydrogen bonds (empty black dots). Glycerol molecules (pink ellipses) are attracted by the hydrophilic regions of the pectin backbone (black lines). As a result, they weaken the electrostatic attraction between the chains, increasing the segmental motion and the water absorption.

Electrical Properties and Temperature Response

The increased water content is also reflected in the electrical properties of the produced films. The films' conductivity increases with respect to the glycerol content

(Fig. 3.6(a)). In general, plasticizers can influence the conductivity of a polyelectrolyte in different ways, for example, by varying the water uptake amount, viscosity, dielectric constant, polymer-polymer interactions, and polymer-ion interactions [27–30]. The effects of plasticizers on the ionic conduction have already been studied in many plasticizer-polyelectrolyte systems [31–36]. Nevertheless, studies on the impact of plasticizers on the conductivity change with temperature have been limited [37]. In addition, none of these studies reported the temperature responsivity measured for pectin films. In earlier experimental studies [20], it was found that the temperature responsivity of pectin-based temperature sensors is strongly linked to the water content. However, the detailed transport phenomena of pectin hydrogels are not fully understood. We schematically depict the conduction in the films with a network composed of two parallel resistors, one representing the resistance of pectin and the other that of water, both of which change with temperature (Fig. 3.6(b)). Water resistance can be on the order of tens of kiloohms and decreases only slightly with temperature, because of changes in pH and viscosity. The other resistor describes the role played by calcium ions (Ca^{2+}) in pectin, and it is on the order of hundreds of megaohms at room temperature. It has been suggested that the thermal generation of free ions, or their increased mobility, is responsible for the large changes in resistivity with temperature recorded in pectin films [15, 20]. However, an optimal hydration status is required to observe this response. The high water content in the hydrogel network could hinder the measured temperature response since the high conductivity of water, which has a low temperature response, can suppress the effect of the Ca^{2+} ions (Fig. 3.6(b, top)). When the pectin film is dehydrated, the water resistance increases and the transport is mainly mediated by the pectin chains (Fig. 3.6(b, bottom)). As the sample undergoes thermal cycling, the unbound water evaporates, allowing the ionic conduction to dominate the current transport (Fig. 3.3(b)). The temperature response increases with respect to the number of thermal cycles, up to a limited value (Fig. 3.6(c)). This plateau indicates that all the unbound water molecules have left the network. As a result, the temperature response remains stable and the water molecules bound to the polymer backbones mediate the ionic conduction. The glycerol concentration in the pectin films increases the amount of water retained within the network, leading to a drop in the temperature response of the films (Fig. 3.6(d)). The glycerol concentration around 2.5% v/v halves the response, while concentrations above 5% v/v critically affect the temperature responsivity of the produced films.

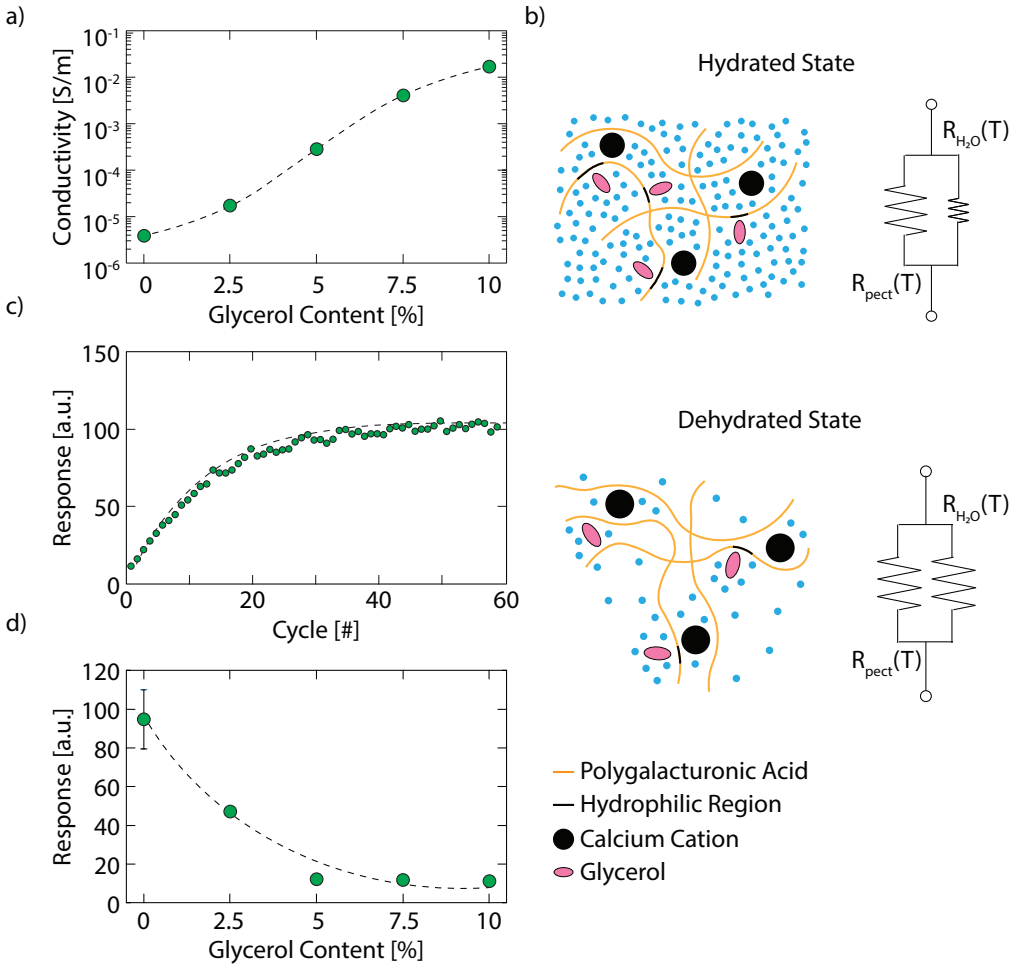

Figure 3.6: Effect of water on conductivity and temperature response of pectin. (a) Pectin network conductivity as a function of glycerol content. (b) Schematic of the electrical network of pectin films in the hydrated (top) and dehydrated (bottom) form. The smaller, light blue dots represent the water molecules, the larger, black dots represent the calcium ions, the orange lines represent the polymer chains, and black lines in the polymer chains represent glycerol molecules linked to polymer chains. (c) Typical cyclical temperature response of a pectin film. Every point represents the temperature response of the film (current value measured at 60 °C normalized by the current measured at 20 °C) after cycling it between 20 and 60 °C. The current in a pectin film increases 100 times when temperature changes by 40 °C. (d) Temperature responsivity of the pectin films as a function of glycerol content (for the points at glycerol contents of 2.5%, 5%, 7.5%, and 10%, the error bars are smaller than the data marker).

Thermogravimetric Analysis

To analyze how the water content in the films varies with temperature, at different glycerol concentrations, we performed TGA. Figure 3.7(a, top) shows the typical TGA profile of a pectin sample with glycerol as a function of time and temperature. As temperature increases, pectin samples start rapidly to lose weight due to water

evaporation. After ca. 200 min at around 42 °C, the first inflection point appears and the weight loss slows down, reaching a plateau. This turning point in the weight loss profile highlights a change in the kinetics of water evaporation. The inflection point shows that two types of water exist in the pectin network: free water and bound water. The first derivative of thermogravimetry (1st DTG) is useful in deconvoluting the different contributions in the weight loss fraction of the pectin samples. Figure 3.7(a,middle) shows the 1st DTG calculated from the weight loss profile. It clearly shows a jump, indicating a change in the kinetics from free and loosely bound water to relatively strong bound water against evaporation. Classical 1st DTG methods look at the intersection of the tangents before and after the inflection point in order to measure the amount of water molecules in the free or bound states [38–40]. However, these methods do not have high accuracy, because a small shift in the intersection point leads to a significant change in the calculated weight loss. It has been recently reported that the second derivative of thermogravimetry (2nd DTG) can achieve greater accuracy, repeatability, and reproducibility of water measurements [41]. In fact, the turning point in the weight loss appears as a peak in the 2nd DTG, which can be measured with greater accuracy than the intersection of tangents. Figure 3.7(a,bottom) shows the 2nd DTG calculated from the 1st DTG of a pectin sample. A peak, marking the change in the kinetics, is noticeable. The weight measured in the occurrence of this peak represents the amount of bound water within the network. The total amount of water retained in the network at the end of the evaporation processes increases as the glycerol content increases in the network, as clearly shown in Figure 3.7d. This result indicates that water is not retained directly in the network because of the glycerol water interaction and because more hydrophilic regions are available in the backbone to bound water. With the addition of glycerol, the water-polymer interactions prevail and a larger amount of water molecules are electrostatically bound to the polymer network.

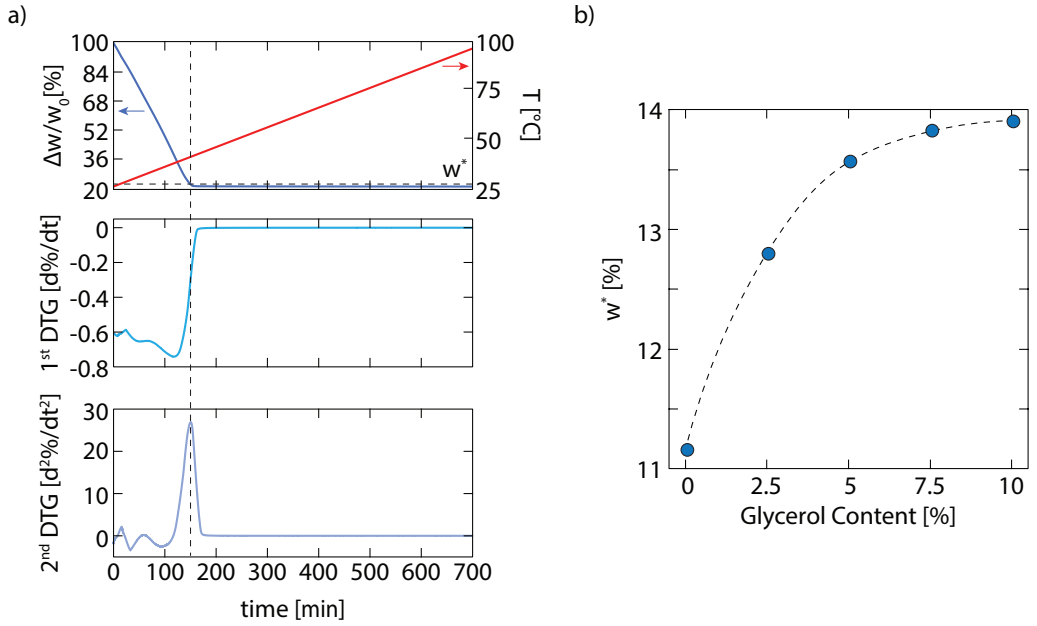

Figure 3.7: Thermogravimetric analysis on pectin. (a) Weight fraction loss as a function of time of a pectin sample (blue line) when the sample undergoes thermal ramping from room temperature to 100 °C (top). 1st DTG with respect to time calculated from the weight fraction loss (middle). 2nd DTG with respect to time calculated from the 1st (bottom). (b) Total percentage of weight retained after the evaporation of all free water. This percentage was calculated from the intersection of the second peak of the 2nd and the weight loss.

3.6 Conclusion

We investigated and characterized the effect of glycerol as a plasticizing agent in pectin-based films used for temperature sensing. We produced films with different glycerol concentrations and studied their effect on the mechanical, electrical, and temperature-sensing properties of the films. We show that glycerol improves elongation at the break of pectin films up to a critical concentration, but it suppresses their responsivity to temperature. We explain this behavior with the increasing water content in the films due to the presence of glycerol. The combination of the different studies presented elucidates that a concentration around 2.5% v/v of glycerol is the most desirable ratio to improve the mechanical properties of the material without critical losses of the temperature sensing capability. This research was funded by the Samsung Electronic GRO Program.

References

[1] S. Bauer. Sophisticated skin. *Nature Materials*, 12:871–872, 2013.

[2] X. Wang, L. Dong, H. Zhang, R. Yu, C. Pan, and Z. L. Wang. Recent progress in electronic skin. *Advanced Science*, 2(10):1500169.

[3] A. Chortos, J. Liu, and Z. Bao. Pursuing prosthetic electronic skin. *Nature Naterials*, 15:937–950, 2016.

[4] T. Q. Trung and N. Lee. Flexible and stretchable physical sensor integrated platforms for wearable human-activity monitoring and personal healthcare. *Advanced Materials*, 28(22):4338–4372, 2016.

[5] J.K. Aggarwal and Y.F. Wang. Sensor data fusion in robotic systems. In *Advances in Robotic Systems, Part 1 of 2*, volume 39 of *Control and Dynamic Systems*, pages 435–462. Academic Press, 1991.

[6] C. G. Núñez, W. T. Navaraj, E. O. Polat, and R. Dahiya. Energy-autonomous, flexible, and transparent tactile skin. *Advanced Functional Materials*, 27(18): 1606287, 2017.

[7] J. Kim, M. Lee, H. J. Shim, R. Ghaffari, H. R. Cho, D. Son, Y. H. Jung, M. Soh, C. Choi, S. Jung, K. Chu, D. Jeon, S.-T. Lee, J. H. Kim, S. H. Choi, T. Hyeon, and D.-H. Kim. Stretchable silicon nanoribbon electronics for skin prosthesis. *Nature Communications*, 5(5747), 2014.

[8] T. Q. Trung, S. Ramasundaram, B. Hwang, and N. Lee. An all-elastomeric transparent and stretchable temperature sensor for body-attachable wearable electronics. *Advanced Materials*, 28(3):502–509, 2016.

[9] M. Segev-Bar, A. Landman, M. Nir-Shapira, G. Shuster, and H. Haick. Tunable touch sensor and combined sensing platform: Toward nanoparticle-based electronic skin. *ACS Applied Materials & Interfaces*, 5(12):5531–5541, 2013.

[10] J. Park, M. Kim, Y. Lee, H. S. Lee, and H. Ko. Fingertip skin-inspired microstructured ferroelectric skins discriminate static/dynamic pressure and temperature stimuli. *Science Advances*, 1(9):e1500661, 2015.

[11] B. P. Mason, M. Whittaker, J. Hemmer, S. Arora, A. Harper, S. Alnemrat, A. McEachen, S. Helmy, J. Read de Alaniz, and J. P. Hooper. A temperature-mapping molecular sensor for polyurethane-based elastomers. *Applied Physics Letters*, 108(4):041906, 2016.

[12] C. Yu, Z. Wang, H. Yu, and H. Jiang. A stretchable temperature sensor based on elastically buckled thin film devices on elastomeric substrates. *Applied Physics Letters*, 95(14):141912, 2009.

[13] T. Yokota, Y. Inoue, Y. Terakawa, J. Reeder, M. Kaltenbrunner, T. Ware, K. Yang, K. Mabuchi, T. Murakawa, M. Sekino, W. Voit, T. Sekitani, and T. Someya. Ultraflexible, large-area, physiological temperature sensors for multipoint measurements. *Proceedings of the National Academy of Sciences*, 112(47):14533–14538, 2015.

[14] J. Jeon, H. Lee, and Z. Bao. Flexible wireless temperature sensors based on ni microparticle-filled binary polymer composites. *Advanced Materials*, 25(6): 850–855, 2013.

[15] R. Di Giacomo, L. Bonanomi, V. Costanza, B. Maresca, and C. Daraio. Biomimetic temperature-sensing layer for artificial skins. *Science Robotics*, 2 (3):eaai9251, 2017.

[16] W. Willays, L. McCartney, W. Mackie, and J.P. Knox. Pectin: Cell biology and prospects for functional analysis. *Plant Molecular Biology*, 47:9–27, 2001.

[17] W. Plazinski. Molecular basis of calcium binding by polyguluronate chains. revising the egg-box model. *Journal of Computational Chemistry*, 32(14): 2988–2995, 2011.

[18] P. Espitia, W. Du, R. Avena-Bustillos, N. Soares, and T. H. McHugh. Edible films from pectin: Physical-mechanical and antimicrobial properties - A review. *Food Hydrocolloids*, 35:287–296, 2014.

[19] S. Cardoso, M. Coimbra, and J.A. Lopes da Silva. Temperature dependence of the formation and melting of pectin–ca2+ networks: A rheological study. *Food Hydrocolloids*, 17(6):801–807, 2003. 6th International Hydrocolloids Conference - Part 2.

[20] R. Di Giacomo, C. Daraio, and B. Maresca. Plant nanobionic materials with a giant temperature response mediated by pectin-ca²⁺. *Proceedings of the National Academy of Sciences*, 112(15):4541–4545, 2015.

[21] G. Cantarella, V. Costanza, A. Ferrero, R. Hopf, C. Vogt, M. Varga, . Petti, N. Münzenrieder, L. Büthe, G. Salvatore, A. Claville, L. Bonanomi, A. Daus, S. Knobelspies, C. Daraio, and G. Tröster. Design of engineered elastomeric substrate for stretchable active devices and sensors. *Advanced Functional Materials*, 28(30):1705132, 2018.

[22] J. Sun, C. Keplinger, G. M. Whitesides, and Z. Suo. Ionic skin. *Advanced Materials*, 26(45):7608–7614, 2014.

[23] C. Keplinger, J. Sun, C. Foo, P. Rothemund, G. Whitesides, and Z. Suo. Stretchable, transparent, ionic conductors. *Science*, 341(6149):984–987, 2013.

[24] M. Aider. Chitosan application for active bio-based films production and potential in the food industry: Review. *LWT - Food Science and Technology*, 43(6):837–842, 2010.

[25] M. Vieira, M. da Silva, L. dos Santos, and M. Beppu. Natural-based plasticizers and biopolymer films: A review. *European Polymer Journal*, 47(3):254–263, 2011.

[26] S.D. Pasini Cabello, E.A. Takara, J. Marchese, and N.A. Ochoa. Influence of plasticizers in pectin films: Microstructural changes. *Materials Chemistry and Physics*, 162:491–497, 2015.

[27] G.O. Machado, H.C.A. Ferreira, and A. Pawlicka. Influence of plasticizer contents on the properties of hec-based solid polymeric electrolytes. *Electrochimica Acta*, 50(19):3827–3831, 2005.

[28] R. Huq, G.C. Farrington, R. Koksbang, and P.E. Tonder. Influence of plasticizers on the electrochemical and chemical stability of a li+ polymer electrolyte. *Solid State Ionics*, 57(3):277–283, 1992.

[29] L.R.A.K. Bandara, M.A.K.L. Dissanayake, and B.-E. Mellander. Ionic conductivity of plasticized(peo)-licf3so3 electrolytes. *Electrochimica Acta*, 43 (10):1447–1451, 1998.

[30] S. Gao, X. L. Yan, J. Zhong, G. B. Xue, and B. Wang. Temperature dependence of conductivity enhancement induced by nanoceramic fillers in polymer electrolytes. *Applied Physics Letters*, 102(17):173903, 2013.

[31] X. Qian, N. Gu, Z. Cheng, X. Yang, E. Wang, and S. Dong. Plasticizer effect on the ionic conductivity of peo-based polymer electrolyte. *Materials Chemistry and Physics*, 74(1):98–103, 2002.

[32] C. Walker and M. Salomon. Improvement of ionic conductivity in plasticized PEO-based solid polymer electrolytes. *Journal of The Electrochemical Society*, 140(12):3409–3412, 1993.

[33] Y. Masuda, M. Seki, M. Nakayama, M. Wakihara, and H. Mita. Study on ionic conductivity of polymer electrolyte plasticized with peg–aluminate ester for rechargeable lithium ion battery. *Solid State Ionics*, 177(9):843–846, 2006.

[34] G.K. Prajapati, R. Roshan, and P.N. Gupta. Effect of plasticizer on ionic transport and dielectric properties of pva–h3po4 proton conducting polymeric electrolytes. *Journal of Physics and Chemistry of Solids*, 71(12):1717–1723, 2010.

[35] W. Ning, Z. Xingxiang, L. Haihui, and W. Jianping. N, n-dimethylacetamide/lithium chloride plasticized starch as solid biopolymer electrolytes. *Carbohydrate Polymers*, 77(3):607–611, 2009.

[36] P. K. Varshney and S. Gupta. Natural polymer-based electrolytes for electrochemical devices: A review. *Ionics*, 17(6):479–483, 2011.

[37] J. Andrade, E. Raphael, and A. Pawlicka. Plasticized pectin-based gel electrolytes. *Electrochimica Acta*, 54(26):6479–6483, 2009.

[38] D. Fessas and A. Schiraldi. Water properties in wheat flour dough I: classical thermogravimetry approach. *Food Chemistry*, 72(2):237–244, 2001.

[39] J. Saldo, E. Sendra, and B. Guamis. Changes in water binding in high-pressure treated cheese, measured by tga (thermogravimetrical analysis). *Innovative Food Science Emerging Technologies*, 3(3):203–207, 2002.

[40] A. Lodi and Y. Vodovotz. Physical properties and water state changes during storage in soy bread with and without almond. *Food Chemistry*, 110(3):554–561, 2008.

[41] Y. Wang, Q. Zheng, W. Li, Y. Ma, X. Zhao, and C. Zhang. Measurement of free water in foods by secondary derivative thermogravimetry. *CyTA - Journal of Food*, 16(1):438–443, 2018.

Chapter 4

ROLE OF PROTON CARRIERS IN THE TRANSPORT MECHANISM AND THERMAL PROPERTIES OF HEA–AA ION CONDUCTORS

4.1 Chapter Preamble

In Chapter 3, we showed that pectin films need to have a specific water content in order to show an optimal temperature sensitivity. Nevertheless, the complex chemical structure of pectin makes understanding the microscopic transport phenomena extremely difficult. In this chapter, we will use a simplified organic scaffold to study the effect of water concentration on the material's temperature sensitivity. Combining DSC, FTIR, and dielectric spectroscopy data, we will identifiy the exact role water plays in the conduction mechanisms and in the temperature responsivity. In addition, we will show that the temperature response recorded in this material is a direct consequence of the interaction between the functional groups present on the polymer's backbone and the coordinating central ion.

4.2 Abstract

The understanding of transport phenomena in ion conducting polyelectrolytes is crucial to enable the progress in important fields such as energy storage and conversion. A new class of bio and synthetic polyelectrolytes has attracted a lot of attention for their remarkable temperature response. Previous works have suggested that the mechanism responsible for this response lays in the interaction between the polyelectrolyte coordination complex and the crosslinking ions. Furthermore, the concentration of water in this systems has been indicated as crucial in order to record the record-breaking temperature response. Here, we analyze the role of the proton transport in anhydrous 2-hydroxyethyl acrylate–acrylic acid (HEA–AA). By combining gravimetric analysis, DSC, and FTIR data, we show how the increase in water content changes the ion mobility without affecting their number density. The Almond-West formalism as well as the continuous time random walk model are used to analyze different transport phenomena at different frequency and their dependence on water concentration. The application of the time humidity superposition principle shows that two conduction regimes are present: one at low humidity where the ions are the main charge carrier, and one at higher humidity where the

protons start contributing to the ion conduction. The bulk temperature response is directly affected by this transition, decreasing as a function of water concentration. Through the analysis of the Arrhenius plot at different water concentration and the application of the VTF model, we shows that this drop in response is caused by an increase in the chain mobility and a decrease in the pseudo activation energy for the ion hopping as water content increases.

4.3 Introduction

Ion conducting polyelectrolytes have the potential to replace liquid electrolytes in batteries [1, 2] and fuel cells [3–5]. Polyelectrolytes are macromolecular systems that can transport ions or protons, in which the monomeric unit bears an electrolyte group. The presence of these moieties allows polyelectrolytes to solvate ions without the need of a liquid solvent. Even if in theory many of these polyelectrolytes are solvent-free, because of their chemical structure they absorb water molecules. The hydration level of the polymer matrix strongly affects and modify the transport properties of the material. Although the role of hydration and proton conduction has been studied in theoretical and computational works [6–9] and despite the numerous experimental investigations [10–14], the underlying features of the conduction mechanism are still not very well understood. In particular, in these systems it is difficult to separate the role of proton conduction from the effect the water molecules have on the ion-polymer coordination complexes. Recently, the time humidity superposition principle (THSP) has been used to investigate the effect of water on the conductivity of polyelectrolytes complexes and polyelectrolytes multilayers [15–17]. The systematic study of conductivity spectra as a function of hydration in these systems allowed to conclude that the increase in water concentration results in a higher ion mobility without affecting the number density of conducting ions. Here, we applied this principle on 2-hydroxyethyl acrylate–acrylic acid (HEA–AA), a recent class of single ion conductor polyelectrolytes that has attracted a lot of attention for its temperature sensing properties [18].

HEA–AA is composed of highly polar 2-hydroxyethyl acrylate groups and weak acrylic acid groups, randomly distributed. These functional groups together have the ability to coordinate metal cations, forming a structure comparable to the egg box model reported in similar bio and synthetic polymers [19–21] (Fig. 4.1(a)). Starting from this simplified version, we investigated how the ion conduction is influenced by the concentration of water in the polymer matrix.

According to the general model of transport in an ion conducting medium, the conductivity is given as the sum of the individual contributions from every conducting species:

$$\sigma = \sum_i \sigma_i = \sum_i N_i \mu_i q_i \tag{4.1}$$

where N is the number density of the carriers, μ the mobility and q the charge of the $i-th$ conducting species. In the case of a single ionic conductor, the conductivity reduces to one term only. However, because the hydrophilic nature of the polymer, water molecules are also present in the matrix, both in a bound and unbound state, contributing to the overall conductivity. Considering both the proton and the ion conduction, the total conductivity in the polymer can be written as:

$$\sigma = N_{H^+} \mu_{H^+} q_{H^+} + N_{Ca^{2+}} \mu_{Ca^{2+}} q_{Ca^{2+}}. \tag{4.2}$$

Water molecules can affect the conductivity of the polyelectrolytes in multiple ways. Proton transport can take place by molecular diffusion of water molecule as an aggregate via the vehicular mechanisms. However, given the low water content in HEA–AA, the vehicular mechanism is not likely. Anhydrous proton transport occurs via the 'Grotthuss mechanism' in which protons move via molecular diffusion through the formation and sequent cleavage of hydrogen bonds [22]. The higher concentration of water molecules provides more protons available for conduction and therefore an increase in proton conductivity. The presence of water molecules in the polymer network does not only influence the polymer conductivity directly by increasing proton conductivity, but also by modifying the landscape in which the ions move. Water molecules, in fact, interact with the hydrophilic regions of the polymer backbone, screening the electrostatic attraction between the polymer chains. This screening effect plasticizes the polymer chains, resulting in an increase in the segmental motion of the backbone. The increase in the chains segmental motion facilitates the hopping of the ions from one site to another or offers additional pathways for the ions to move. As a result, interchain and intrachain hopping increases leading to an increase in the ion conductivity (Fig. 4.1(b)). Energetically, the effect of water with respect to the segmental motion is an overall reduction of the activation energy in the ion mobility μ. In addition to this effect, water can modify the way ions interact with their coordinating environment. The presence of water molecules compete with the coordination complexes on the polymer's backbone for binding the metal ions, lowering the activation energy for ion hopping. On the other hand, a larger solvation shell will decrease the ion mobility due to the increasing friction loss the moving ion encounters. Therefore, even though the hydration shell

radius depends on the water concentration, a significant effect is not expected due to the increasing friction forces that will impair ions mobility. Besides the increase in proton transport and the lowering of the barrier energy for ion transport, water concentration can affect macroscopically the conductivity in the polymer. In fact, the amount of water molecules in the matrix will change the strength of the electric field that individual ions will be subjected to, and therefore affect the dielectric constant of the polymer. Since the capacitance of the polymer is a description of the number of charges therein contained, and since the capacitance depends by the dielectric constant of the medium, an increase in water concentration will cause a change in the dielectric constant, resulting in a change in the number density of the conducting ions.

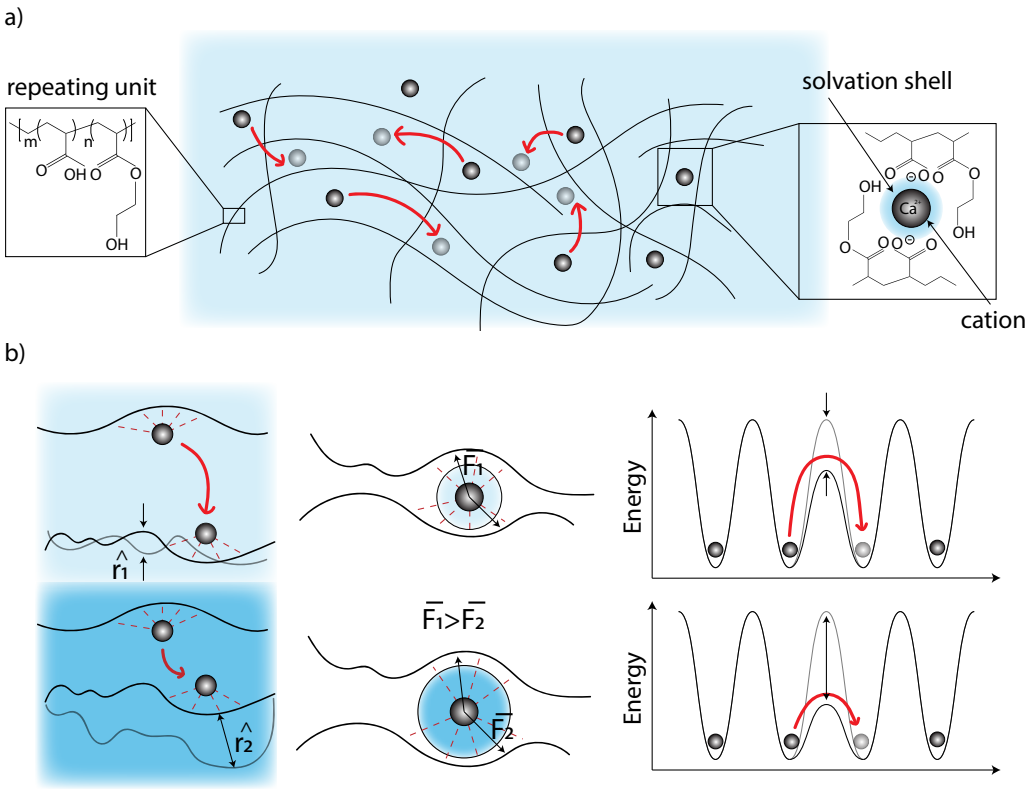

Figure 4.1: Schematic of conduction mechanisms in HEA–AA. (a) Crosslinking mechanism and ion transport in HEA–AA. Black lines represents the polymer backbone, grey circles the metal ions in the matrix, while the red arrows the potential paths for ion hopping. Left inset: chemical structure of HEA–AA. Right Inset: coordination complex. (b) Effect of water concentration on the ion environment and the coordination complex. Left: effect of water concentration on polymer segmental motion. Middle: effect of water concentration on coordination complex. Right: lowering of the energy barrier as a result of higher water concentration.

Considering the effect of the water content to the activation enthalpy U_N and U_μ and the dielectric constant ϵ, we can write the conductivity σ as proportional to [23]:

$$\sigma \propto N_{H^+}(RH)\mu_{H^+}q_{H^+} + N_0[exp(-\frac{U_N(RH)}{\epsilon(RH)k_BT})]\mu_0[exp(\frac{U_\mu(RH)}{k_BT})]q_{Ca^{2+}}. \quad (4.3)$$

Deconvoluting the individual contributions is often not trivial since multiple mechanisms superimpose resulting in a single measured quantity, the conductivity. In this work, we combined the results obtained by gravimetric and calorimetric analysis, FTIR, impedance spectroscopy and temperature response as a function of water content to analyse the importance of these different mechanisms and understand the role water molecules play within the polymer matrix.

4.4 Materials and Methods

HEA–AA Synthesis

Polymer films were prepared following the procedure reported in [18], employing reversible addition-fragmentation chain transfer (RAFT) polymerization as shown in figure. Unlike as reported in this previous works, we did not synthetize a block copolymer but we only used the 2-Hydroxyethyl acrylate and the tert-Butyl acrylate units for this work 4.2. Nitrogen purged tert-butyl acrylate 2 (1.28 g, 10 mM) and 2-hydroxyethyl acrylate 1 (1.16 g, 10 mM) is dissolved in 2 mL DMF, followed by S,S-Dibenzyl trithiocarbonate 3 (29 mg, 0.1 mM). The mixture is further purged under nitrogen for 3 minutes, added with AIBN (0.8 mg, 5 µM), and then stirred at 75 °C under protection of N_2, and the progress in polymerization was monitored using HNMR. The reaction was cooled down and vented to air at approximately 80% conversion rate. Residual tert-butyl acrylate and 2-hydroxyethyl acrylate was removed first by vacuum, followed by precipitation in 100 mL cold Diethyl Ether to yield a yellow oil as the macro-CTA (2.02 g, 80%). For deprotection, the polymer (1 g) was dissolved in 3 mL dichloromethane (DCM), followed by addition of 3 mL Trifluoroacetic acid (TFA). The reaction was stirred at room temperature overnight. DCM and TFA were removed by vacuum, followed by precipitation in cold Diethyl Ether, to result in a highly sticky yellow oil as HEA–AA (100%). We then mixed the deprotected HEAAA with a calcium chloride solution in ethanol 1:2 (300 mM) to obtain the final solution.

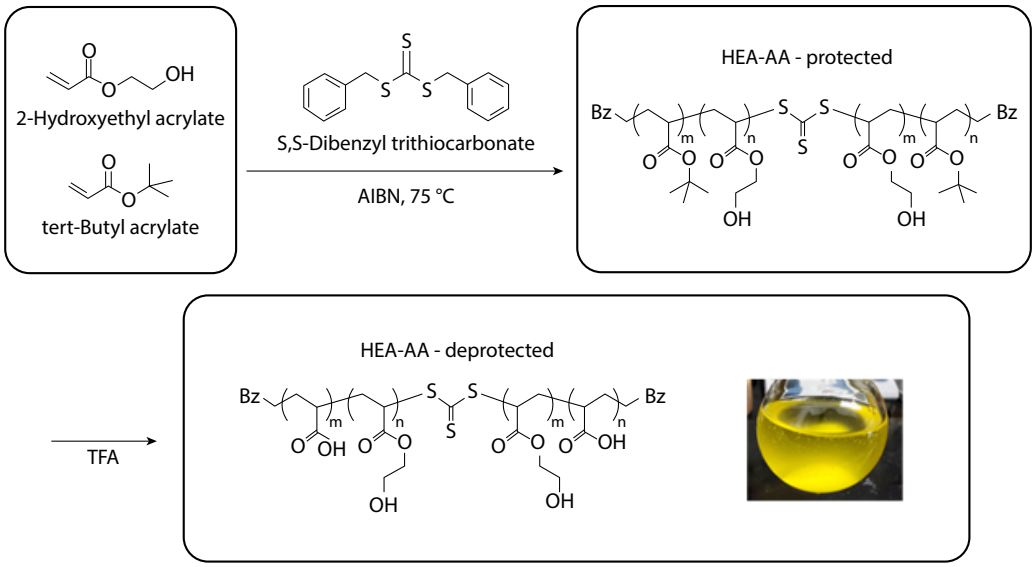

Figure 4.2: HEA–AA synthesis.

Differential Scanning Calorimetry (DSC)

Thermal measurements were conducted using Differential Scanning Calorimetry 250 from TA instruments. Nitrogen gas purging was set at 50ml/min flow rate. 40 µL HEAAA was deposited in a Tzero aluminium pan. After dehydration in a nitrogen box at room temperature over 24 hours, its weight was measured to be 3.3 mg. The temperature scanning was performed at 10 °C/min, cycling from -40 °C to 100 °C. During the measurement, the remaining water in the sample evaporates at high temperature. After the DSC scans, the weight of the sample decreased to 3.1 mg.

Gravimetric Measurement

Gravimetric measurements of the samples were performed via a precision quartz microbalance (openQCM Q-1, 5MHz). 500 nL of HEA–AA with a concentration of 1 g/mL was deposited on the active area of the quartz (6 mm radius) and dehydrated in a vacuum chamber for half an hour. The so prepared samples were kept overnight in a glove box flushed with nitrogen to eliminate excess ethanol and water from the polymer matrix. The resonance of the so prepared sample was then measured in the humidity box at different humidity.

FTIR

P3A with calcium was drop cast onto a piece of silicon wafer and dried at 70 °C on a hotplate for several days. The sample was then stored in a desiccator. Transmission Fourier transform infrared spectroscopy (FTIR) was acquired on a Nicolet 6700 FTIR purged with nitrogen. A blank spectrum was taken on silicon wafer at several intervals over a 25 minute period to observe the removal of gases introduced during the sample placement. The spectrum taken at 25 minutes was used as the reference for calculating absorption of the sample. FTIR of the dried sample was then taken at several intervals over a 20 minute period. The spectrum taken at 20 minutes was used at the dried sample spectrum (Fig. 4.3(a)). The sample was then placed on an elevated platform in a sealed container with a small quantity of water, for 15 minutes. The sample was removed from the humidity chamber and FTIR was then taken at several intervals over a 180 minute period. The FTIR data was fit utilizing a custom python script for the data from 1519.66-1897.64 cm^{-1}. It was fit with 8 gaussian peaks and a linear background (Fig. 4.3(b)). Peak locations and widths were identically constrained for all fits, constraints were set by visual inspection of the data. Peaks at ~1563 cm^{-1} and ~1597 cm^{-1} were assigned to the calcium bound carboxylic acid. The peak at ~1620-1630 cm^{-1} was assigned to water. The areas of the peaks were evaluated and plotted.

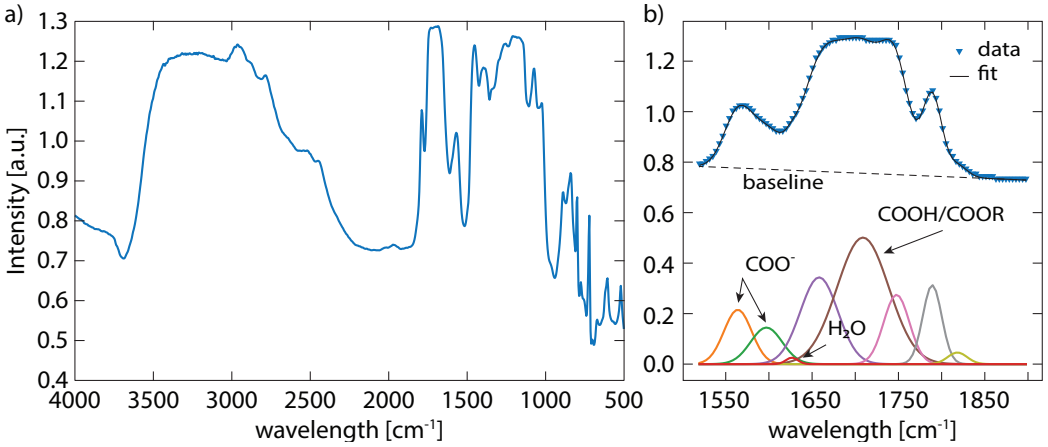

Figure 4.3: FTIR analysis. (a) Transmission FTIR specturm of HEA–AA after 20 min under N_2. (b) Peak identification and fitting of the FTIR region between 1500 and 1900 cm^{-1}.

Humidity Control

A custom humidity-controlled box was built to control humidity between 0% and 60%. A mix between air flow passing through desiccants beads was mixed with air

flow coming from a water tank. By adjusting the air speed and the ratio between the two flows the correct humidity could be achieved in the chamber. The humidity was then measured by a humidity sensor (Sensoria SHT16) placed in close proximity to the sample and used to keep the humidity constant in the chamber. A breakout board was placed into the humidity box in order to connect sample to the impedance analyzer. The computer was connected to the humidity controller, the temperature controller, and the impedance analyzer in order to control the set points and collect the humidity, temperature, and impedance data (Fig. 4.4(a)). The humidity value was stable over time, as shown in Figure 4.4(b) and the controller achieved a good accuracy (less ±0.3 %) for all the RH values used in this study (Fig. 4.4(c)).

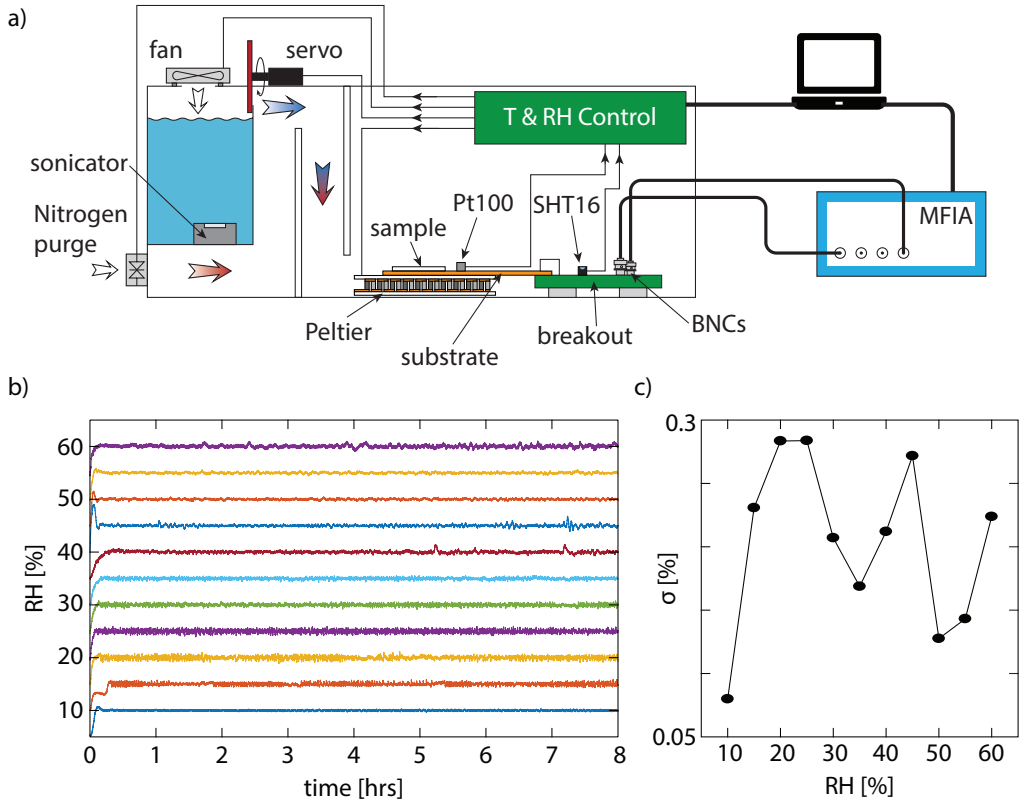

Figure 4.4: Humidity control. (a) Schematic of the custom made environmental controlled chamber to performed the humidity/temperature controlled experiments. (b) Recorded RH over time (8 hours) for various set points. (c) Measured standard deviation over the experiment time for various RH levels.

Impedance Spectrum

5 µL of HEAAA (1g/mL) were then deposited on polyimide substrates, prepatterned with gold electrodes and dried under vacuum for half an hour. The so prepared samples were kept overnight in a glove box flushed with nitrogen to eliminate ethanol/water excess from the polymer matrix. The impedance spectra were acquired by an impedance analyzer (Zurich Instrument, MFIA 5 MHz). The samples were kept at room temperature (40 °C) for the whole duration of the experiment. This temperature was chosen in order to obtain an appropriate water content for the tested humidity range. In addition, to ensure that the water content reached the equilibrium, we kept the samples at the specific humidity for 8 hours at 1Hz before starting the frequency sweep. After this time, we acquired the impedance spectra between 1 Hz and 5 MHz with different current ranges (i.e. 1 µA, 10 µA and 100 µA), to ensure the highest accuracy. The data sets were then merged. The humidity was increased from 5% to 50% in steps of 3%. It should be noted that the data shown in this work, are presented in form of conductance rather than its dimensionless counterpart conductivity, given the planar geometry at which the measurements were performed. This might sound uncommon practice, however, when looking at the same sample, the conductance will scale in the same way of the conductivity, therefore when calculating the slopes of group of points over frequency or measure temperature response, it will be independent of the geometry of the sample. We measured the impedance of the empty cell (comprising of the substrate, connectors and cables) and subtracted these values from the one of the full sample to eliminate parasitic effects arising from spurious capacitance (Fig. 4.5).

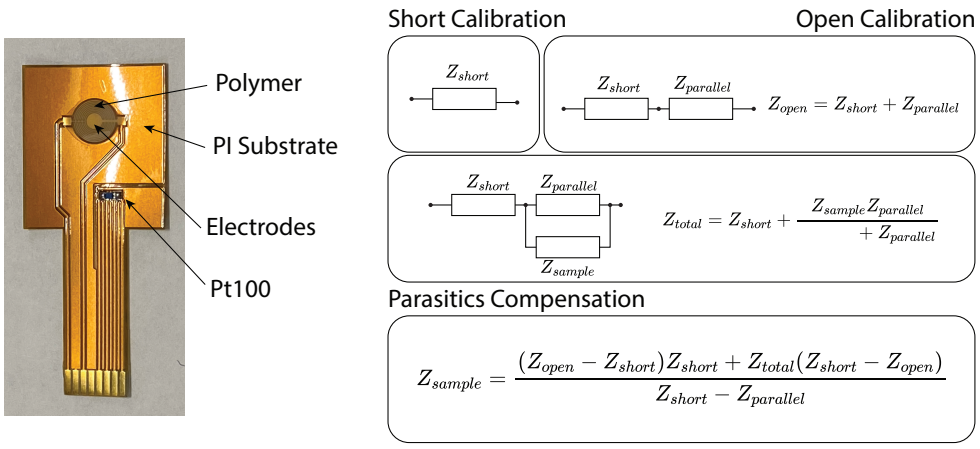

Figure 4.5: Parasitics compensation. (a) Image of the substrates used for the impedance spectroscopy measurements. (b) Parasitics compensation procedure.

Response Calculation

Temperature cycles on the films were actuated by a Peltier-Element (model Qc-31-1.4-8.5m). The temperature was independently measured with a Pt100 platinum resistance thermometer placed on the polyimide substrate near the polymer. The Pt100 sensors were previously calibrated with a FLIR thermal camera (A655SC). A PID controller was implemented to generate a sinusoidal temperature between 27 and 62 °C. The substrates and the reference Pt100 were electrically connected through an interface board that could be connected with the impedance analyzer and the temperature control board. The current was measured with the impedance analyzer with an average sampling rate of 10 S/s. The temperature response as a function of frequency was isochronically measured: the frequency was kept constant within one temperature cycles and then changed to the next frequency for the next cycle. The frequency was swept from 1 Hz to 500 kHz. To avoid the thermal hysteresis due to the sample mass, we considered only the raising section of the temperature response and sampled the current at different temperatures. The real part of the temperature response after each thermal cycle was calculated as the ratio between the conductance measured at 62 °C and 27 °C. The humidity was kept constant for 8 hours and then switched to the next value. Relative humidity was swept from 5% to 20% in steps of 3%.

Almond-West formalism and Continuous Time Random Walk model comparison

In order to verify the accuracy of the fitted data, we calculated the DC conductance and onset frequency using two different methods: the AW formalism and the CTRW model. For the AW formalism, the DC conductance G_{DC} was calculated from the intersection between the frequency corresponding to the maximum of the tangent loss and the conductance data. The onset frequency was then calculated as the frequency at which $G(\nu^*) = 2G_{DC}$ (Fig. 4.6(a)). Because of the limited frequency range, the spectra at humidity higher than 35% could not be fitted using this method because the portion of the spectrum where the line $2G_{DC}$ intercepts the conductance spectrum was outside of the measured frequency range. We also estimated the DC conductance G_{DC} and the onset frequency ν^* using the CTRW model modified with a Debye relaxation term. These two characteristic points were calculated directly from the fitting of the data to the CTRW model (Fig. 4.6(b)). The two onset frequencies slightly differ from each other (Fig. 4.6(c)).

Nonetheless the relationship between the DC conductivity and the onset frequencies calculated with the two different methods maintained the same shape (Figs. 4.6(d,e)).

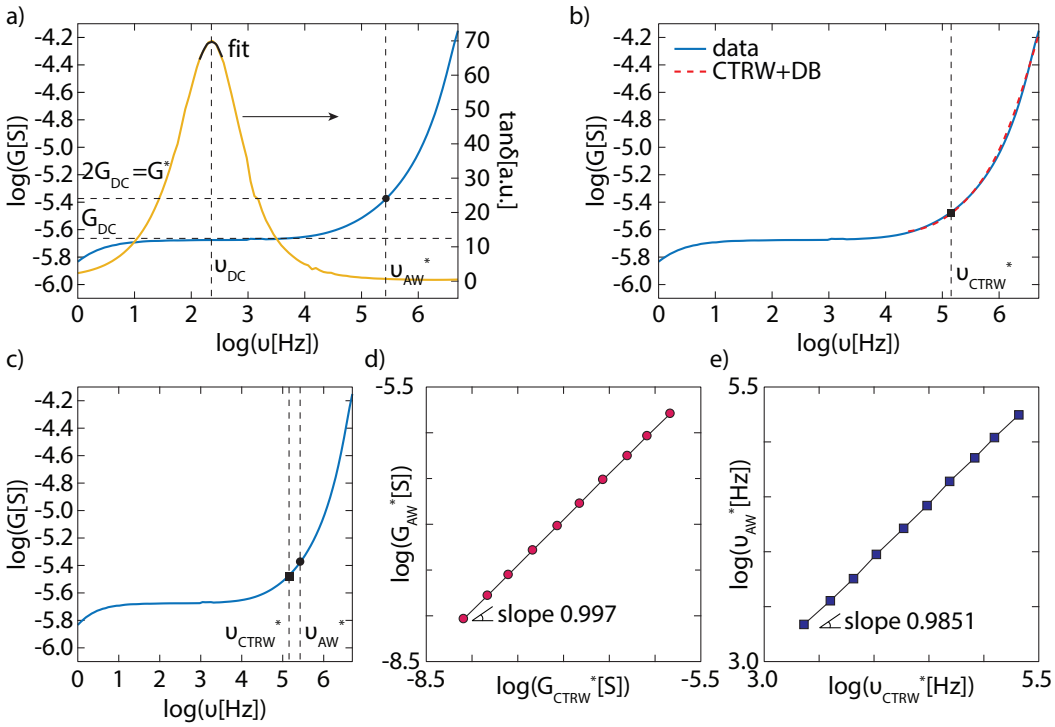

Figure 4.6: Comparison between the AW formalism and the CTRW model to calculate the onset frequency and DC conductivity. (a) AW formalism to calculate ν^* for a sample at RH 35%. The tangent loss $tan(\delta)$ was used to calculate σ_{DC}. (b) CTRW fitting and corresponding ν^* for the same sample. (c) Comparison between the onset frequency calculated with the AW formalism and the CTRW model. The two onset frequency ν^*_{AW} (circle) and ν^*_{CTRW} (square) are plotted on the correspective conductance plot. (d) Comparison between the DC conductivity $log(G^*)$ calculated with the two different methods for different humidity. (e) Comparison between the onset frequency $log(\nu^*)$ calculated with the two different methods for different humidity.

Data fitting

All the impedance data were corrected for the parasitic effect before the fitting using the method described above. Both the real and imaginary parts of the conductance data were used for the nonlinear regression (Fig. 4.7). We chose the mean squared logarithmic error (MSLE) as the loss function because the fitted conductance spans several orders of magnitude over the measured frequency range and MSLE is a better measure to minimize the percentage error of the fitting. Basin hopping minimization method was used to find the global minimum of the loss function. For the VTF fitting, we assume that $_0$ is constant for varying humidity. In fact, since $_0$ is the

conductance at the infinite temperature and is proportional to the concentration of all the possible current carriers in the system, it should not change with RH. The fitting of B, T_0 and $_0$ simultaneously for each RH results in multiple local fitting minimums. During the fitting we set $_0$ as the shared parameter for all RH.

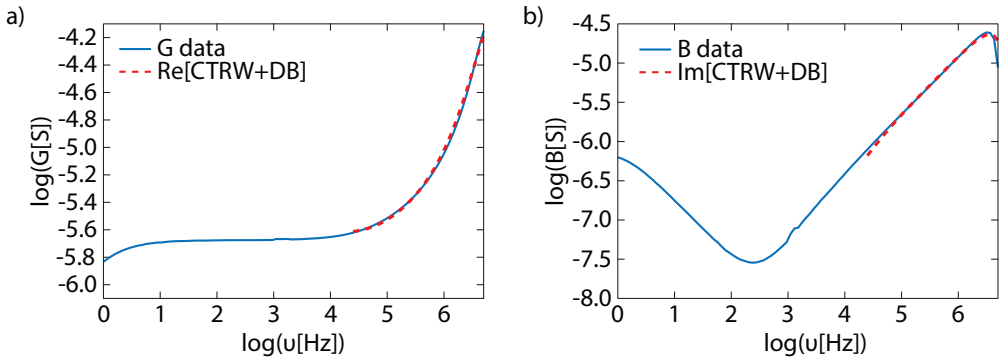

Figure 4.7: Complex fit method. Complex fit results when compared to the sample's (a) conductance and (b) susceptance measured at RH 35%.

Scaling

The conductance obtained at different humidity we scaled according to:

$$\frac{\sigma'(\nu)}{\sigma_{DC}} = F\left(\frac{\nu}{\sigma_{DC}\nu^*}\right) \tag{4.4}$$

where the DC conductance G_{DC} and the onset frequency ν^* were calculated through the modified CTRW model fitting procedure.

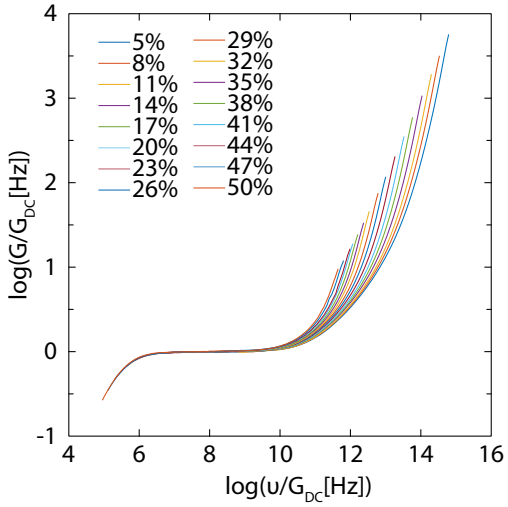

Figure 4.8: Superimposed spectra at different RH.

4.5 Results

Effect of Water on the Macroscopic Properties of HEA–AA

Varying the amount of water within the polymer matrix is usually obtained by exposing the sample to a saturated atmosphere at different relative humidity (RH). In this study, we employed multiple techniques to vary the RH of the environment. The dynamic of water absorption was evaluated gravimetrically through a precision quartz microbalance while the sample was exposed to humidity varying from 5% to 50%, while at room temperature. As shown in Figure 4.9a, the increase in the external RH results in the decrease of the resonance frequency of the quartz, indicating an increase in the resonating mass. In fact, due to the hydrophilic character of the matrix and the presence of hygroscopic metal calcium cations, the water molecules present in the environment are absorbed both by the polymer backbone and the solvated ions. Interestingly, also the dissipation factor of the resonating mass increases as a function of RH, suggesting an increase in polymer viscosity [24, 25]. This behavior is further confirmed by the analysis of the glass transition temperature of HEA–AA. Figure 4.9b shows the heat flow as a function of temperature as characterized by differential scanning calorimetry (DSC). A hydrated sample was place in the DSC and cycled between -50 and 100 $^{\circ}$ C under N_2 purge. Because of the temperature cycling and the dry atmosphere, at every cycle the sample loses water molecules (the cycling temperature is not high enough to induce polymer degradation). Therefore, at every cycle the water content is lower compared to the previous cycle. As expected, with decreasing water content, the glass transition temperature increases (Fig. 4.9(b, inset)). Water acts as plasticizer in hydrophilic polymers reducing the electrostatic interchain interactions. Fewer water molecules will favor stronger interchain interactions, leading to a lower glass transition temperature. In addition, lower water concentration favors stronger coordination interactions between the metal ions and the polymer chains, pushing the polymer to remain in a crystalline state for increasing temperatures. As previously described, the presence of water molecules could also screen the interaction of the cations inside the matrix and the polymer backbone. In order to evaluate this effect on the ions contained in the HEA–AA, we performed FTIR at different water content. Similarly to the procedure followed in the DSC experiment, we exposed a dried sample to a saturated environment and then performed FTIR at regular intervals under nitrogen purging to observe how the spectrum is modified. As time evolves, the area of the peak corresponding to water concentration decreases, confirming the sample is dehydrating. On the other hand, the area of the peaks

associated with bound Ca^{2+} ions (i.e., the concentration of deprotonated carboxylic acids) does not show any significant variation (Fig. 4.9(c)). This implies that the number density of calcium cations remains constant and is not significantly affected by the water concentration. The combined effect of improved segmental motion and lower binding energy between the ions and the coordination sites results in a strong dependence of the polymer's bulk conductance on water content. As a result, the bulk conductance increases exponentially with water content and shows a slope change for humidity above 35% (Fig. 4.9(d)).

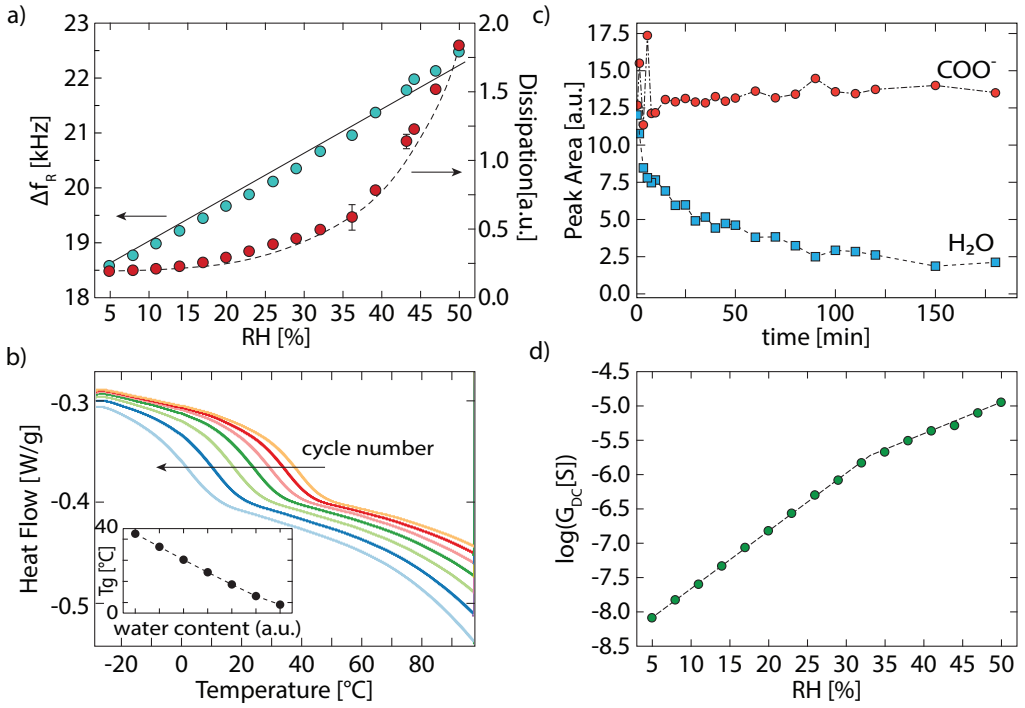

Figure 4.9: Water dependence of the macroscopic properties of HEA–AA. (a) Gravimetric Data as function of RH. Blue dots shift from fundamental resonance frequency of the empty cell, red dots dissipation factor of the resonator (the only points where the error bars are larger than the data marker are at RH 35% and 41%). (b) Differential Scanning Calorimetry Data. Light blue, dark blue, light green, dark green, orange, red, and yellow correspond, respectively, to 1st, 2nd, 3rd, 4th, 5th, 6th, and 7th cycle of the DSC run. Inset represents the calculated glass transition temperature as a function of water content (cycle number). (c) Area of peak calculated from the FTIR data as a function of time. Red Circles area corresponding to the carboxylic acid peak, blue squares area corresponding to the water peak. (d) DC Conductance as a function of RH as calculated with the CTRW model.

Ion Transport

Gravimetric, DSC and FTIR data is insightful to probe the dynamic of water absorption in the polymer and its effect on the polymer matrix. Nonetheless, solely it cannot describe the conduction and thermal response phenomena in HEA–AA. A very powerful tool to probe different conductivity dynamics in polymer electrolytes is dielectric spectroscopy, in which the samples conductance and susceptance are measured as a function of the excitation frequency of the applied electric field. Figure 4.10a shows a representative spectrum of the real conductance of HEA–AA as a function of the excitation frequency measured at constant humidity. Three different regions can be observed: (i) at low frequency a dispersive regime caused by the build-up of the polarization of accumulating ions at the blocking electrodes interface; (ii) a medium frequency region where the conductance is independent from the excitation frequency, indicating that the ion transport is diffusive; (iii) a high frequency "universal" dispersive region where the transport ceases to be diffusive, ions with non successful hops contributes to the conductivity due to the shorter time of the observation window. Similar conclusions can be drawn by looking at the permittivity loss spectrum, derived by the conductance: in region (i) an apparent relaxation peak appears due to the electrode polarization; region (ii) shows a slope of -1 indicating translational motion of charged particles; region (iii) shows the presence of a not fully formed additional relaxation phenomena at higher frequency. In order to measure the influence of water content on the impedance spectrum, we recorded the conductance as a function of RH (5% to 50% increased in steps of 3%) (Fig. 4.10(b)). For increasing RH, the different spectra move up and shift to the right, indicating that the increase in water content increases the absolute conductance and accelerate the conduction processes. Moreover, as frequently reported for temperature, the effect of RH on the high frequency part of the spectra is limited if not absent. For low RH (below 29%) only the diffusive and dispersive regions are visible. The low water content in fact decreases the mobility, resulting in longer diffusion times for the ions which do not have time to travel to the electrode and build an ionic interface. Above RH 29%, the lower frequency electrode polarization region starts to appear. On the other hand, a correlation between RH, ion mobility and the onset frequency of the dispersive regime can be extracted. The frequency at which the conduction becomes from diffusive to dispersive is generally referred to as the onset frequency ν^*. The corresponding time t^* determines the ion mobility μ. It is intuitive that to a shorter t^* corresponds a higher μ, establishing a proportionality between ν^* and μ. Recent works have shown how the time humidity

superposition principle (THSP), equivalent to the time temperature superposition principle (TTSP), can be applied to understand the effect of the water content on the ion mobility and concentration [28–30]. When the Summerfield case is fulfilled $log(\sigma)$ is proportional to the onset frequency of the dispersive regime. This implies that the water content only affects the mobility of the ions, without modifying the concentration of conducting species. If the slope of the line correlating $log(\sigma)$ with $log(\nu^*)$ is greater than the unity it means that the water content also modifies the number density of conducting ions. For HEA–AA the spectra at different humidity superimpose for low frequency but diverge at higher frequency (Fig. 4.8). In this region another relaxation peak appears, as suggested by the permittivity loss in Figure 4.10(a) although not fully developed in the explored frequency range, resulting in spectra that do not completely superimpose. This is further confirmed by the fitting of the experimental data with the continuous time random walk (CTRW) model [26–29]: a good accordance is found for lower frequency, while the model fails to fit the experimental data for higher frequency (Fig. 4.10(c)). In the CTRW model, in fact, only hopping is taken into account, while relaxation phenomena are neglected. To better describe the ion transport in HEA–AA, a relaxation term needs to be added to represents the conduction mechanism:

$$\sigma(\omega) = \frac{i\omega\tau_c\sigma_{DC}}{ln(1+i\omega\tau_c)} - i\sigma_0\nu + \frac{i\omega\epsilon_0\Delta\epsilon}{1+i\omega\tau_{DB}} \tag{4.5}$$

where σ_{DC} is the bulk hopping conductivity, τ_c is the time needed for a charged particle to overcome the energy barrier and corresponds to the inverse of the offset frequency, $\Delta\epsilon$ is the drop in dielectric permittivity due to the dipole polarization event and τ_{DB} the corresponding relaxation time. In this modfied CTRW model, the first two terms are derived from the CTRW model, while the last term is added considering a Debye relaxation process. In this case, we found that the term $i\sigma_0\nu$ is not neglibgile as assumed in the original CTRW derivation and it is needed to achieve a proper fitting of the data [26]. When adding a Debye relaxation term, we can accurately fit the experimental data (Fig. 4.10(c)). Therefore, we can conclude that even if the conductance spectra do not superimpose, the THSP can still be considered valid. In order to verify that the results of the relationship between the DC conductance and the onset frequency do not depend on the model chosen to fit the data, we additionally used the Almond-West (AW) formalism to calculate the onset frequency at different RH. The AW formalism is an empirical model that relates the conductivity to the frequency [30]:

$$\sigma^{'}(\omega) = \sigma_{DC}[1 + \frac{\omega}{\omega^*}]. \tag{4.6}$$

Using this approach, it is possible to calculate the onset frequency ν^* as the intercept between the conductance spectrum and the point at which $\sigma(\nu) = 2\sigma_{DC}$. The DC conductivity and the onset frequencies calculated when applying the AW formalism and the CTRW model agree with each other (Figs. 4.6d and 4.6e). Figure 4.10d shows the the relationship between $log(\sigma)$ and $log(\nu^*)$ for different RH calculated through the modified CTRW model. The slope of the line remains constant up to RH 35%, whereas it increases for humidity above this threshold. Recalling Eq. 4.2, this implies that either the ion number density $N_{Ca^{2+}}$ or the proton number density N_{H^+} is increasing. Provided that FTIR data shows that the ion number density does not change as a function of water content, we can conclude that the change in the slope of $log(\sigma)$ vs $log(\nu^*)$ is caused by the additional proton carriers, whose contribution to the overall conductivity is visible for humidity higher than 35%.

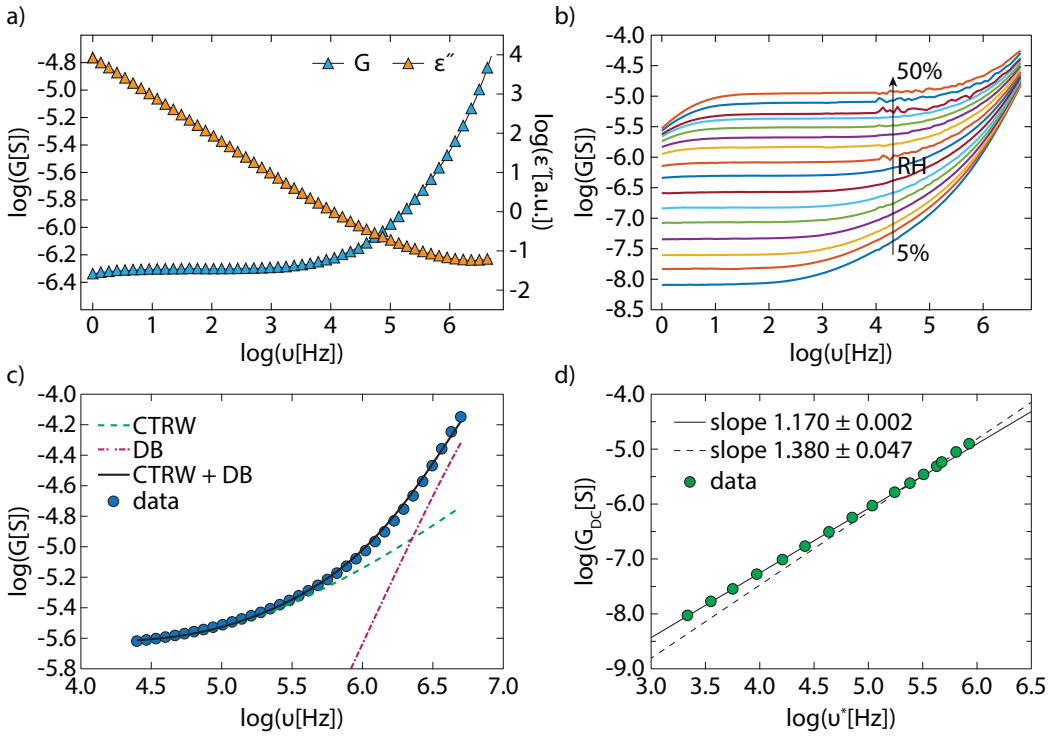

Figure 4.10: Impedance spectra and THSP. (a) Dielectric Spectrum. Blue triangles represent the conductance, while the yellow triangles represent the dielectric loss for a sample at RH 35%. For clarity, markers are a subgroup of the data points. (b) Conductance spectra as a function of RH. (c) Model fitting. The blue dots represent the conductance spectrum of a sample at RH 35%. The green dashed line represents the CTRW model, the purple dotted line a Debye relaxation, while the black line a combination of the two fitted to the data. (d) Onset frequency vs onset conductance as a function of different RH. The linear fit results in two different slope of 1.170 and 1.380.

Relationship between Temperature Response, Onset Frequency, and Glass Transition Temperature

The correlation between proton and ion transport in the system has important implications for the temperature response of this class of materials. Previous work on pectin has indicated how an increase in the water content degrades the temperature response of the polymer [21]. Similar results have been reported for the block copolymer that mimics pectin structure [18]. In this latter work however, a response degradation has also been measured for water content below a certain threshold. This behavior is unexpected because a lower water content should increase the activation energy and thus leads to a higher temperature response. A similar relationship is expected also in the simplified version of the block copolymer used in this work. As presented in Figure 4.10(b), the increase in RH has the effect of shifting up and right the conductance spectra. A similar effect is expected when changing the temperature of the sample. Figure 4.11(a) shows the result of an isochronical impedance spectra taken at constant RH (20%) for different temperatures (42 and 62 °C). Even though the analysis of the conduction mechanism as a function of temperature will be left to forthcoming papers, it is important to notice that, depending on the temperature, some spectra will show only the dispersive and diffusive regions, while others will also present the polarization of the electrodes, in the same frequency range. This leads to a dependence of the temperature response from the excitation frequency. Four regions can be observed: (i) one at lower frequency where the spectrum at lower temperature does not show a fully developed electrode polarization while the one at higher temperature does; (ii) a low medium frequency region where both the spectra are in diffusive regime; (iii) a high medium frequency region where the spectrum at lower temperature is already in the dispersive regime while the higher temperature spectrum is still in the diffusive region, and (iv) a high frequency region where both spectra present dispersive behavior. In region (i), the presence of the electrode polarization affects the effective conductivity, modifying the response. In region (ii) we can describe the temperature effect on the ion conduction since both the curves are in the diffusive regime. We will consider this region to calculate the bulk response R_{DC}. When transitioning to region (iii) the response drops once more since one of the spectra shows increased conductivity as a result of the dispersive regime. Region (iv) shows a weak dependence from temperature, following a common trend for ion conductors when in the near constant loss region. The combination of these behaviors in different parts of the spectrum leads to a dependence of the temperature response from frequency. Figure 4.11(b) shows the impact of

different RH on the response spectra: for increasing RH the characteristic transition frequency from region (i) to (iv) shift to the right, suggesting a dependence from the water content. This behavior can explain the decrease of response below a certain water content when measuring at a single frequency. initially, the excitation frequency falls in region (ii); as the water content decreases the transition frequency between region (i) and (ii) shifts at higher frequencies, and eventually the excitation frequency falls in region (i). This reasoning could also be applied to explain the decrease in response as the water content increase, resulting in an apparent lowering in the response. Nevertheless, Figure 4.11(c) shows that the bulk response spectra for different RH strongly decreases at higher humidity. This behavior indicates that the lowering in the temperature response for higher water content has to be attributed to an overall decrease in the energy barriers that prevent ions from hopping from one site to another and not to the particular frequency used to measure the temperature response. To further confirm this hypothesis, we analyzed the Arrhenius plot, which can provide information on the energetics of the ion transport, for RH going from 5% to 20%. In this case, we do not observe a linear relationship in the Arrhenius plot, indicating that the ion transport is coupled with the segmental motion of the polymer (Fig. 4.11(d)). The conductance G in this scenario is often described by the Vogel–Fulcher–Tammann (VTF) model:

$$G = G_0 exp(\frac{B}{T - T_0}) \tag{4.7}$$

where G_0, B, and T_0 are empirical constants. In particular, the pseudo-activation energy B, correlates to the activation energy of the system, while T_0 is associated with the glass transition temperature. The fitting of the experimental data through the VTF equation shows that both the pseudo-activation energy as well as the glass transition temperature are lowered by the increasing water content. The augmented polymer segmental motion and the lowered binding energy of the metal-polymer complex, result in a lower energy barrier to activate the ion hopping phenomena, which results in a lower temperature response. In fact, generally speaking the activation energy E_a of the ion transport is directly correlated to the bulk temperature response R through:

$$\begin{aligned} E_a &= \frac{log(\sigma_0(T_{max})) - log(\sigma_0(T_{min}))}{1/T_{max} - 1/T_{min}} = \frac{log\frac{\sigma_0(T_{max})}{\sigma_0(T_{min})}}{1/T_{max} - 1/T_{min}} \\ E_a &= \frac{logR}{1/T_{max} - 1/T_{min}} \qquad with \quad R = \sigma_0(T_{max})/\sigma_0(T_{min}). \end{aligned} \tag{4.8}$$

Therefore, lowering the activation energy for the hopping process reduces the temperature response. This important result suggests that the magnitude of the temperature response depends on the strength of the interaction between the metal ion and the coordination complex and can be used as parameter to optimize the material's temperature response.

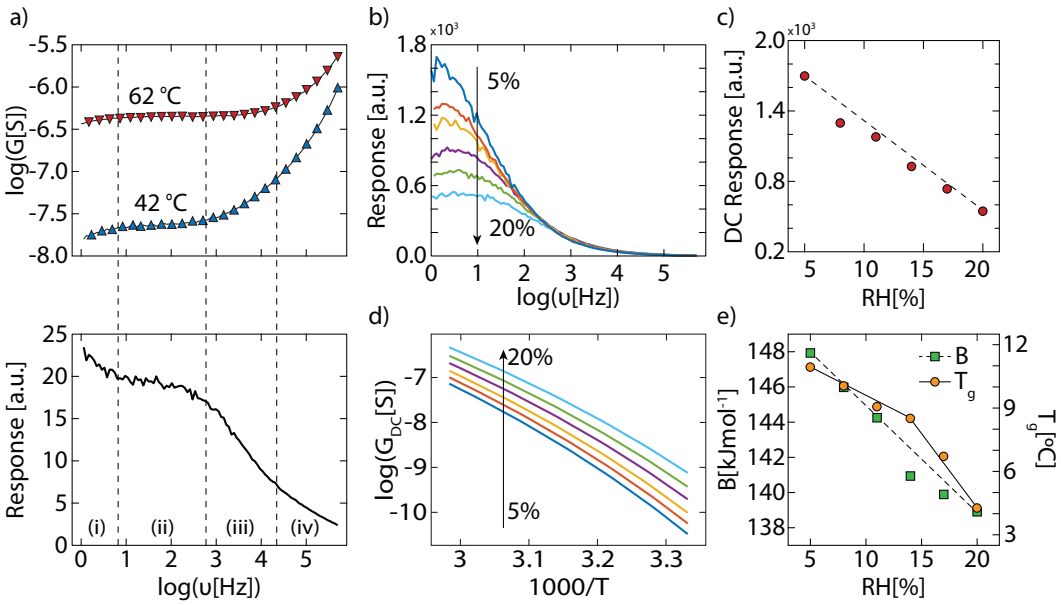

Figure 4.11: Effect of water content on HEA–AA temperature response. Dielectric Spectra as a function of temperature (top) measured at RH 20%. Blue triangles represents the conductance spectrum at measured at 62 °C, while the red triangles represents the conductance spectrum measured at 42 °C. For clarity, markers are a subgroup of the data points. Corresponding temperature response spectra (bottom). Black line represents the conductance temperature response as a function of the frequency measured at 20% RH. The dashed lines indicate the four different regimes of the response. (b) Response spectra for different RH. Light blue, green, purple yellow, orange, and dark blue correspond, respectively, to 20%, 17%, 14%, 11%, 8%, and 5% RH. (c) DC temperature response calculated from the response spectra. (d) Calculated Arrhenius plot fit for the different humidity values. Light blue, green, purple yellow, orange, and dark blue correspond, respectively, to 20%, 17%, 14%, 11%, 8%, and 5% RH. (e) VTF fitting parameters of the Arrhenius plot as a function of humidity. Green squares indicates the pseudo-activation energy B, while the yellow dots the glass transition temperature.

Conclusions

In this work, we investigated the effect of water concentration on the transport phenomena in a single ion conductor polymer composed of HEA–AA and calcium metal ions. We showed that the increase in water content modifies the energetic landscape in which ions hop by increasing the segmental motion of the polymer backbone and the ion mobility, without affecting the number density of mobile metal

cations in the polymer matrix. As a result, we measured a strong effect of water on the ionic conductivity. By applying the THSP, we studied how the concentration of water molecules in the matrix accelerates the conduction processes for lower water concentration, while provide additional proton carriers that contribute to the overall conductivity for higher water concentration. Furthermore, with a higher water concentration, the number of pathways and sites for ion hopping increases, leading to a overall lower activation energy for the transport phenomena. This results in a lower temperature response for increasing water content, implying that the temperature response of the material depends on the interaction between the crosslinking cation and the coordination site.

References

[1] S. S. Sha'rani, E. Abouzari-Lotf, M. M. Nasef, A. Ahmad, T. Ming Ting, and R. R. Ali. Improving the redox flow battery performance of low-cost thin polyelectrolyte membranes by layer-by-layer surface assembly. *Journal of Power Sources*, 413:182–190, 2019.

[2] K. M. Diederichsen and B. D. McCloskey. Electrolyte additives to enable nonaqueous polyelectrolyte solutions for lithium ion batteries. *Molecular Systems Design & Engineering*, 5(1):91–96, 2020.

[3] N. Chen, C. Long, Y. Li, C. Lu, and H. Zhu. Ultrastable and high ion-conducting polyelectrolyte based on six-membered n-spirocyclic ammonium for hydroxide exchange membrane fuel cell applications. *ACS Applied Materials & Interfaces*, 10(18):15720–15732, 2018.

[4] J. Escorihuela, R. Narducci, V. Compañ, and F. Costantino. Proton conductivity of composite polyelectrolyte membranes with metal-organic frameworks for fuel cell applications. *Advanced Materials Interfaces*, 6(2):1801146, 2019.

[5] M. Eldin, H. A. Farag, T. M. Tamer, A. H. Konsowa, and M. H. Gouda. Development of novel iota carrageenan-g-polyvinyl alcohol polyelectrolyte membranes for direct methanol fuel cell application. *Polymer Bulletin*, 77(9): 4895–4916, 2020.

[6] G. S. Manning. Limiting laws and counterion condensation in polyelectrolyte solutions. 7. Electrophoretic mobility and conductance. *The Journal of Physical Chemistry*, 85(11):1506–1515, 1981.

[7] S. Cui, J. Liu, M. E. Selvan, D. J. Keffer, B. J. Edwards, and W. V. Steele. A molecular dynamics study of a nafion polyelectrolyte membrane and the aqueous phase structure for proton transport. *The Journal of Physical Chemistry B*, 111(9):2208–2218, 2007.

[8] D. W. M. Hofmann, L. N. Kuleshova, and B. D'Aguanno. Theoretical simulations of proton conductivity: Basic principles for improving the proton conductor. *Journal of Power Sources*, 195(23):7743–7750, 2010.

[9] A. Vishnyakov, R. Mao, M.-T. Lee, and A. V. Neimark. Coarse-grained model of nanoscale segregation, water diffusion, and proton transport in nafion membranes. *The Journal of Chemical Physics*, 148(2):024108, 2018.

[10] L. Garrido, J. Pozuelo, M. Lopez-Gonzalez, J. Fang, and E. Riande. Simulation and experimental studies on proton diffusion in polyelectrolytes based on sulfonated naphthalenic copolyimides. *Macromolecules*, 42(17):6572–6580, 2009.

[11] V. K. Shahi. Highly charged proton-exchange membrane: Sulfonated poly (ether sulfone)-silica polyelectrolyte composite membranes for fuel cells. *Solid State Ionics*, 177(39-40):3395–3404, 2007.

[12] J. Hou, J. Li, D. Mountz, M. Hull, and L. A. Madsen. Correlating morphology, proton conductivity, and water transport in polyelectrolyte-fluoropolymer blend membranes. *Journal of Membrane Science*, 448:292–299, 2013.

[13] A. H. Shah, J. Li, H. Yang, U. A. Rana, V. Ranganathan, H. M. Siddigi, D. R. MacFarlane, M. Forsyth, and H. Zhu. Enhancement of 'dry'proton conductivity by self-assembled nanochannels in all-solid polyelectrolytes. *Journal of Materials Chemistry A*, 4(20):7615–7623, 2016.

[14] X. Ling, M. Bonn, K. F. Domke, and S. H. Parekh. Correlated interfacial water transport and proton conductivity in perfluorosulfonic acid membranes. *Proceedings of the National Academy of Sciences*, 116(18):8715–8720, 2019.

[15] C. Cramer, S. De, and M. Schönhoff. Time-humidity-superposition principle in electrical conductivity spectra of ion-conducting polymers. *Physical Review Letters*, 107(2):028301, 2011.

[16] S. De, C. Cramer, and M. Schonhoff. Humidity dependence of the ionic conductivity of polyelectrolyte complexes. *Macromolecules*, 44(22):8936–8943, 2011.

[17] S. De, A. Ostendorf, M. Schönhoff, and C. Cramer. Ion conduction and its activation in hydrated solid polyelectrolyte complexes. *Polymers*, 9(11):550, 2017.

[18] T. H. Kim, Z. Zhou, Y.S. Choi, V. Costanza, L. Wang, Y. Yun, H. Kang, S. Kim, and C. Daraio. Flexible biomimetic block copolymer composite for temperature and long-wave infrared sensing. *Nature Communications, under review*, 2022.

[19] R. Di Giacomo, C. Daraio, and B. Maresca. Plant nanobionic materials with a giant temperature response mediated by pectin-ca2+. *Proceedings of the National Academy of Sciences*, 112(15):4541–4545, 2015.

[20] R. Di Giacomo, L. Bonanomi, V. Costanza, B. Maresca, and C. Daraio. Biomimetic temperature-sensing layer for artificial skins. *Science Robotics*, 2 (3):eaai9251, 2017.

[21] V. Costanza, L. Bonanomi, G. Moscato, L. Wang, Y. S. Choi, and C. Daraio. Effect of glycerol on the mechanical and temperature-sensing properties of pectin films. *Applied Physics Letters*, 115(19):193702, 2019.

[22] N. Agmon. The Grotthuss mechanism. *Chemical Physics Letters*, 244(5-6): 456–462, 1995.

[23] S. B. Aziz, T. J. Woo, M. F. Z. Kadir, and H. M. Ahmed. A conceptual review on polymer electrolytes and ion transport models. *Journal of Science: Advanced Materials and Devices*, 3(1):1–17, 2018.

[24] M. V. Voinova, M. Rodahl, M. Jonson, and B. Kasemo. Viscoelastic acoustic response of layered polymer films at fluid-solid interfaces: Continuum mechanics approach. *Physica Scripta*, 59(5):391, 1999.

[25] M. V. Voinova, M. Jonson, and B. Kasemo. On dissipation of quartz crystal microbalance as a mechanical spectroscopy tool. *Spectroscopy*, 18(4):537–544, 2004.

[26] J. C. Dyre. The random free-energy barrier model for AC conduction in disordered solids. *Journal of Applied Physics*, 64(5):2456–2468, 1988.

[27] J. C. Dyre. Unified formalism for excess current noise in random-walk models. *Physical Review B*, 37(17):10143, 1988.

[28] J. C. Dyre. Some remarks on AC conduction in disordered solids. *Journal of Non-Crystalline Solids*, 135(2-3):219–226, 1991.

[29] J. C. Dyre and T. B. Schrøder. Hopping models and AC universality. *Physica Status Solidi (b)*, 230(1):5–13, 2002.

[30] D. P. Almond and A.R. West. Mobile ion concentrations in solid electrolytes from an analysis of AC conductivity. *Solid State Ionics*, 9:277–282, 1983.

Chapter 5

BODY CORE TEMPERATURE SENSOR USING NOVEL ORGANIC TEMPERATURE SENSITIVE POLYMERS

5.1 Chapter Preamble

In the previous chapter, we introduced HEA–AA, a synthetic polymer that can mimic the interaction pectin has with metal ions and that shows a similar temperature response. In this chapter, we will use the main results presented in Chapters 3 and 4 to fabricate an ultrathin DHF thermometer. In particular, we will optimize the material's temperature sensitivity by increasing the strength of the interaction between the ion and the polymer backbone, comparing the temperature response for different metal cations. In addition, we will maximize the DHF accuracy by analysing and mitigating the measurement error sources through FEM simulation. Eventually, we will characterize the performance of the DHF sensor fabricated by integrating HEA–AA as temperature sensitive material in different conditions.

5.2 Abstract

Body core temperature (BCT) is an important physiological vital sign that can provide important information on an individual's health status. The continuous recording of the BCT can have important implications both in hospital settings and at home-care environments for patient management, since it can be correlated to a variety of physical and mental conditions. However, current temperature sensing materials lack the desired temperature sensitivity to allow the fabrication of ultrathin, conformable and wearable BCT sensors with the required accuracy for a medical application. Here, we show the realization of an ultrathin BCT sensor based on dual heat flux (DHF) thermometry. We employ a new class of synthetic polymers with a remarkable temperature sensitivity. We shows that by optimizing the polymer composition and the crosslinking agent, we can tune the polymer's properties to obtain the highest temperature response. Furthermore, to minimize the measurement error in the employed DHF architecture, we identify, through a FE analysis, a correlation between the transversal temperature gradient in the structure and the measurement error. Building on this knowledge, we embed the optimized temperature sensitive polymer into an ultrathin DHF sensor, characterizing its functionality and penetration depth in multiple configurations. The results presented in

this work open the way to truly wearable and accurate DHF sensors that will be able to continuously monitor BCT with the appropriate accuracy needed from a medical device.

5.3 Introduction

The body core temperature (BCT) is a symptomatic indicator of the health status of the body. While crucial in the perioperative stage, where hypothermia can lead to serious consequences during both the surgery and the recovery phase [1–4], internal body temperature can provide numerous information about the status of an infection [5, 6] or inflammation [7–9], the number of calories burnt in a period of time [10, 11] as well as the approaching of ovulation period in the female population [12]. Moreover, BCT reflects the circadian cycle and recently it has been shown how some patterns correlate specifically with sleep quality [13, 14], mental health [15], and degenerative diseases such as Alzheimer [16] and Parkinson [17]. Continuously recording the BCT can therefore be extremely beneficial for a wide spectrum of applications spanning from hospital care to activity monitoring indoor and outdoor. However, the measurement of the BCT cannot easily be achieved with the needed degree of accuracy. The gold standard for the correct measurement of the BCT is the pulmonary artery catheter which records the temperature of the blood flowing directly from the heart. This method is extremely invasive and can be used only in specific surgery procedures. Other strategies rely on the measurement of the temperature of the rectum or the ingestion of radio pills. Nevertheless, they fail when it comes to continuous monitoring or minimal invasiveness. Skin temperature measurement could allow continuous non-invasive recording of body temperature, which however does not correspond to the core temperature. In fact, thermoregulatory processes regulate the inner temperature, while the temperature of the surface and peripheries are a result of temperature gradients and external temperature. This results in a low accuracy when measuring the BCT through skin temperature. In order to overcome these limitations, some strategies that employ the measurement of heat flux have been used. Dual heat flux (DHF) thermoemetry measures the heat flux outgoing the body through two different thermal paths to make the system independent from the thermal resistance of the underlying tissue [18–22]. Nevertheless, given the limited sensitivity and accuracy of commercially available thermal sensors (on average around 100 mK) the dimension of existing heat flux sensors could not be optimized over the thickness. This results in a rather bulky device that is not fully wearable. Moreover, the larger mass results

in to prolonged response times. Using a similar approach, multiple resistance thermometers fabricated on flexible substrates were used to reconstruct the body core temperature [23]. However, the temperature sensing elements employed in this case (a Ti/Cu/Ti/Au resistance thermometer with a theoretical accuracy of around 10 mK) depended on the applied external strains, introducing a source of error difficult to control in a day to day application. In this work, we employed a novel temperature responsive polymer that has shown a record temperature sensitivity [24]. We embedded this polymer in a DHF thermometer to fabricate ultrathin BCT sensors that do not suffer from strain induced errors. Through FE analysis we show the main error sources as well as the maximum penetration depth for the selected geometry in various conditions. We analyzed the chemical composition of the temperature responsive polymer to obtain the highest temperature sensitivity and to achieve the desired sensing functionality. Taking advantage of the complex nature of the temperature response, we show how we can design a readout system in order to achieve an accuracy of 4 mK. Finally, we show our device functionality on a bench top set up, demonstrating that this new polymer type can be successfully integrated in to an ultrathin DHF thermometer, allowing the realization of wearable BCT sensors.

5.4 Materials and Methods

Polymer Synthesis

Nitrogen purged tert-butyl acrylate 2 (1.28 g, 10 mmol) and 2-hydroxyethyl acrylate 1 (1.16 g, 10 mM) is dissolved in 2 mL DMF, followed by S,S-Dibenzyl trithiocarbonate 3 (29 mg, 0.1 mM). The mixture is further purged under nitrogen for 3 minutes, added with AIBN (0.8 mg, 5 μM), and then stirred at 75 °C under protection of N2, and the progress in polymerization was monitored using 1HNMR. The reaction was cooled down and vented to air at approximately 80% conversion rate. Residual tert-butyl acrylate and 2-hydroxyethyl acrylate was removed first by vacuum, followed by precipitation in 100 mL cold Diethyl Ether to yield a yellow oil as the macro-CTA (2.02 g, 80%). For deprotection, polymer (1 g) was dissolved in 3 mL dichloromethane (DCM), followed by addition of 3 mL Trifluoroacetic acid (TFA). The reaction was stirred at room temperature overnight. DCM and TFA were removed by vacuum, followed by precipitation in cold Diethyl Ether, to result in a highly sticky yellow oil as HEA–AA (100%).

FEM Analysis

The geometry was simulated using COMSOL Multiphysics. The skin was simulated as homogeneous medium. Bioheat generation or blood perfusion were not taken into account since previous work have shown to have little impact on the simulation. The substrate was implemented using the thin layer module in order to decrease computation time and achieve a better result. A general layer type was considered to take into account both the normal and tangential heat fluxes. Three different situations were considered for the boundary conditions: radiation heat exchange, convection heat exchange and mixed radiation and convection heat exchange. We first calculated the heat transfer in the system tissue/sensor. Then we used the output of this simulation to compute the heat exchange at the boundaries through radiation and convection. The error was calculated as the difference between the temperature set at the bottom boundary of the tissue and the temperature calculated with Eq. 5.2. The temperature gradient was estimated as the temperature difference between the temperature at the center on the top surface of the thicker heat flux sensor and the temperature of the point on the diagonal at a distance of 20 mm along the diagonal on the same surface. The maximum penetration depth was calculated as the maximum thickness at which the error was calculated to be below 0.25 °C. The thickness of the tissue was incremented in steps of 100 µm.

Thermal Response and Calibration

Temperature cycles on the films were actuated by a Peltier-Element (model Qc-31-1.4-8.5m). The temperature was independently measured with a Pt100 platinum resistance thermometer placed on the polyimide substrate near the polymer. The Pt100 sensors were previously calibrated with a FLIR thermal camera (model A655sc). A PID controller was implemented to generate a sinusoidal temperature between 30 and 65 °C. The substrates and the reference Pt100 were electrically connected through an interface board that could be connected with the impedance analyzer and the temperature control board. The current was measured with the impedance analyzer with an average sampling rate of 10 S/s. The temperature response as a function of frequency was isochronically measured: the frequency was kept constant within one temperature cycles and then changed to the next frequency at the next temperature cycle. Frequency was swept between 1 Hz and 100 kHz. To avoid the thermal hysteresis due to the sample mass we then considered only the raising part of the temperature cycle and sampled the current at different temperatures. The different temperature responses were calculated between 35 and 45 °C.

Electrical Readout

The phase difference between the input voltage and the resulting current flowing through the sample was measured by evaluating the corresponding time lag between the two signals. The harmonic signal used to excite the sample was generated by a Bubba oscillator in which every RC section provides a phase shift of 60 ° to trigger the oscillator. The component were chose to achieve an oscillation at 80 Hz, but due to component mismatching the oscillator had an output frequency of 86 Hz. To avoid the use of a dual supply system, we biased the generated voltage at 2.5 V through a precision Zener diode. The output signal then had an amplitude control to allow flexibility on the excitation signal (Fig. 5.1(a)).The reference sine was then applied to one of the four temperature sensor through an analog multiplexer and then switched to the others. This approach allowed to use only one oscillator and one phase detector/counter for all the sensors. The current flowing through the sample was then converted to a voltage through a resistor, which was then amplified to the desired amplitude through an instrumentation amplifier with a digitally controlled gain. The reference sine and the voltage-converted current were translated in to square waves through fast voltage comparators referenced to 2.5 V. The resulting square waves were then compared with a phase detector that generated a pulse proportional to the phase difference between the two inputs (Fig. 5.1(b)). This time lag was measured by gating a 2 MHz clock with the pulse generated by the phase detector, which was then fed to a 12 bit digital counter. The parallel output of the counter was then converted to a serial bit stream through a PISO register and sent to the µC for data processing. Synchronisation and reset signals were generated by the µC to zero the count of the digital counter and to synchronize the data transfer at the end of each reading. We implemented this design on a 6 layers PCB manufactured by Eurocircuits. The functionality of the readout were characterized by an all-pass filter (Fig. 5.2(a)). This circuit is designed to have a zero and a pole at the same frequency, so that the resulting magnitude is constant with frequency while the phase varies from 180 ° to 0° according to the relation:

$$\Delta\Theta = \pi - 2tan^{-1}(2\pi fRC). \tag{5.1}$$

In this case, we wanted to generate a phase difference at a constant frequency (the one of the readout oscillator), therefore we varied the resistance value R by using a 10 bit, 100 kΩ digital potentiometer (Fig. 5.2(b)). To evaluate the exact phase corresponding to a certain resistance value, we swept the potentiometer from 0 to 1024 while recording the phase difference with a lock-in amplifier at 86 Hz (Fig.

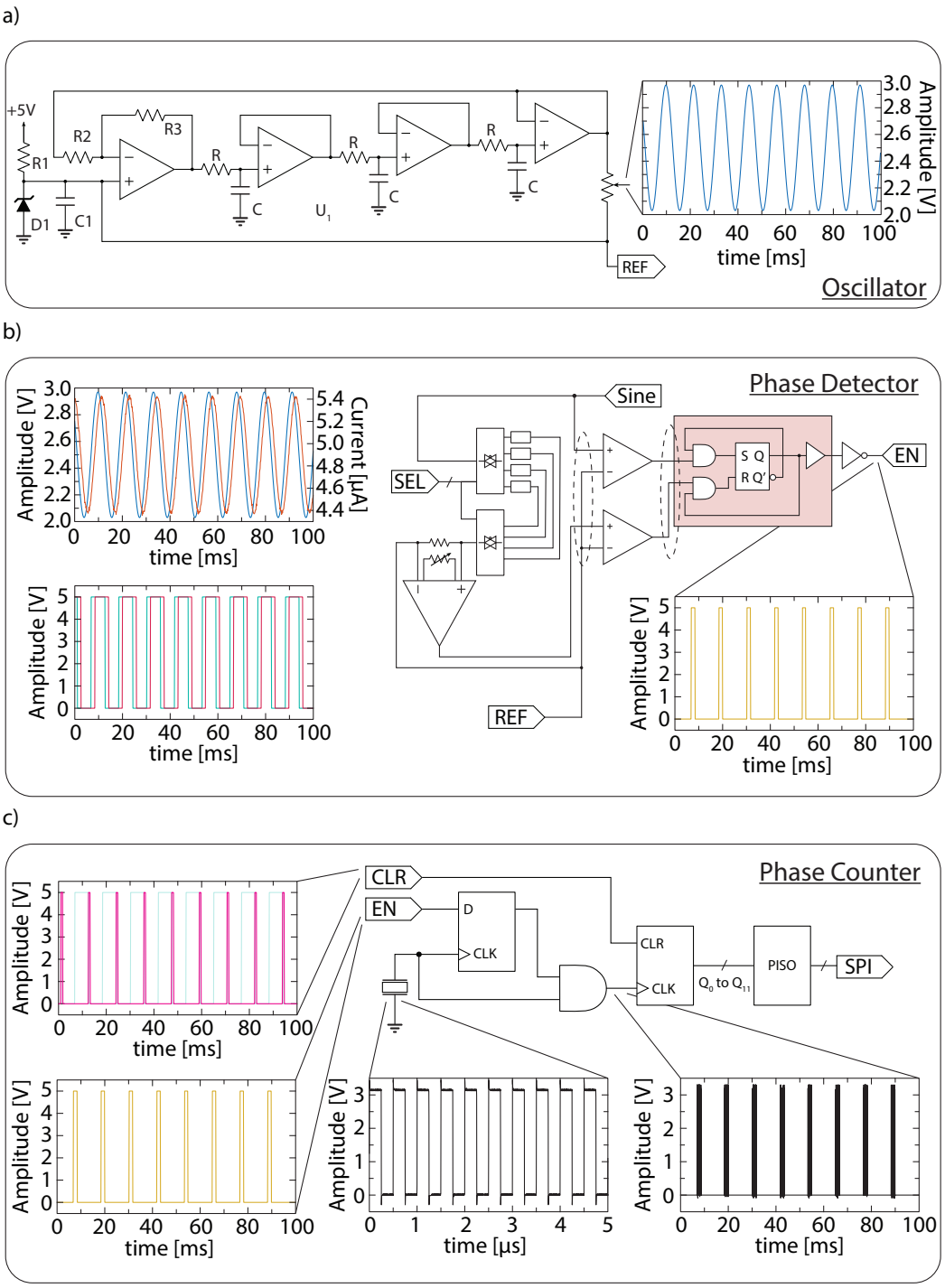

Figure 5.1: Detailed implementation of the electrical readout. (a) Schematic of the harmonic Bubba oscillator. (b) Schematic of the phase detector. (c) Schematic of the phase counter.

5.2(c)). Once a correspondence between the potentiometer value and the resulting phase difference was established, we connected the all-pass filter to the readout

circuit and measured the phase difference (Fig. 5.2(d)). As expected, the measured phase saturates around 60 ° which corresponds to the maximum time lag that can be measured with a 16 bit counter and a 2 MHz clock.

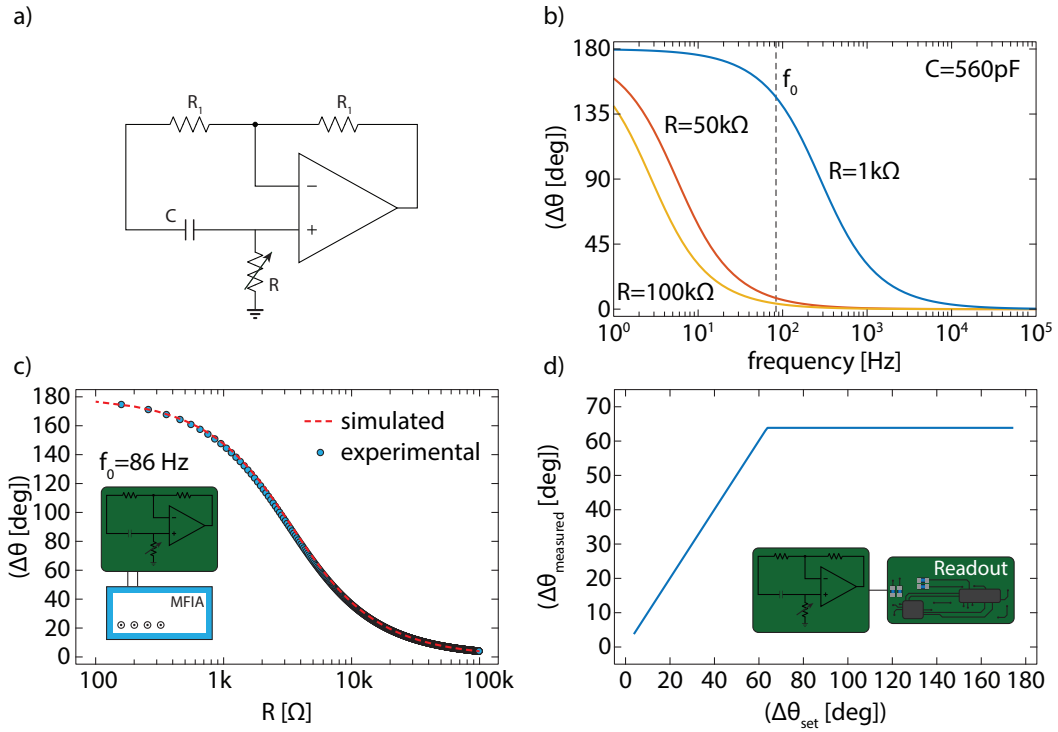

Figure 5.2: Characterization of the readout circuit. (a) Schematic of the all-pass circuit used for the readout calibration. (b) Simulation of the phase difference as a function of frequency (1 Hz to 100 kHz) for different resistance values R: blue line $R = 1\ k\Omega$, orange line $R = 50\ k\Omega$, yellow line $R = 100\ k\Omega$. (c) Phase difference measured at constant frequency $f_0 = 86\ Hz$ for the different resistance values R. Red dotted line simulated results, blue circles experimentally measured data. (d) Phase measured by the readout circuit for different phase values generated by the all-pass circuit.

BCT Measurement

Polyimide substrates with double sided prepatterned copper/immersion gold electrodes (35 µm and 3 µm, respectively) were purchased from PCBWay. On these substrates 5 µL of HEA–AA crosslinked with various ions were deposited and then dried overnight under vacuum. A Pt100 were placed on each side in order to obtain the calibration curves for each sensor. The sensors were then insulated with a 50 µm PET layer to shield the polymer from humidity and placed on a rubber mat with different thickness in order to reproduce the effect of different skins conditions. To further reduce the effect of convective heat exchange with the environment, the DHF sensor was further covered with a piece of clothing. The experiment was performed

at room temperature. The rubber mat along with the sensor was placed on a thermal bath (Thermo Scientific Precision GP 05) to create a stable temperature, which simulate the core temperature, and kept at 37 °C. Data from individual sensors were acquired through the previously discussed readout system at a total sampling rate of 21.5 S/s. In order to measure the response time, we increased the bath temperature from 37 to 39 °C and analyzed the time evolution of the sensor's output when placed on the 6 mm mat.

5.5 Discussion

The temperature distribution along the cutaneous and subcutaneous tissue is determined by the BCT, the external temperature (associated with the corresponding heat exchange phenomena), and the thermal conductivity of the tissue. Theoretically, the BCT can be calculated from the skin temperature, knowing the thermal conductivity of the underlying tissue. However, the thermal conductivity of the human dermis greatly varies from subject to subject, since it depends on multiple factors such as thickness and composition (e.g., lean to fat tissue ratio) of the tissue. This variability on the tissue's thermal conductance makes calculating the BCT prone to several errors. In order to remove the unknown thermal resistance of the tissue, DHF thermometry employs two different thermal paths (Fig. 5.3(a)). The temperature gradient established between the core and the of the skin results in a heat flux flowing outward. If we consider two different heat flux sensors placed on the skin surface, they will measure the same amount of heat flux leaving the body. This will remain the case even when the two heat flux sensors present a different thermal path to the heat flux. Combining the two different thermal balance equations applied to the single heat flux sensor and assuming that the heat flux is the same we can express the BCT as:

$$T_B = T_1 + \frac{(T_1 - T_2)(T_1 - T_3)}{K(T_2 - T_4) - (T_1 - T_3)}. \tag{5.2}$$

where $T_1 : T_4$ are the temperatures of the top and the bottom of the two heat flux sensors, respectively, and K is ratio between the thermal resistance paths under the two heat flux sensors, and it can be calculated as:

$$K = \frac{(T_B - T_2)(T_1 - T_3)}{(T_B - T_2)(T_2 - T_4)}. \tag{5.3}$$

Using these two equations, the BCT can be calculated as follows: first the ratio of the thermal resistances between the two heat flux sensors is measured experimentally. Then, once the parameter K is assessed, the DHF sensor can be used to measure the deep temperature of the body. It is intuitive that the temperature difference

between the bottom and the top surfaces of the DHF sensor is determined by the thermal resistance of the two different paths. The thickness of the insulating layers needs to allow the development of a thermal gradient that is measurable by the temperature sensors placed at the top and bottom of each heat flux sensor. In order to decrease the thickness of the heat flux sensors, extremely accurate temperature sensitive materials have to be used. It has been recently reported how a particular class of polyelectrolytes shows a significantly high temperature sensitivity [24–27]. These polymers are characterized by carboxyl and hydroxyl groups placed along the backbone, which interact with metal cations (e.g., Ca^{2+}, Co^{2+}, Cu^{2+}) present in the polymer matrix. The temperature variation modifies the thermal energy of the system resulting in more or less cations to hop from one coordination site to another, leading to a change in the conductivity (Fig. 5.3(b)). In this work, we synthesized 2-hydroxyethyl acrylate acrylic acid (HEA–AA) with a combination of metal cations to be used for the fabrication of the DHF sensor. The polymer was deposited on to two thin polyimide (PI) layers. To generate two different thermal

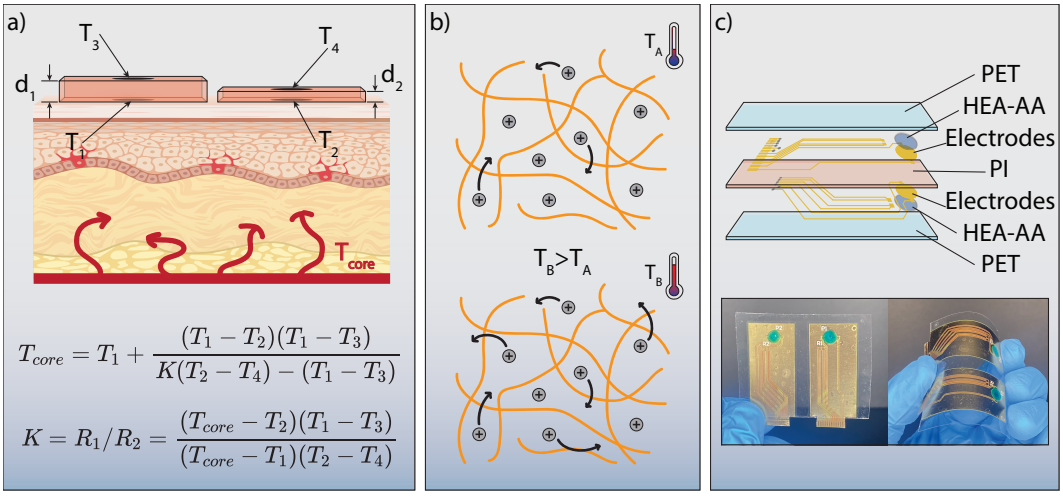

Figure 5.3: Dual Heat Flux sensor and HEA–AA integration. (a) Dual Heat Flux working principle. (b) Temperature sensing mechanism in HEA–AA. (c) Schematic of a DHF sensor integrating HEA–AA in the architecture. Inset: picture of the DHF sensor using Co^{2+} ions flat (left) and bent (right).

paths the PI substrates had different thicknesses of 260 and 100 µm, respectively. On the surfaces of the PI layers, prepatterned Cu/Au plated electrodes were used to electrically connect HEA–AA to measure the conductivity change. Two 10 µm thin HEA–AA layers were deposited on the electrodes and then insulated with a 50 µm thick PET layers (Fig. 5.3(c,top)) from external agents (e.g., room humidity). The resulting DHF sensor is below 500 µm thick and shows a high degree of flexibility,

important since the sensors need to be conformally applied to the curvature of the body (Fig. 5.3(c,bottom)).

Temperature Response Comparison

From a device perspective, HEA–AA is a temperature dependent resistor, since the polymer's conductivity is a function of temperature. However, a temperature coefficient of resistance (TCR), usually used to describe the sensitivity of this class of sensor, cannot be defined in this case because the relationship between temperature and resistance is non-linear. Moreover, the ions present in the polymer network cannot be subjected to a DC voltage to measure the conductivity because that would lead to charge accumulation at the gold blocking electrodes. Therefore, the change of conductivity as a function of temperature needs to be characterized by an AC current resulting from an applied AC. The polymer's conductivity temperature dependence needs to be generalized to a temperature dependence of the complex admittance Y (impedance Z). Figure 5.4a() shows the absolute value of the admittance as a function of frequency (1 Hz to 100 kHz) measured at 35 and 45 °C and at a constant relative humidity (RH) of 10%. In the medium frequency region, a strong frequency dependence does not appear, while at low and high frequency the spectrum presents two strong dispersive regimes. This behavior is in line with ionic conductors were polarization and dielectric relaxation arise in these frequency regions [28]. The phase of the admittance (i.e. the phase difference between the applied voltage and the resulting current) also shows a strong dependence on temperature as well as on the applied frequency (Fig. 5.4(b)). Therefore, we can define the material's temperature response as the ratio between the admittance at highest temperature divided by the admittance measured at the lowest temperature for a specified temperature range:

$$R^*(\omega) = \frac{Y^*(\omega, T_{max})}{Y^*(\omega, T_{min})} = |\frac{Y(\omega, T_{max})}{Y(\omega, T_{min})}|e^{-j\omega[\theta(\omega,T_{max})-\theta(\omega,T_{min})]}. \tag{5.4}$$

As a result, the absolute value of the response $|R^*(j\omega)|$ corresponds to the ratio of the absolute value of the admittance, while the phase of the response $\phi^*(j\omega)$ corresponds to the difference between the phase of admittance:

$$|R^*(\omega)| = \frac{|Y_0(\omega, T_{max})|}{|Y_0(\omega, T_{min})|}, \quad \phi R^*(\omega) = |\theta(\omega, T_{max}) - \theta(\omega, T_{min})|. \tag{5.5}$$

In order to maximize the temperature sensitivity, we prepared different HEA–AA samples crosslinked with Ca^{2+}, Co^{2+}, Cu^{2+}, Mg^{2+}, Zn^{2+}. Each of these ions has a different binding energy with the polymer backbone which will result in a different temperature response. In fact, even though the exact mechanism responsible for the

temperature response in these systems is not completely understood, it is clear that the temperature response is directly correlated to the activation/binding energy of the metal ion with the acid and polar groups along the polymer backbone. This concept becomes more clear in the Arrhenius representation, when considering the ion bulk conductivity σ_0 (the value corresponding to the plateau region in the conductivity spectrum), the temperature response is proportional to the activation energy for ion hopping:

$$E_a = \frac{log(\sigma_0(T_{max})) - log(\sigma_0(T_{min}))}{1/T_{max} - 1/T_{min}} = \frac{log\frac{\sigma_0(T_{max})}{\sigma_0(T_{min})}}{1/T_{max} - 1/T_{min}}$$
$$E_a = \frac{logR}{1/T_{max} - 1/T_{min}} \quad with \quad R = \sigma_0(T_{max}/)\sigma_0(T_{min}) \tag{5.6}$$

where $R_0 = \sigma_0(T_{max})/\sigma_0(T_{min})$ is the conductivity DC response. This correlation has been observed experimentally in multiple scenarios. For example, it has been shown how increasing the number of carboxylic and hydroxyl groups, increases the polymer's temperature response. This behavior is a direct consequence of the the strength of the interaction between the polymer backbone and the metal ion: a higher number of functional groups, creating a coordination complex with higher binding/activation energy E_a. As a result, a higher temperature response R was measured [1]. A stronger interaction between the polymer complex and the metal cation could also be achieved by choosing a ion whose affinity to the coordination complex is particularly high. Previous studies based on MD simulations and experimental data suggest that the geometry of the electronic orbitals combined with the spatial arrangement of the coordination complex will result in larger activation energies [29, 30]. Therefore, we compared different polymer-metal cation combination(i.e. Ca^{2+}, Co^{2+}, Mg^{2+}, Cu^{2+} and Zn^{2+}) to evaluate the one that has the highest temperature response. Figures 5.4(c) and 5.4(d) show the absolute value and phase response spectra for the different cations in the temperature range between 35 and 45 °C. Co^{2+} shows the highest temperature response both in terms of absolute and phase response. Further investigations are needed in order to exactly understand the dynamics of these phenomena in this class of polymers, however in this case these results can be interpreted by considering the water concentration present in the polymer matrix. As described in Chapter 4, an optimal water content is needed to measure a high temperature response. Water in fact can modify in multiple ways the activation energy for the ion transport, such as the coordination environment of the ion as well as the polymer segmental motion. In addition, water molecules can provide additional charge carriers (i.e. protons) with a lower activation energy, which

will lower the temperature response. In order to minimize the effect of the water concentration within the polymer we performed the material's characterization at constant humidity (10%). However, every ion has a different water affinity (Ca^{2+} is highly hygroscopic while Co^{2+} and Cu^{2+} have lower water affinity). To evaluate the difference in water content between the various ions, we measured the conductance at constant temperature (35 °C) (Fig. 5.4(e)). Among the different ions, Co^{2+} has the lowest current compared to the other ions, suggesting that the water content is within the optimal concentration to register an optimal temperature response. The

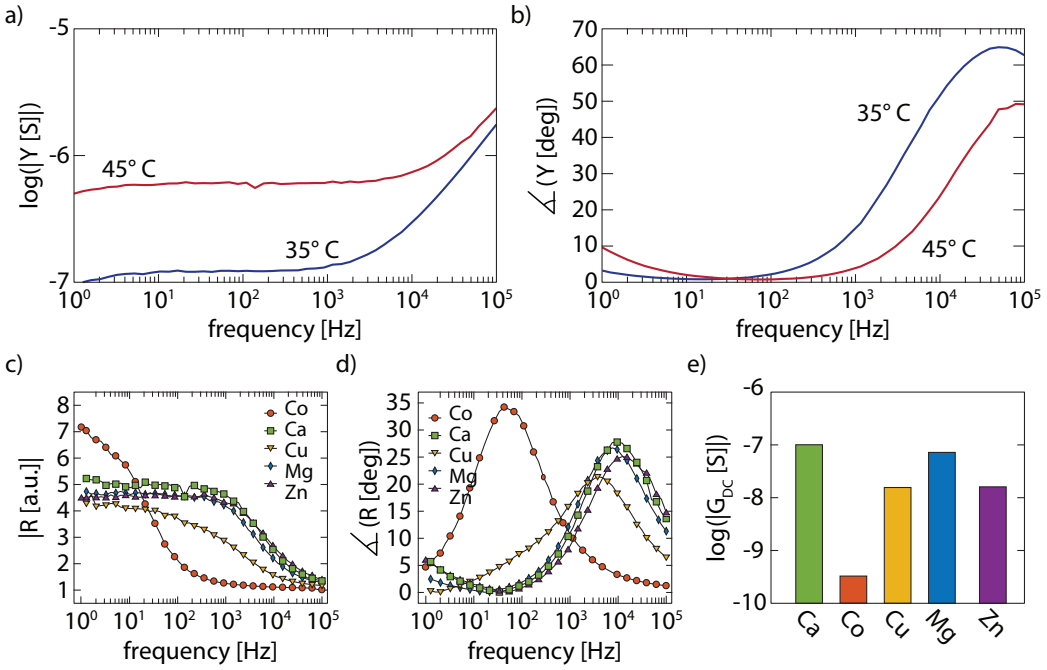

Figure 5.4: HEA–AA characterization. (a) Typical absolute value of the conductance spectra for a sample crosslinked with Ca^{2+} and measured at RH 10%. Blue line absolute value measured at 35 °C, red line absolute value measured at 45 °C. (b) Typical phase of the conductance spectra for a sample crosslinked with Ca^{2+} and measured at RH 10%. Blue line phase measured at 35 °C, red line phase measured at 45 °C. (c) Absolute value of the response as a function of frequency for samples crosslinked with different ions measured at RH 10%: orange dots Co^{2+}, green squares Ca^{2+}, yellow down triangles Cu^{2+}, blue diamonds Mg^{2+}, purple triangles Zn^{2+}. The markers represent a subset of the actual data set. (d) Phase of the response as a function of frequency for samples crosslinked with different ions measured at RH 10%: orange dots Co^{2+}, green squares Ca^{2+}, yellow down triangles Cu^{2+}, blue diamonds Mg^{2+}, purple triangles Zn^{2+}. The markers represent a subset of the actual data set. (e) DC conductance of the samples crosslinked with different ions at 35 °C measured at RH 10%.

information gathered from the comparison between the response obtained with different cations used for the crosslinking can be used to design a proper system for the current to temperature conversion. It is important to notice that, since the response

of the sensor is defined as a complex quantity, two quantities can be used to map the temperature with the measured current: absolute value and phase difference. Figure 5.5(a) shows the typical calibration curve for HEA–AA crosslinked with Co^{2+} ions. The current absolute value increases from 300 pA to 2.2 nA, while the current phase difference decreases from 55 to 20 degree over a 10 °C temperature change. While the current phase difference varies linearly with temperature, the current absolute value–temperature relationship is exponential. Output linearity is an important characteristic for a sensor, since it allows an easy calibration procedure, low computational effort for output to input mapping and the error reduction with input scaling. Therefore, we chose to map temperature with the phase response rather than the absolute value response. In this case, a traditional sensitivity can be defined, since in the analyzed temperature range (35 to 45 °C) the relationship between phase and temperature is linear. A custom read out system was designed to accurately sample the phase response (Figs. 5.5(b) and 5.5(c)). A sinewave

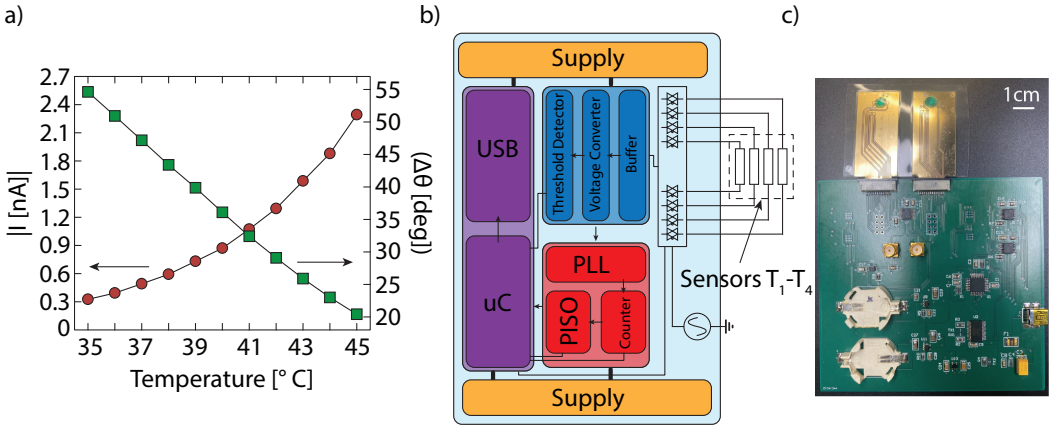

Figure 5.5: Sensors calibration and readout. (a) Sensor temperature calibration. Red circles current absolute value, green squares current phase. (b) Schematic of the readout system. (c) Picture of the readout system and the DHF sensor.

oscillator generates the harmonic voltage to be applied to the sensor through an analog multiplexer. The resulting current flowing through each individual sensor is then converted to a voltage and then amplified by mean of an instrumentation amplifier. The applied voltage and the measured current were then converted to square waves. Because of the reactance of the polymer the voltage and current have a phase difference. This phase difference is measured by a phase detector, which generates a pulse that corresponds to the time delay between the two signals. The pulse width is then quantified through a 2 MHz 16-bit counter. Given the frequency

of the applied voltage $f_{excitation}$, the frequency of the counter clock $f_{counter}$, the phase difference $\Delta\Theta$ correlates to the counter counts n_{count} through the relation:

$$\Delta\Theta = \frac{n_{count}}{f_{counter}} \cdot 360° \cdot f_{excitation}. \tag{5.7}$$

By measuring the phase response, not only the sensor's output is linearized with respect to temperature, but also considerably higher accuracy can be achieved without the need of particular ADC architecture. With the implemented circuit, a minimum phase shift of 0.006 °can be measured, which corresponds to a resolution of circa 4 °mC.

Error Analysis

The optimization of HEA–AA composition ensures that the temperature response of the polymer has the proper sensitivity to measure the small temperature differences across the DHF sensor. However, the precision of the temperature sensors is not the only factor that contributes to the DHF sensor's accuracy. More specifically, in the derivation of Eq. 5.2 some assumptions were made to reach a simple analytical solution. In particular, the heat flux was assumed to be totally transversal with no longitudinal component. We will show that this assumption is the major contribution to the theoretical error of the DHF architecture. Figure 5.6(a,top) shows the transversal and longitudinal thermal gradient that are established in the chosen geometry calculated from the FE simulation. The transversal thermal gradient develops from the bottom of the tissue layer and it is funneled towards the heat flux sensors. At this interface, two different thermal gradients appear because the heat flux sensors have different thickness. Because we chose to use very thin insulating layers for our sensors (260 and 100 μm, respectively), the temperature difference between the top and the bottom of the sensors is in the order of 50 mK. However, as it can be seen in Figure 5.6(a,bottom) there is a non-zero longitudinal temperature gradient that develops over the xy plane. The generation of a transversal thermal gradient has to be attributed to the non-uniform heat exchange along the surface boundaries on the xy plane. Previous works studied the system using radiation [20] or convection [23] boundary condition without taking into account how they affected the measurement error. In order to analyze how the different heat exchange phenomena affect the measurement, we characterized the error e for the two different conditions and we correlated it with the temperature gradient ∇T between the temperature at the center of the top surface of one of the two heat flux, T_A, and the one at the corner on the same surface, T_B. By doing so, we can correlate

the amount of transversal thermal gradient to the measurement error. First we analyzed the heat exchange at the boundaries through radiation only (Fig. 5.6(b)). The rate of heat exchange through radiation depends on the surface emissivity ϵ and the ambient temperature T_{amb}, according to the Stefan-Boltzmann law:

$$-\boldsymbol{n} \cdot \boldsymbol{q}_0 = \epsilon\sigma(T_{amb}^4 - T^4). \tag{5.8}$$

As T_{amb} increases, there will be a lower surface to ambient radiation which will create a smaller gradient on the xy plane. Figure 5.6(c) indicates that the decrease in the thermal gradient proportionally leads to a smaller error. Similarly to radiation, convective heat exchange is determined by ambient temperature T_{amb} and the heat transfer coefficient h:

$$q_0 = h(T_{amb} - T). \tag{5.9}$$

For convective heat exchange with the ambient, the heat transfer coefficient depends on several factors, among which relative humidity or air flow speed. However, heat transfer coefficient in normal conditions ranges between 0.1 – 10 W/m^{2}K. For this simulation, we only modified the heat transfer coefficient keeping the ambient temperature constant. Figure 5.6(c) shows the error as a function of h: for values below 1 W/m^{2}K the error remains low, however it drastically increases above this threshold. This behavior correlates closely with the development of a larger thermal gradient as the heat transfer coefficient increases: for h<1 W/m^{2}K the transversal gradient remains low, while above this value it starts to increase. It is therefore clear how the measurement error is caused by the thermal gradient on the xy plane, whose magnitude is set by the heat exchange characteristics at the boundaries. When combining both heat exchange physics, the complete measurement error can be further analyzed (Fig. 5.6(d)). When radiation is combined with convection, the effect of convection does not drastically impact on the error as long as the heat transfer coefficient is kept low. For higher h (e.g., above 1 W/m^{2}K), the convective heat exchange dominates leading to a larger error. The analysis of the theoretical error indicates that in order to reduce the measurement error in the experimental setting, both the radiation and convection need to be reduced to achieve accurate results. Radiation heat exchange is inevitable and can be only limited by lowering the emissivity of the substrates, which is constrained by the choice of the available materials used to fabricate flexible substrates. Convection can be drastically lowered by the use of materials to thermally insulate the sensor. However, this approach would lead to bulkier and less flexible sensors. However, as previously shown, it is sufficient to ensure that the heat transfer coefficient is below 1W/m^{2}K in order

to minimize the effect of convection. This is the case for most everyday conditions under normal clothing [31]. The use extensive thermal insulation on the device is not required and a clothing layer will be used to reduce to the minimum convective heat. Moreover, it has been shown that the error given by the transversal gradient can be minimized modifying Eq. 5.2 to [20]:

$$T_B = T_1 + \frac{(T_1 - T_2)(T_1 - T_3)}{K(T_2 - T_4) - (T_1 - T_2)}. \tag{5.10}$$

Using the modified Eq. 5.10 and considering both radiative and convective heat exchange (fixed to 1 W/m^{2}K), it is possible to calculate the penetration depth as a function of the ambient temperature (Fig. 5.6(e)). The maximum penetration depth that this method can achieve is the maximum tissue thickness which allows the calculation of the BCT with an error below 0.25 °C. This error threshold was chosen because it is the minimum accuracy the FDA requires for a BCT sensor. The minimum penetration depth is 6.4 mm at 20 °C and the maximum penetration depth is almost 10 mm at 30 °C.

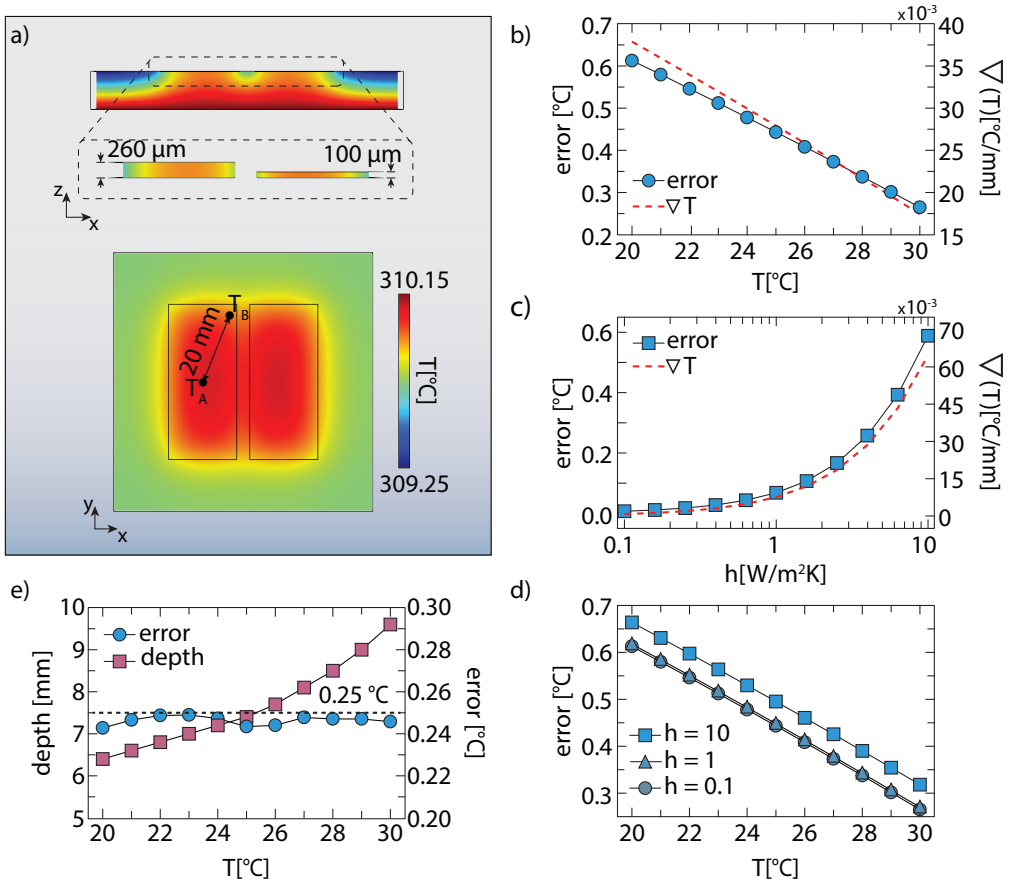

Figure 5.6: FEM Analysis on the BCT architecture. (a) Thermal gradient developed across the xz (top) and xy (bottom) planes. (b) Error (blue circles) and temperature gradient (red dashed line) calculated as a function of external temperature for radiative heat trasnfer. (c) Error (blue squares) and temperature gradient (red dashed line) calculated as a function of heat transfer coefficient for convective heat transfer. (d) Error calculated as a function of external temperature for both radiative and convective heat exchange at different heat transfer coefficients: light blue squares h = 10 W/m^{2}K, blue triangles h = 1 W/m^{2}K, dark blue circles h = 0.1 W/m^{2}K. (e) Penetration depth and corresponding error as a function of external temperature at constant heat transfer coefficient h = 1 W/m^{2}K.

BCT Measurement

Combining the results of the ion comparison in HEA–AA with the readout system and the information gathered by the theoretical error analysis, HEA–AA temperature sensors can now be successfully integrated in the designed DHF architecture. The individual temperature sensors were characterized between 35 and 45 °C to obtain the phase-temperature calibration curve. The calibration data was then fit with a first degree polynomial and the two fit parameters were used to convert the acquired phase to a temperature (Fig. 5.7(a)). The linear fit diverges for higher temperature, but it gives an optimal representation for $T < 43°C$, with coefficient of determination

R greater than 0.9989. To simulate the BCT measurement, we built a custom made setup, where both the accuracy and the time response of the sensor can be estimated (Fig. 5.7(b)). A water bath was used to achieve a constant temperature T_{set} of 37 °C, while a thin copper layer immersed in the bath was used to obtain an homogeneous temperature across the surface. To simulate the skin we used a rubber mat with a thermal resistance similar to the one of the human tissue. In order to evaluate the sensor's performances for different skin thicknesses, rubber mats thick 2, 4, 6 and 8 mm, were used. The DHF sensor was connected to the readout board which was then connected to a computer. At the same time, an IR camera measured the different temperatures of the water bath and the copper layer to ensure that the correct temperature was established in the bath. A piece of regular clothing (few millimiters thick) was used to decrease the heat transfer coefficient with the ambient. We first determined the ratio between the thermal resistance paths K using eq. 5.3 using the 2mm thick rubber mat. Then, the T_{set} was computed from the individual temperatures using eq. 5.10. Figure 5.7(c) shows the estimated BCT using the DHF sensors for the different mat thicknesses. The green area in the plots indicates the ± 0.25 °C maximum allowed error. When the DHF sensor is not thermally insulated with a piece of clothing, the estimated T_{set} has an error greater than 0.25 °C for mats thicker than 2 mm, with a maximum error of 0.76 °C for the 8 mm thick mat. When, the DHF thermometer is covered with a regular piece of clothing, the sensor's performance greatly improve. Error within the 0.25 °C bounds was measured for a mat thickness of 6mm, while for a 8mm thick mat the maximum error was 0.33 °C. These results are in line with the theoretical calculation presented in the previous section. The transversal heat flux is the main responsible for the error in the DHF architecture. Decreasing the heat transfer between the boundaries and the ambient, results in lower a thermal gradient across the sensor which corresponds to a higher sensor accuracy. When covered with a piece of clothing the heat transfer coefficient of the convective transfer between the sensor and the ambient is reduced, resulting in a smaller error. Lastly, we analyzed the transient behavior of the DHF thermometer. We increased the temperature of the thermal bath from 37 to 39 °C and we estimated T_{set} on the 6 mm mat while the sensor was covered with a piece of clothing. Figure 5.7(d) shows the time evolution of the reconstructed temperature when a step response was applied. We calculated the response time as the time the system needed to recover to a error below 0.25 °C. For the selected mat thickness, the reconstructed temperature fell within the accepted error roughly after 15 minutes.

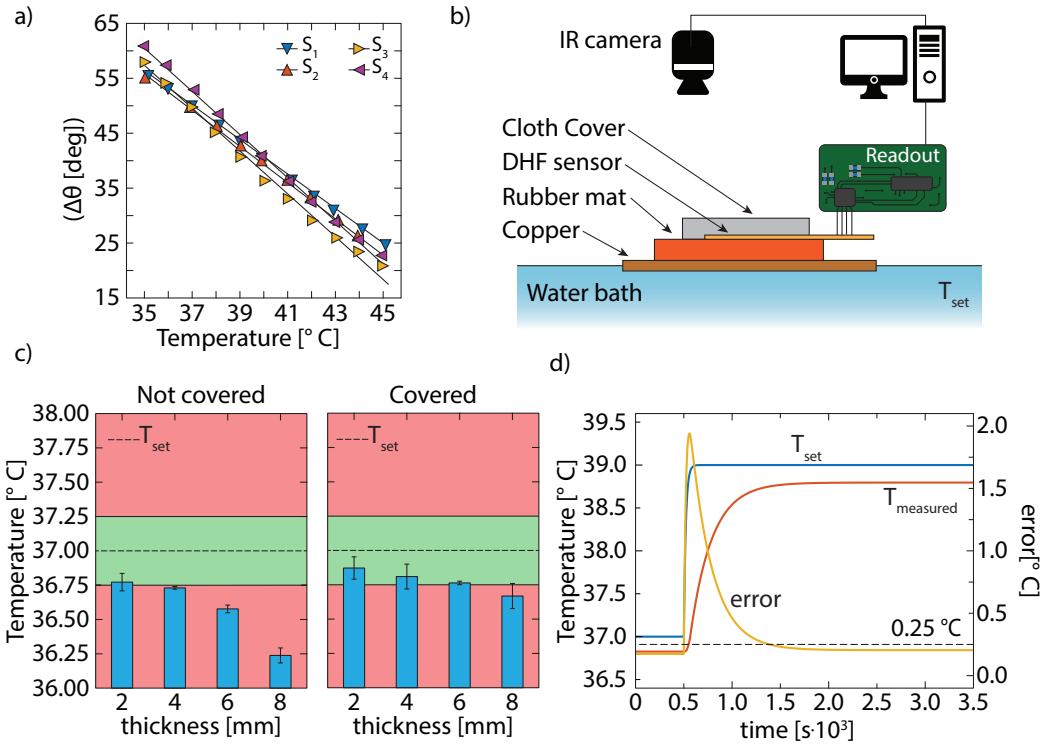

Figure 5.7: BCT measurement. (a) Phase calibration curves for the different temperature sensor in the range 35 and 45 °C. (b) Set up to measure the BCT. The core temperature is simulated by a water bath set to the desired value T_{set}. A thin copper layer is used to achieve homogeneous temperature over the analyzed surface. A rubber mat simulates the tissue layer between the core and the sensor. The DHF is placed on top of the rubber mat and then covered by a piece of clothing. (c) Calculated BCT for a set temperature of $T_{set} = 37°C$, for different thickness of the rubber mat (2, 4, 6, and 8 mm respectively). Measured BCT when when the sensor is exposed to convective heat exchange (left) and when a piece of clothing is applied to insulate the sensor from the environment (right). (d) Step response for the DHF sensor calculated when T_{set} is increased from 37 to 39 °C. Blue line represents thermal bath temperature, orange line represents the DHF sensor output temperature, the yellow line represents the absolute error in the measurement.

Conclusions

In this work, we showed the fabrication of a BCT sensor, integrating a thermally responsive polymer into the DHF thermometer architecture. We optimized the polymer's composition by choosing the best metal cation that showed the highest response. Co^{2+} was found to be the most performing ion because it showed an optimal water content. We employed the complex temperature sensitivity to design a readout systems in which the temperature could be related to the phase of the sensor's admittance, achieving a sensitivity of 3.5 °/°C and a resolution of ± 4 °mC. By simulating the DHF architecture, we found a correlation between the theoretical error

and the longitudinal thermal gradients that develops over the sensors. Furthermore, we analyze different boundary conditions and we calculated the corresponding errors and penetration depth in several conditions. We fabricated a DHF thermometer employing the optimal polymer's composition and we used a custom built readout system to measure the BCT on a characterization setup. We showed that, as described by the FE simulations, the measurement error can be reduced by lowering the heat exchange at the boundaries. The fabricated sensor has an error below ± 0.25 °C for a thickness up to 6mm and a time response of 15 minutes.

References

[1] C. A. Paulikas. Prevention of unplanned perioperative hypothermia. *Aorn Journal*, 88(3):358–368, 2008.

[2] A. Torossian. Thermal management during anaesthesia and thermoregulation standards for the prevention of inadvertent perioperative hypothermia. *Best Practice & Research Clinical Anaesthesiology*, 22(4):659–668, 2008.

[3] S. Moola and C. Lockwood. Effectiveness of strategies for the management and/or prevention of hypothermia within the adult perioperative environment. *International Journal of Evidence-Based Healthcare*, 9(4):337–345, 2011.

[4] O. H Mehta and K. L. Barclay. Perioperative hypothermia in patients undergoing major colorectal surgery. *ANZ Journal of Surgery*, 84(7-8):550–555, 2014.

[5] L. H. Aulick, A. T. McManus, A. D. Mason Jr, and B. A. Pruitt Jr. Effects of infection on oxygen consumption and core temperature in experimental thermal injury. *Annals of Surgery*, 204(1):48, 1986.

[6] N. M. Bagnall, S. Vig, and P. Trivedi. Surgical-site infection. *Surgery (Oxford)*, 27(10):426–430, 2009.

[7] M. J. Kluger. Body temperature changes during inflammation: Their mediation and nutritional significance. *Proceedings of the Nutrition Society*, 48(3):337–345, 1989.

[8] D. Martelli, S. T. Yao, M. J. McKinley, and R. M. McAllen. Reflex control of inflammation by sympathetic nerves, not the vagus. *The Journal of Physiology*, 592(7):1677–1686, 2014.

[9] T. Tesch, E. Bannert, J. Kluess, J. Frahm, L. Hüther, S. Kersten, G. Breves, L. Renner, S. Kahlert, H.-J. Rothkötter, et al. Relationships between body temperatures and inflammation indicators under physiological and pathophysiological conditions in pigs exposed to systemic lipopolysaccharide and dietary deoxynivalenol. *Journal of Animal Physiology and Animal Nutrition*, 102(1): 241–251, 2018.

[10] R. Walford, D. Mock, T. MacCallum, and J. Laseter. Physiologic changes in humans subjected to severe, selective calorie restriction for two years in biosphere 2: Health, aging, and toxicological perspectives. *Toxicological Sciences*, 52(2 Supplement):61–65, 1999.

[11] L. Landsberg, J. Young, W. Leonard, R. Linsenmeier, and F. Turek. Is obesity associated with lower body temperatures? Core temperature: A forgotten variable in energy balance. *Metabolism*, 58(6):871–876, 2009.

[12] M. D. Coyne, C. M. Kesick, T. J. Doherty, M. A. Kolka, and L. A. Stephenson. Circadian rhythm changes in core temperature over the menstrual cycle: Method for noninvasive monitoring. *American Journal of Physiology-Regulatory, Integrative and Comparative Physiology*, 279(4):R1316–R1320, 2000.

[13] H. Middelkoop, G. Lammers, B. Van Hilten, C. Ruwhof, H. Pijl, and H. Kamphuisen. Circadian distribution of motor activity and immobility in narcolepsy: Assessment with continuous motor activity monitoring. *Psychophysiology*, 32 (3):286–291, 1995.

[14] M. Van Veen, J. Sandra Kooij, A. Marije Boonstra, M. Gordijn, and E. Van Someren. Delayed circadian rhythm in adults with attention-deficit/hyperactivity disorder and chronic sleep-onset insomnia. *Biological Psychiatry*, 67(11):1091–1096, 2010.

[15] M. Bagheri Hosseinabadi, M. Ebrahimi, N. Khanjani, J. Biganeh, S. Mohammadi, and M. Abdolahfard. The effects of amplitude and stability of circadian rhythm and occupational stress on burnout syndrome and job dissatisfaction among irregular shift working nurses. *Journal of Clinical Nursing*, 28(9-10): 1868–1878, 2019.

[16] D. Weldemichael and G. Grossberg. Circadian rhythm disturbances in patients with Alzheimer's disease: A review. *International Journal of Alzheimer's Disease*, 2010, 2010.

[17] S. Li, Y. Wang, F. Wang, L. Hu, and C. Liu. A new perspective for Parkinson's disease: Circadian rhythm. *Neuroscience Bulletin*, 33:62–72, 2017.

[18] K.-I. Kitamura, X. Zhu, W. Chen, and T. Nemoto. Development of a new method for the noninvasive measurement of deep body temperature without a heater. *Medical Engineering & Physics*, 32(1):1–6, 2010.

[19] M. Huang, T. Tamura, W. Chen, and S. Kanaya. Evaluation of structural and thermophysical effects on the measurement accuracy of deep body thermometers based on dual-heat-flux method. *Journal of Thermal Biology*, 47:26–31, 2015.

[20] M. Huang, T. Tamura, Z. Tang, W. Chen, and S. Kanaya. A wearable thermometry for core body temperature measurement and its experimental verification. *IEEE Journal of Biomedical and Health Informatics*, 21(3):708–714, 2016.

[21] J. Feng, C. Zhou, C. He, Y. Li, and X. Ye. Development of an improved wearable device for core body temperature monitoring based on the dual heat flux principle. *Physiological Measurement*, 38(4):652, 2017.

[22] J. Fang, C. Zhou, and X. Ye. Optimization of a wearable device for core body temperature monitoring based on the dual-heat-flux model. In *IOP Conference*

Series: Materials Science and Engineering, volume 677, page 032006. IOP Publishing, 2019.

[23] Y. Zhang, R. Chad Webb, H. Luo, Y. Xue, J. Kurniawan, N. H. Cho, S. Krishnan, Y. Li, Y. Huang, and J. A. Rogers. Theoretical and experimental studies of epidermal heat flux sensors for measurements of core body temperature. *Advanced Healthcare Materials*, 5(1):119–127, 2016.

[24] T. H. Kim, Z. Zhou, Y.S. Choi, V. Costanza, L. Wang, Y. Yun, H. Kang, S. Kim, and C. Daraio. Flexible biomimetic block copolymer composite for temperature and long-wave infrared sensing. *Nature Communications, under review*, 2022.

[25] R. Di Giacomo, C. Daraio, and B. Maresca. Plant nanobionic materials with a giant temperature response mediated by pectin-ca2+. *Proceedings of the National Academy of Sciences U.S.A.*, 112(15):4541–4545, 2015.

[26] R. Di Giacomo, L. Bonanomi, V. Costanza, B. Maresca, and C. Daraio. Biomimetic temperature-sensing layer for artificial skins. *Science Robotics*, 2 (3):eaai9251, 2017.

[27] V. Costanza, L. Bonanomi, G. Moscato, L. Wang, Y. S. Choi, and C. Daraio. Effect of glycerol on the mechanical and temperature-sensing properties of pectin films. *Applied Physics Letters*, 115(19):193702, 2019.

[28] B. Huber, L. Rossrucker, J. Sundermeyer, and B. Roling. Ion transport properties of ionic liquid-based polyelectrolytes. *Solid State Ionics*, 247:15–21, 2013.

[29] W. Plazinski and M. Drach. Binding of bivalent metal cations by α-l-guluronate: Insights from the dft-md simulations. *New Journal of Chemistry*, 39(5):3987–3994, 2015.

[30] U. TD Huynh, A. Lerbret, F. Neiers, O. Chambin, and A. Assifaoui. Binding of divalent cations to polygalacturonate: A mechanism driven by the hydration water. *The Journal of Physical Chemistry B*, 120(5):1021–1032, 2016.

[31] N. Mao, M. Song, D. Pan, and S. Deng. Computational fluid dynamics analysis of convective heat transfer coefficients for a sleeping human body. *Applied Thermal Engineering*, 117:385–396, 2017.

Chapter 6

CONCLUSIONS

6.1 Thesis Summary

In this thesis, we reported the fabrication of a ultrathin DHF thermometer with an accuracy suitable for the use of these sensors in medical devices. In order to overcome the limitations posed by previously reported DHF themormeters, we integrated novel thermally responsive materials with a high temperature sensitivity in a conventional DHF architecture. These materials, that belong to the family of polyelectrolytes, draw their thermal sensitive properties by the nature of the interaction between the backbone and the charge carriers present in the polymer matrix.

In Chapter 2, we gave a brief introduction on the ion conduction phenomena in polyelectrolytes. The understanding of the transport properties is essential to analyze the temperature sensing mechanism in this class of polyelectrolytes. A first example of these concepts was shown in Chapter 3, in a system composed of pectin, calcium ions, and glycerol. Due to the electrostatic attraction between carboxyl acids and hydroxyl acids on pectin's backbone, calcium ions are solvated by the matrix. The addition of glycerol allowed to tune the water content in the system and to analyze the effect on the temperature response. Through the analysis of the mechanical properties, we demonstrated how an increase in the water content improves the segmental motion of the polymer backbone. On the other hand, a higher water concentration results in a lower the temperature response, demonstrating that there is a relationship between the transport mechanisms and the temperature sensitivity.

In order to better understand the mechanism that governs the temperature response, we introduced a simpler synthetic polymer scaffold that mimics pectin's structure in Chapter 4. This organic polymer interacts in a similar way with cations and shows a similar temperature response when compared to pectin. Combining DSC, FTIR, and impedance spectroscopy, we described the basic transport mechanism and which carriers mainly contribute to the material's conductivity. Furthermore, we showed that the temperature response results from the strength of the interaction between the coordination complex that is established between the polymer backbone and the metal ions.

Leveraging on the understanding of the nature of the temperature response, we integrated these polymer in the DHF architecture to fabricate BCT sensors. First, we optimized the polymer's composition by choosing the ion that has the strongest interaction with the backbone in order to maximize the temperature response. In addition, we simulated the DHF structure to understand the error sources and to mitigate their impact on the measurement, improving the sensor's accuracy. Finally, we reported the performance of the fabricated DHF thermometer on a custom-made set up. The combination of the material's sensing properties combined with a specifically designed readout circuit allowed us to accurately measure the BCT in multiple conditions.

6.2 Outlook on Future Work

Even though this thesis presented the successful fabrication of a DHF sensor to monitor BCT temperature, there are still multiple scientific questions to be answered and several engineering challenges to be faced to bring this technology to be integrated in actual medical products.

Understanding of the Fundamentals of the Temperature Response

As highlighted in Chapters 3, 4, and 5 the temperature response is a direct consequence of the interaction between the ions and the polymer backbone. In this work, we analyzed in depth the mechanisms that regulate the transport of ions and protons in pectin and HEA–AA and how the temperature response changes when we modified the water content. We found that water affects in multiple way both the carriers transport and the energetics of the solvation of the ions. This strong correlation indicates that there is a link between the conduction phenomena and the temperature response and, in particular, between the thermally activated ion hopping and the thermal sensing polymers in the polyelectrolytes we analyzed. This concept was exploited to optimize the response of the temperature sensors employed in the realization of the DHF sensor. Nevertheless, there are still some mechanisms that still need to be analyzed and understood. In particular, it is not clear whether the thermal energy that is provided to the system when temperature increases, increments the number density of ions available to the transport, or their mobility. The challenge in understanding this mechanism comes once again from the overlapping of these different contributions in the macroscopic conductivity. An interesting approach consists in the application of the Electrode Polarization model developed

by MacDonald[1] and Coelho [2]. The correct application of this model allows to separate the ion number density from the ion mobility by the analysis of dielectric spectroscopy data. Answering this fundamental question has important implications on the application side, since it will allow to further optimize the material's properties, specifically improving the conductivity without sacrificing the temperature sensitivity.

Application of the DHF for continuous BCT monitoring

In this thesis, we have demonstrated that an ultrathin and wearable BCT sensor can be fabricated by integrating thermally sensitive polyelectrolytes in the DHF architecture. Even though the basic operation of the BCT thermometer was characterized, additional optimization and investigations are needed to asses the potential use of this technology in hospital settings as well as for remote patient management. For instance, to further reduce the theoretical error, the geometry of the thermometer (e.g. position and size of the temperature sensing elements) can be further optimized. Similarly, a comparison between different substrate materials with different IR emissivity can lower the heat radiation exchange minimizing the measurement error. In addition, it is crucial to test, for a prolonged amount of time, the functionality of the sensor outside of the laboratory environment to asses both the accuracy and the stability of the BCT sensor. In fact, operating conditions are much more variable when a user is wearing the device: for example, the thermal resistance of the interface between the skin and the sensor can change or the temperature calibration of the temperature sensors can drift over time. The assessment of the sensor's performances in real case scenarios will allow the use of BCT thermometers both as diagnostic tool as well as indicator of several other conditions such as Alzheimer and Parkinson, or mental burnout. In fact, even though a correlation between core temperature and these conditions has been established, the systematic experimental study of the exact medical implications on BCT could not be evaluated due to a lack of appropriate measuring devices.

[1] J. R. Macdonald. Theory of ac space-charge polarization effects in photoconductors, semiconductors, and electrolytes. *Physical Review*, 92:4–17, 1953.

[2] R. Coelho. Sur la relaxation d'une charge d'espace. *Revue de Physique Appliquée*, 18(3):137–146, 1983.

LIST OF ILLUSTRATIONS